Beam intensity effects on the $K^+ \to \pi^+ \nu\bar{\nu}$ measurement at NA62

By

Jack Henshaw

A thesis submitted to the University of Birmingham
for the degree of Doctor of Philosophy

UNIVERSITY OF BIRMINGHAM

Supervisors:

Prof. Evgueni Goudzovski,

Dr. Angela Romano.

Particle Physics Research Group,

University of Birmingham.

December 2023

Abstract

The ultra-rare $K^+ \to \pi^+ \nu\bar{\nu}$ decay, precisely predicted in the Standard Model, is a gateway into exploring new physics at mass scales unattainable at present collider experiments. The NA62 experiment at CERN aims at measuring the branching ratio of the $K^+ \to \pi^+ \nu\bar{\nu}$ decay to a precision of 15% with any deviation from the Standard Model prediction hinting at New Physics.

A Cherenkov detector (CEDAR) is used in NA62 to identify a minority component of particles (kaons) in an unseparated hadron beam. The optical design for a new CEDAR detector optimised to work with hydrogen as radiator gas, Cedar-H, is presented. Cedar-H has been commissioned and installed into NA62 with more than satisfactory performances and a 20% increase in light yield.

The single event sensitivity for the $K^+ \to \pi^+ \nu\bar{\nu}$ decay with data collected in 2021 is computed as $\mathcal{B}_{SES} = (5.00 \pm 0.13_{\text{stat}}) \times 10^{-11}$. Studies of each component entering into this figure and their variation with the intensity of the NA62 hadron beam are performed. A new optimal beam intensity to maximise the number of $K^+ \to \pi^+ \nu\bar{\nu}$ events collected is discussed.

To those who believed in me, even when I did not.

Acknowledgements

Firstly, I must thank my supervisors, Evgueni Goudzovski and Angela Romano, for their guidance.

Additionally, I would like to express my gratitude to the people I have worked with over the years as part of the NA62 collaboration. In particular, John Fry for his assistance through the CEDAR project, Simone Schuchmann regarding anything to do with the MC, and Joel Swallow for his expert guidance and vast knowledge of the $K^+ \to \pi^+ \nu\bar{\nu}$ analysis. To Cristina Lazzeroni, thank you for the proof-reading so close to Christmas. I am also very grateful to Angela Romano for reading drafts and drafts of this thesis and guiding me through the writing process.

My final thanks go to those in the office. Despite COVID-19 stealing a few years of our time, to those of you who have been around, you have contributed to my sanity over the years.

Declaration of author's contributions

In Chapter 1, the theoretical foundations are laid out for the topics discussed in this thesis. Chapter 2 describes the NA62 detector used to collect the data analysed in this thesis; additionally section 2.3 describes the data acquisition, of which the author contributed to in 2021 and 2022, along with the simulation framework used to replicate the collected data described in section 2.4.

Chapter 3 outlines the author's contribution to the NA62 detector in which simulations of the CEDAR using hydrogen as the radiator gas were performed. Sections 3.1 and 3.2 provide the theoretical groundwork for the CEDAR detector along with highlighting the work performed prior to the author's contributions. Sections 3.3, 3.4, and 3.5 follow the author's contributions in redesigning a new CEDAR using hydrogen as the radiator gas at 3.80 bar pressure along with the tolerances required for such a design to perform adequately after construction. The work performed by collaborators in commissioning the Cedar-H is described in subsection 3.6.2 for added context.

Chapter 4 describes the improvements made by the author to the simulation of the NA62 beam intensity profile. A software was created by the author to automate this procedure and its performance is shown in section 4.5.

The collaborative effort of the $K^+ \to \pi^+\nu\bar{\nu}$ analysis is presented in Chapter 5. Section 5.1 provides context to the measurement through defining the analysis procedure and summarising the NA62 result from data collected in 2016-2018. Sections 5.2–5.5 follow the author's independent measurements of all components entering into the single event sensitivity. Section 5.6 compiles all results together and the author recommends that the intensity of the NA62 beam be lowered for data collection in 2023 onwards with the aim of maximising the number of $K^+ \to \pi^+\nu\bar{\nu}$ events collected.

No other qualifications have been achieved with the work presented in this thesis.

Contents

Page

Introduction **1**

1 Theoretical foundations **3**

1.1 Standard Model of particle physics 3

1.2 Kaon physics 9

1.3 $K^+ \to \pi^+ \nu\bar{\nu}$ theory 12

2 The NA62 experiment **17**

2.1 The NA62 beam 18

2.2 Detectors 22

2.2.1 The kaon tagging system 25

2.2.2 The GigaTracker spectrometer 26

2.2.3 The upstream vetocounters 27

2.2.4 The charged anti-coincidence detector 28

2.2.5 The STRAW spectrometer 29

2.2.6 The ring imaging Cherenkov counter 30

2.2.7 The photon veto system 32

2.2.8 The charged particle hodoscopes 35

2.2.9 The muon veto detectors 36

2.2.10 The hadronic sampling calorimeter 37

2.3 Trigger and data acquisition 38

2.4 The NA62 software framework 41

3 A CEDAR detector with hydrogen gas 43

3.1 Working principles of a Cherenkov detector 44

3.1.1 CEDAR 46

3.1.2 KTAG 49

3.1.3 Why use hydrogen? 51

3.2 Previous work 52

3.3 Redesign of CEDAR/KTAG 53

3.3.1 Design methodology for Cedar-H 55

3.3.2 Further KTAG optical considerations 57

3.3.3 Performance of CEDAR designs 58

3.4 Proposed KTAG with Cedar-H at 3.8 bar 59

3.5 Tolerances 66

3.6 Summary 68

3.6.1 Summary of this work 68

3.6.2 Since leaving the project 68

4 Beam intensity simulations 70

4.1 Motivation 71

4.2 The beam intensity 72

4.3 Methods for template creation 75

4.3.1 Reweighting with data/MC ratio 75

4.3.2 Reweighting with 2D histogram 76

4.3.3 Unfolding 76

4.4 Unfolding data 78

4.4.1 The response matrix 78

4.4.2 Unfolding algorithms 80

4.4.3 Selecting the method 82

4.5 New MC templates 85

4.6 Stability of the template 89

4.7 Summary 90

5 Studies of $K^+ \to \pi^+\nu\bar{\nu}$ as a function of beam intensity 92

5.1 Fundamentals . . . 93

5.1.1 Analysis procedure . . . 93

5.1.2 Data & MC samples . . . 95

5.1.3 $K^+ \to \pi^+\nu\bar{\nu}$ selection . . . 96

5.1.4 $K^+ \to \pi^+\pi^0$ and $K^+ \to \mu^+\nu_\mu$ selections . . . 99

5.1.5 Single event sensitivity . . . 100

5.1.6 Summary of NA62 run-1 results . . . 102

5.2 Random veto . . . 103

5.2.1 Photon vetoes . . . 104

5.2.2 Multiplicity vetoes . . . 105

5.2.3 Status for the 2021 analysis . . . 106

5.3 Trigger efficiency . . . 108

5.3.1 L0 . . . 110

5.3.2 L1 . . . 114

5.3.3 Status for the 2021 analysis . . . 117

5.4 Acceptance . . . 117

5.4.1 Status for the 2021 analysis . . . 119

5.5 Number of normalisation events . . . 119

5.5.1 New procedure . . . 120

5.5.2 Status for the 2021 analysis . . . 123

5.6 Compiling results . . . 126

5.7 Summary . . . 129

6 Conclusions 131

References 133

A Cedar-H simulation parameters and tolerance plots 140

List of Figures

1.1 Standard Model of particle physics 4
1.2 Illustration of the unitarity triangle 8
1.3 Measured values of the unitarity triangle 8
1.4 Feynman diagrams for $K^0 - \overline{K}^0$ mixing. 9
1.5 Feynman diagrams for the $K^+ \to \pi^+ \nu\bar{\nu}$ decay. 12
1.6 Unitarity triangle for the $K^+ \to \pi^+ \nu\bar{\nu}$ decay 15
1.7 Error budget on the theoretical branching ratios 16

2.1 Schematic of K12 beam line 19
2.2 Schematic of the second achromat 21
2.3 Schematic of NA62 23
2.4 Schematic of original CEDAR 25
2.5 Schematic of the GTK 26
2.6 Schematic of the ANTI-0 28
2.7 Schematic of the STRAW 29
2.8 RICH ring radius vs momentum 31
2.9 Schematic of the LKr 34
2.10 Schematic of the NA48-CHOD 35
2.11 Schematic of the CHOD 36
2.12 MUV3 tile geometry 37
2.13 Software diagram 42

3.1 Standard CEDAR Schematic 47
3.2 Geant4 visualisation of the KTAG optics. 49

3.3 Arrangement of PMTs in the lightguide 50

3.4 Quantum efficiency of the PMTs used in KTAG 51

3.5 Photon wavelength versus radius at the diaphragm for the Cedar-W with N_2 and H_2 52

3.6 Image of an opened CEDAR 54

3.7 Number of photons at diaphragm versus Mangin Mirror inner radius . 57

3.8 Light distribution at the diaphragm for the Cedar-H with radiator gas pressure of 3.80 bar. 60

3.9 Distribution of light over the PMT array for a hydrogen radiator gas pressure of 3.80 bar. 61

3.10 Ray tracing through the CEDAR for a hydrogen radiator gas at 3.80 bar pressure. 62

3.11 Average hit rate in each PMT for the new Cedar-H design. 63

3.12 Photon wavelength versus radius at the diaphragm for the Cedar-H . 64

3.13 Pressure scans for the new Cedar-H design. 65

4.1 Data/MC ratio for the beam intensity using the 2017 template 71

4.2 Distribution of beam intensity for 2018 data 73

4.3 Spill structure of the beam 74

4.4 GTK hit efficiency 75

4.5 Illustration of the unfolding procedure 77

4.6 Response matrix using the 2017 template 79

4.7 Response matrix using a uniform template 80

4.8 Bias of each of the unfolding algorithms 83

4.9 Unfolded true intensity for each of the unfolding algorithms 84

4.10 Data/MC ratio for Bayesian and IDS unfolding 85

4.11 New intensity templates 86

4.12 Data/MC for beam intensity using the new 2017 template 87

4.13 Data/MC for beam intensity using the new 2018 template 87

4.14 Data/MC for beam intensity using the new 2021 template 88

4.15 Data/MC for beam intensity using the new 2022 template 88

4.16 Unfolding 2018 MC to obtain the 2018 template 89
4.17 Unfolding 2018 data with different response matrices 90

5.1 Distribution of m^2_{miss} for the signal and background channels 94
5.2 $K^+ \to \pi^+\nu\bar{\nu}$ signal regions in $m^2_{\text{miss}} - P_{\pi^+}$ space 95
5.3 Unblinded signal regions for 2018 data. 103
5.4 LKr cluster time versus π^+ track time. 105
5.5 Photon Veto Efficiency as a function of intensity for 2021 106
5.6 Multiplicity Veto Efficiency as a function of intensity for 2021 107
5.7 L0 Trigger efficiencies measured on 2021 data 111
5.8 LKrL0 measurement for 2021 113
5.9 Trigger efficiency of the $K^+ \to \pi^+\nu\bar{\nu}$ L0 conditions versus momentum 114
5.10 L1 Trigger efficiencies measured on 2021 data 116
5.11 L1 STRAW efficiency as a function of momentum 116
5.12 Acceptance as a function of momentum 118
5.13 Number of normalisation events per burst 121
5.14 Expected number of normalisation events per burst 123
5.15 Number of normalisation events measured on 2021 data 124
5.16 Number of normalisation events measured on 2018 data 126
5.17 Expected $K^+ \to \pi^+\nu\bar{\nu}$ events per burst 128
5.18 Components contributing to $K^+ \to \pi^+\nu\bar{\nu}$ events per burst 128

A.1 Tolerance on the Mangin Mirror x-y position 142
A.2 Tolerance on the Mangin Mirror reflective surface radius 143
A.3 Tolerance on the Mangin Mirror refractive surface radius 143
A.4 Tolerance on the Mangin Mirror reflective surface centre of curvature 144
A.5 Tolerance on the Mangin Mirror refractive surface centre of curvature 144
A.6 Tolerance on the Mangin Mirror thickness 145
A.7 Tolerance on the Mangin Mirror angle of tilt 145

A.8 Tolerance on the Chromatic Corrector x-y position 146
A.9 Tolerance on the Chromatic Corrector radius 146
A.10 Tolerance on the Chromatic Corrector centre of curvature 147
A.11 Tolerance on the Chromatic Corrector thickness 147
A.12 Tolerance on the Chromatic Corrector angle of tilt 148
A.13 Tolerance on the Spherical Mirror radial offset 149
A.14 Tolerance on the Spherical Mirror z posiiton 149
A.15 Mean of light rings position as a function of refractive index 151
A.16 Width of light rings as a function of refractive index 152
A.17 Example Gaussian Distributions used in the refractive index tolerance. 153
A.18 Width of light rings for a Gaussian refractive index 154

List of Tables

1.1 Properties of charged and neutral kaons 11

1.2 Kaon decay modes 11

2.1 K12 beam parameters 22

2.2 NA62 components and role 24

2.3 L0 Trigger Conditions 40

2.4 Trigger lines for 2018 41

3.1 Performance of Cedar-H designs. 59

3.2 Performance of KTAG for the new Cedar-H and NA62 Cedar-W. . . 60

3.3 Required changes to the CEDAR internal and external optics for the new Cedar-H design. 63

3.4 Cedar-H Tolerances. 67

4.1 Beam composition weights. 74

5.1 Main backgrounds to the $K^+ \to \pi^+\nu\bar{\nu}$ analysis 94

5.2 Acceptances of the selections used in the $K^+ \to \pi^+\nu\bar{\nu}$ analysis 118

A.1 Simulation parameters for each Cedar design. 141

Introduction

The development in the understanding of elementary particles and their interactions over the 20th century has resulted in the formulation of the Standard Model (SM). Its aim is to encapsulate all knowledge of the properties of fundamental particles and the forces that act upon them into one unified theory. Whilst the SM has been a remarkable collaboration of work it still however remains an incomplete theory that does not provide explanation for neutrino masses [1], matter-antimatter asymmetry [2], dark matter [3, 4], and the inclusion of the fourth fundamental force, gravity.

The target of modern particle physics is to look for New Physics (NP) effects that are not accounted for in the SM. Experimental searches are vital in providing the missing puzzle pieces for further progression of our understanding. Two approaches using particle accelerators are typically used and can be described as the energy frontier and the intensity frontier. The former describes experiments pushing the very limits of accelerating particles to achieve the highest possible beam energy such that new, heavier, particles can be directly measured. This approach led to the discovery of the Higgs boson particle by the ATLAS [5] and CMS [6] experiments at CERN in 2012. The goal of the intensity frontier is the collection of large datasets allowing for precise measurements of the properties of a particle. Any deviations of the measurement from the theoretical SM predictions indirectly hints at new physics in the underlying process yet to be discovered or understood. Both approaches are

vital and complimentary in progressing the theory of the SM.

Kaons have played a key role in the understanding of the flavour sector of the SM. Some examples are the indirect discovery of the charm quark in $K_L^0 \to \mu^+\mu^-$ decays [7], tests of lepton flavour universality [8], and direct CP violation in kaon decays [9–11]. For over 40 years, a series of fixed target experiments in the CERN North Area (NA31, NA48, and NA62) using the Super Proton Synchrotron (SPS) have led a dedicated kaon physics programme in the intensity frontier. These experiments are devoted to the study of kaon decays and precise measurement of cornerstone principles of the SM. The main goal of the NA62 experiment at CERN is the measurement of the branching ratio of the ultra-rare $K^+ \to \pi^+\nu\bar{\nu}$ decay highly sensitive to NP effects and precisely predicted in the SM. The most precise measurement of the branching ratio for this decay was obtained with the analysis of data collected in 2016-2018, $\mathcal{B}_{\pi\nu\nu} = (10.6^{+4.0}_{-3.4}|_{\text{stat}} \pm 0.9_{\text{syst}}) \times 10^{-11}$ [12]. NA62 will continue to take data until 2025 with the aim of further increasing the experimental precision on the $K^+ \to \pi^+\nu\bar{\nu}$ branching ratio down to 15%.

The work described in this thesis was carried out within the NA62 experiment. The outline of this thesis is as follows: Chapter 1 provides the theoretical context required for the work performed in the thesis. Chapter 2 describes the NA62 experiment and detector including data collection periods and detector simulations. Chapter 3 describes the work performed in redesigning the NA62 CEDAR detector to use hydrogen as the radiator gas instead of nitrogen whilst maintaining its required performance for operation in NA62. Chapter 4 outlines the improvements made to the NA62 simulation of the beam intensity in Monte-Carlo data. Finally, Chapter 5 describes the measurement of the NA62 single event sensitivity for the $K^+ \to \pi^+\nu\bar{\nu}$ decay using 2021 data with the up-to-date analysis at the time of writing this thesis.

Chapter 1

Theoretical foundations

In this chapter, we explore the theoretical ground work to the Standard Model of particle physics with an emphasis on kaon physics in the flavour sector. The Cabibbo-Kobayashi-Maskawa (CKM) matrix is explored along with the decays of neutral and charged kaons including the ultra-rare $K^+ \to \pi^+ \nu\bar{\nu}$ and $K_L^0 \to \pi^0 \nu\bar{\nu}$ decays.

1.1 Standard Model of particle physics

The Standard Model (SM) of particle physics aims to encapsulate all knowledge of the fundamental constituents of matter and their interactions. Whilst the understanding of which particles form these fundamental building blocks has changed over time, it is currently understood to contain 12 elementary fermions, 5 vector bosons and a scalar boson, see Figure 1.1. However, the SM is not a complete theory; for example, the gravitational force is not accounted for but is insignificant on a particle scale in comparison to the strength of the other 3 forces (electromagnetic, weak, and strong). Therefore, whilst the SM aims to summarise all of our current

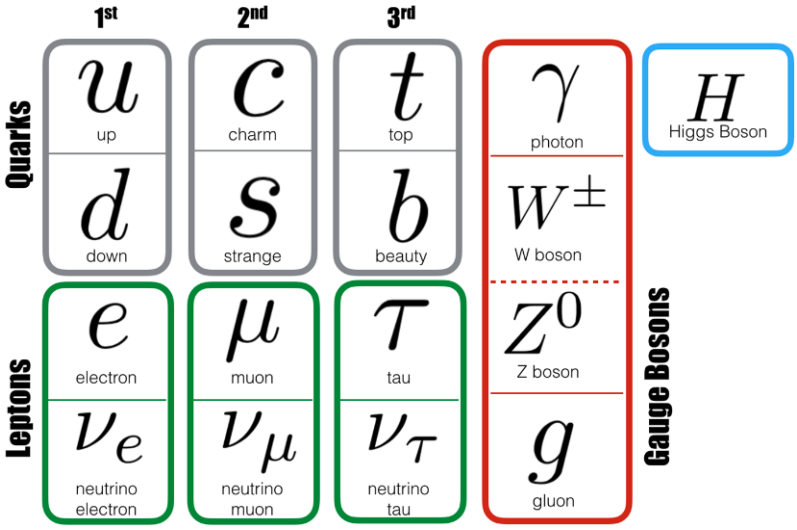

Figure 1.1: Standard Model of particle physics. The twelve elementary fermions are shown in the grey and green blocks whilst the five vector bosons are shown in red; the scalar (Higgs) boson is shown in blue. Figure taken from [13].

knowledge of particle physics, some elements are still missing. Experimental results that show deviations from SM predictions could hint at new physics yet to be discovered. These deviations are most likely to be found by addressing observables precisely predicted in the SM such as the $K^+ \to \pi^+ \nu\bar{\nu}$ decay rate; the more precisely a quantity is measured, the easier it is to distinguish any disagreements from theory. Additionally, deviations from the SM predictions may be linked to sources of new physics that could answer open questions such as matter-antimatter asymmetry [2], why the particle masses are what they are, and what is dark matter [4].

The SM is a gauge quantum field theory with a non-Abelian symmetry group $SU(3) \times SU(2) \times U(1)$, it is self-consistent and also renormalisable. The strong interaction is described by the $SU(3)$ group and electroweak by $SU(2) \times U(1)$. The electroweak component is spontaneously broken by the Higgs field and as a result the associated electroweak gauge bosons ($W^{\pm}$, Z^0) are massive. As a consequence of this symmetry breaking, the strong (mass) and weak (flavour) eigenstates of quarks diverge. The conversion between the weak eigenstates (d', s', b') and the mass eigenstates (d, s, b) is via the Cabibbo-Kobayashi-Maskawa (CKM) matrix, often

labelled V_{CKM} [14, 15]:

$$\begin{bmatrix} d' \\ s' \\ b' \end{bmatrix} = \begin{bmatrix} V_{ud} & V_{us} & V_{ub} \\ V_{cd} & V_{cs} & V_{cb} \\ V_{td} & V_{ts} & V_{tb} \end{bmatrix} \begin{bmatrix} d \\ s \\ b \end{bmatrix} = V_{CKM} \begin{bmatrix} d \\ s \\ b \end{bmatrix} \tag{1.1}$$

Here the probability that a quark will transition from type i to j in a flavour-changing decay is given by $|V_{ij}|^2$.

Whilst the CKM matrix has nine elements, the unitarity requirement from the universality of the weak interaction [16], and the gauge invariance reduce the number of free parameters in the SM down to four. The CKM matrix can be parametrised using three mixing angles corresponding to the coupling between the quark generations (θ_{12}, θ_{13} and θ_{23}) and a CP-violating phase (δ) [17]:

$$V_{CKM} = \begin{bmatrix} c_{12}c_{13} & s_{12}c_{13} & s_{13}e^{-i\delta} \\ -s_{12}c_{23} - c_{12}s_{23}s_{13}e^{i\delta} & c_{12}c_{23} - s_{12}s_{23}s_{13}e^{i\delta} & s_{23}c_{13} \\ s_{12}s_{23} - c_{12}c_{23}s_{13}e^{i\delta} & -c_{12}s_{23} - s_{12}c_{23}s_{13}e^{i\delta} & c_{23}c_{13} \end{bmatrix}. \tag{1.2}$$

Here, $s_{ij} = \sin\theta_{ij}$ and $c_{ij} = \cos\theta_{ij}$. The angles can be chosen such that they lie in the first quadrant, i.e $s_{ij}, c_{ij} \geq 0$. Alternatively, using the experimental condition $s_{13} \ll s_{23} \ll s_{12} \ll 1$ [18], it is convenient to express the CKM matrix with the Wolfenstein parameters [19]:

$$V_{CKM} = \begin{bmatrix} 1 - \frac{\lambda^2}{2} & \lambda & A\lambda^3(\rho - i\eta) \\ -\lambda & 1 - \frac{\lambda^2}{2} & A\lambda^2 \\ A\lambda^3(1 - \rho - i\eta) & -A\lambda^2 & 1 \end{bmatrix} + \mathcal{O}(\lambda^4) \tag{1.3}$$

where

$$\lambda = s_{12}, \qquad A\lambda^2 = s_{23}, \qquad A\lambda^3(\rho - i\eta) = s_{13}e^{-i\delta}. \tag{1.4}$$

As a result, the unitarity of the CKM matrix is lost. In changing,

$$\bar{\rho} = \rho(1 - \frac{\lambda^2}{2}), \qquad \bar{\eta} = \eta(1 - \frac{\lambda^2}{2}), \tag{1.5}$$

the unitarity of the CKM matrix is restored [20].

The measured values of the CKM matrix are shown here, where various measurements have been combined [18]:

$$\begin{bmatrix} |V_{ud}| & |V_{us}| & |V_{ub}| \\ |V_{cd}| & |V_{cs}| & |V_{cb}| \\ |V_{td}| & |V_{ts}| & |V_{tb}| \end{bmatrix} = \begin{bmatrix} 0.97435 \pm 0.00016 & 0.22500 \pm 0.00067 & 0.00369 \pm 0.00011 \\ 0.22486 \pm 0.00067 & 0.97349 \pm 0.00016 & 0.04182^{+0.00085}_{-0.00074} \\ 0.00857^{+0.00020}_{-0.00018} & 0.04110^{+0.00083}_{-0.00072} & 0.999118^{+0.000031}_{-0.000036} \end{bmatrix}. \tag{1.6}$$

We note that the diagonal elements are dominant reflecting that transitions between the same generation are preferred whilst changes between one generation are suppressed and those between two generations are doubly suppressed. This suppression is also clear in the Wolfenstein parametrisation where changes between one generation are $\mathcal{O}(\lambda)$ whilst changes between two generations are $\mathcal{O}(\lambda^3)$.

In ensuring unitarity of the CKM matrix such that (d', s', b') are orthonormal single-quark states similar to (d, s, b), one obtains the expressions:

$$\begin{aligned} \sum_i V_{ij} V_{ik}^* &= \delta_{jk}, \\ \sum_j V_{ij} V_{kj}^* &= \delta_{ik}, \end{aligned} \tag{1.7}$$

which leads to six vanishing contributions, often represented as 'unitarity triangles' in a complex plane. The most common of which,

$$V_{ud} V_{ub}^* + V_{cd} V_{cb}^* + V_{td} V_{tb}^* = 0, \tag{1.8}$$

can be written in terms of the modified Wolfenstein parametrisation using the

parameters $\bar{\rho}$ and $\bar{\eta}$,

$$1 + \frac{V_{td}V_{tb}^*}{V_{cd}V_{cb}^*} = -\frac{V_{ud}V_{ub}^*}{V_{cd}V_{cb}^*} = \bar{\rho} + i\bar{\eta}, \tag{1.9}$$

and is shown graphically in Figure 1.2. The vertices of such triangle are defined as being exactly $(0, 0)$, $(1, 0)$ and $(\bar{\rho}, \bar{\eta})$. The most up to date experimental results at the time of submission of this thesis are shown in Figure 1.3.

In total the SM contains nineteen free parameters originating from the most general Lagrangian:

- The four CKM parameters previously discussed.
- Three lepton masses (electron, muon, and tau).
- Six quark masses (up, down, charm, strange, top, and bottom).
- Three gauge couplings (U(1), SU(2) and SU(3)).
- Quantum ChromoDynamics (QCD) vacuum angle.
- Higgs vacuum expectation value and Higgs boson mass.

Each parameter listed above needs to be experimentally measured, with greater precision allowing for more accurate predictions which in turn can be experimentally validated. Cases in which experimental results do not agree with the predictions could hint at new physics. Theories attempting to explain these 'anomalous' results with new physics would need to be validated before being integrated into the SM.

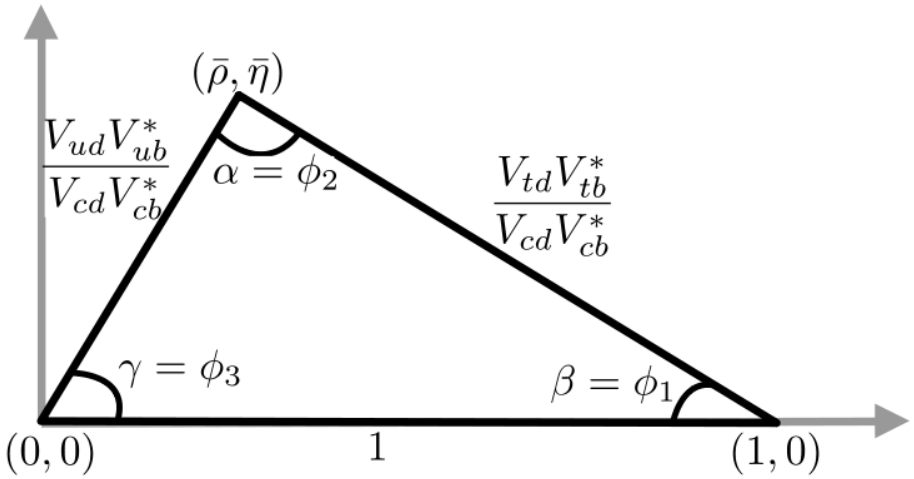

Figure 1.2: Illustration of a unitarity triangle obtained from enforcing the unitarity criteria on the CKM matrix. Here the most commonly used triangle is shown and how this relates to the parameters $\bar{\rho}$, $\bar{\eta}$ and the angles (ϕ_1, ϕ_2, ϕ_3) or (α, β, γ) commonly shown in literature.

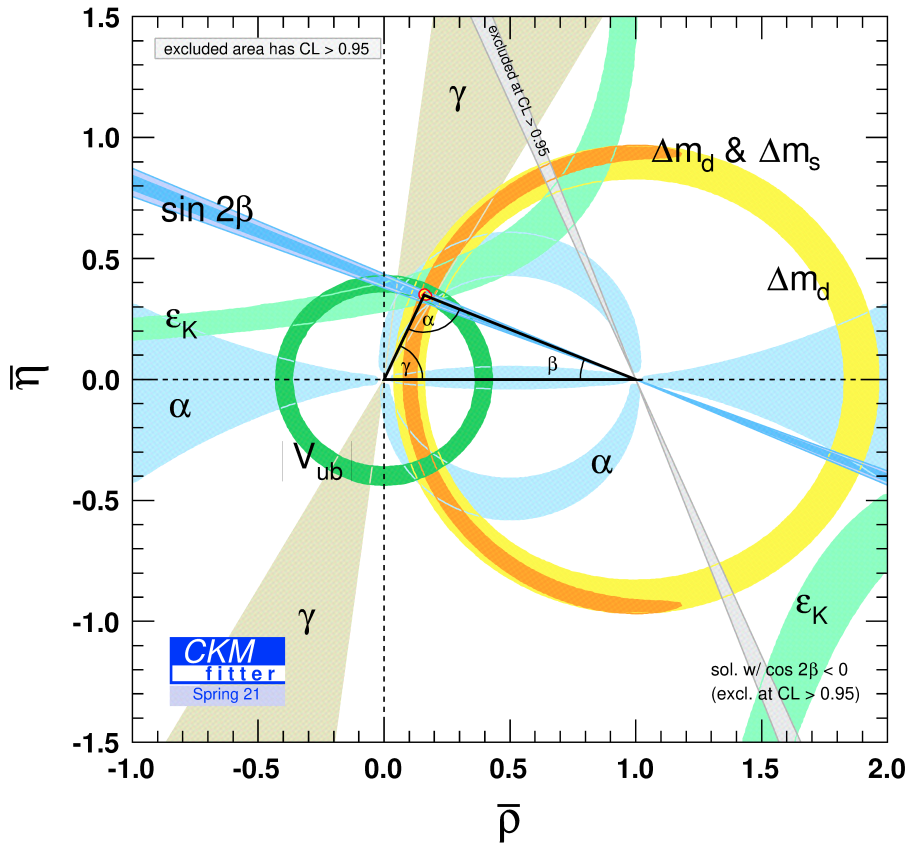

Figure 1.3: Measured values of the most common unitarity triangle expressed in the $\bar{\rho} - \bar{\eta}$ plane. Plot taken from [21] in which the most up to date results can be found.

1.2 Kaon physics

In 1947 whilst studying cosmic ray events in cloud-chamber photographs, Butler and Rochester observed the tracks of two particles which did not behave as expected [22]. They observed two types of events: a new uncharged particle decaying into two lighter, charged particles, and secondly a charged particle decaying into a lighter charged particle and uncharged particle. It is now understood that this was the first discovery of the kaon with the former, neutral, particle decaying into two pions.

A similar neutral particle was observed in 1949 however this time it was shown to be decaying into three pions leading to the tau-theta problem in which the same particle is observed decaying into conflicting parity final states [23]. Whilst it was discovered that parity was violated by weak interactions in 1956 [24], it was thought that the combination of charge parity (CP) symmetry would be instead conserved. A K_S^0 (k-short) particle would decay into two pions with $CP = +1$, whilst a K_L^0 (k-long) particle decays into three pions with $CP = -1$ thus serving the illusion that CP is conserved. These mass eigenstates are so-called after their respective lifetimes three orders of magnitude apart.

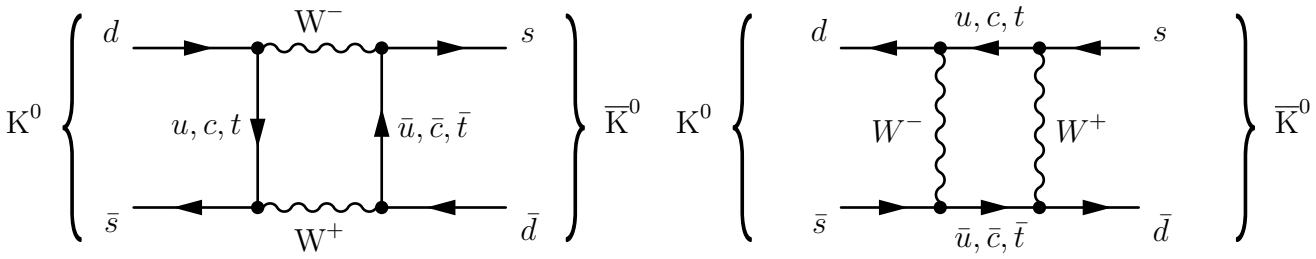

Figure 1.4: Feynman diagrams for $K^0 - \overline{K}^0$ mixing.

Later, in 1964, it was found that the K_L^0 was also able to decay into two pions and thus CP symmetry was in fact violated [25]. This decay occurs via neutral kaon mixing and is known as indirect CP violation. The K^0 and $\overline{K}^0$ produced by the strong interaction can transform spontaneously between themselves via a weak interaction box diagram, see Figure 1.4. The CP eigenstates, K_1 and K_2, are the

linear combinations of K^0 and $\overline{K}^0$:

$$K_1 = \frac{1}{\sqrt{2}}(K^0 - \overline{K}^0) \quad \text{and} \quad K_2 = \frac{1}{\sqrt{2}}(K^0 + \overline{K}^0), \tag{1.10}$$

with $CP(K_1) = CP(2\pi) = +1$ and $CP(K_2) = CP(3\pi) = -1$. To allow for this indirect CP violation, we find that the mass eigenstate K_L^0 is not a pure sample of K_2 but instead a combination of K_1 and K_2:

$$K_L^0 = \frac{1}{\sqrt{1+\epsilon^2}}(K_2 + \epsilon K_1), \tag{1.11}$$

with ϵ characterising the amount of indirect CP violation. Similarly,

$$K_S^0 = \frac{1}{\sqrt{1+\epsilon^2}}(K_1 + \epsilon K_2). \tag{1.12}$$

Direct CP violation, in which the kaon violates CP whilst decaying rather than via mixing has also been observed but not until the 1990's by the NA31, NA48, and KTEV experiments [9–11].

Some additional contributions to the SM that have originated through the study of kaon decays are: the indirect discovery of the charm quark through the measured supression of the $K_L^0 \to \mu^+\mu^-$ decay in comparison to the $K_L^0 \to \gamma\gamma$ decay in 1974 [7]; and tests of lepton flavour universality by studying the ratio of the $K^\pm \to e^\pm\nu$ and $K^\pm \to \mu^\pm\nu$ decays [26, 27].

This thesis describes work performed with the NA62 experiment using a hadron beam of which 6% are kaons. Table 1.1 shows the properties of the charged and neutral kaons along with Table 1.2 showing the six most dominant decays of the positive kaon. The NA62 experiment, described further in chapter 2, utilises a 75 GeV/c momentum hadron beam resulting in the mean distance travelled by a kaon of ~ 564 m; it is expected that only 10% of kaons will decay inside the fiducial

volume. The main goal of the NA62 experiment is the measurement of the ultra-rare $K^+ \to \pi^+ \nu\bar{\nu}$ decay discussed further in the following section.

Table 1.1: Properties of charged and neutral kaons [18].

Particle	Quark content	Mass (MeV/c^2)	Lifetime (s)
K^+	$u\bar{s}$	493.677 ± 0.016	$(1.2380 \pm 0.0020) \times 10^{-8}$
K^-	$\bar{u}s$	493.677 ± 0.016	$(1.2380 \pm 0.0020) \times 10^{-8}$
K^0	$d\bar{s}$	497.611 ± 0.013	n/a
K_S^0	$\frac{d\bar{s}-s\bar{d}}{\sqrt{2}}$	497.611 ± 0.013	$(0.8954 \pm 0.0004) \times 10^{-10}$
K_L^0	$\frac{d\bar{s}+s\bar{d}}{\sqrt{2}}$	497.611 ± 0.013	$(5.116 \pm 0.021) \times 10^{-8}$

Table 1.2: Predominant K^+ modes with their branching ratios [18].

Decay	Branching ratio [%]
$K^+ \to \mu^+ \nu$	63.56 ± 0.11
$K^+ \to \pi^+ \pi^0$	20.67 ± 0.08
$K^+ \to \pi^+ \pi^+ \pi^-$	5.583 ± 0.024
$K^+ \to \pi^0 e^+ \nu$	5.07 ± 0.04
$K^+ \to \pi^0 \mu^+ \nu$	3.352 ± 0.033
$K^+ \to \pi^+ \pi^0 \pi^0$	1.760 ± 0.023

1.3 $K^+ \to \pi^+\nu\bar{\nu}$ theory

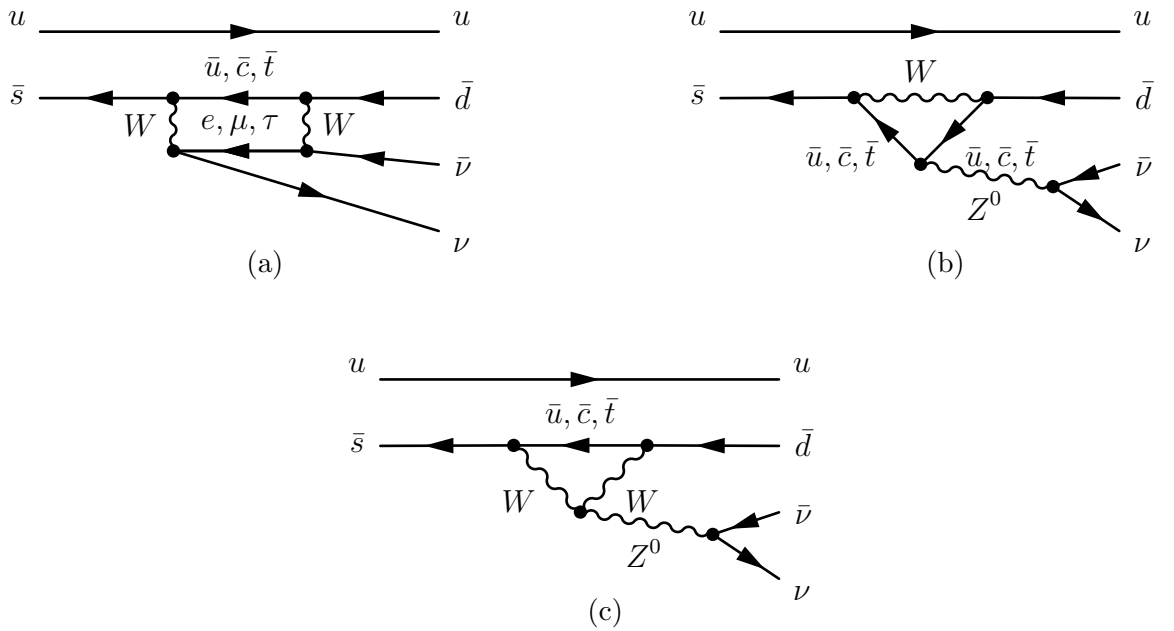

Figure 1.5: Feynman diagrams for the $K^+ \to \pi^+\nu\bar{\nu}$ decay.

The $K^+ \to \pi^+\nu\bar{\nu}$ decay proceeds, at the lowest order in the SM, through electroweak box and penguin diagrams, see Figure 1.5. These are Flavour Changing Neutral Current (FCNC) processes and in each diagram, all of the three positively charged quarks can run in the loops. The contribution of each quark with mass, m_q, to the decay amplitude can be expressed as:

$$A_q \approx \frac{m_q^2}{m_W^2} V_{qs}^* V_{qd}, \tag{1.13}$$

with CKM parameters V_{qs}, V_{qd} and accounting for the propagating W boson mass, m_W. Hence the $K^+ \to \pi^+\nu\bar{\nu}$ decay is dominated by the exchange of a top quark. Due to GIM suppression [28] and the $t \to d$ transition, this process is highly suppressed.

After summation of the lepton flavours in each of the Feynman diagrams, an approximation of the branching ratio of the $K^+ \to \pi^+\nu\bar{\nu}$ decay using the Wolfenstein

parametrisation is given by [29, 30]:

$$\begin{aligned}\mathcal{B}(K^+ \to \pi^+\nu\bar{\nu}) =&(1+\Delta_{\mathrm{EM}})\frac{\kappa_+}{\lambda^8}|V_{cb}|^4 X(x_t)^2 \quad \times \\ &\left[\sigma R_t^2 \sin^2\beta + \frac{1}{\sigma}\left(R_t\cos\beta + \frac{\lambda^4 P_c(X)}{|V_{cb}|^2 X(x_t)}\right)^2\right].\end{aligned} \tag{1.14}$$

Here:

- λ originates from the Wolfenstein parametrisation of the CKM matrix and is equal to the parameter $|V_{us}|$. Additionally, the parameter σ is also a function of λ through the formula,

$$\sigma = \left(\frac{1}{1-\frac{\lambda^2}{2}}\right)^2. \tag{1.15}$$

- Δ_{EM} describes the long-distance radiative Quantum ElectroDynamics (QED) corrections whilst κ_+ contains the higher order electroweak corrections to the low-energy matrix elements [31]. Next-to-leading order (NLO) and partial next-to-next-to-leading order (NNLO) calculations in Chiral Perturbation theory (ChPT) of these contributions have been performed with the value of Δ_{EM} given below along with κ_+ written in terms of λ [32]:

$$\Delta_{\mathrm{EM}} = -0.003, \tag{1.16}$$

$$\kappa_+ = (5.173 \pm 0.025)\times 10^{-11}\left[\frac{\lambda}{0.225}\right]^8. \tag{1.17}$$

- $x_t = m_t^2/m_W^2$ describes the ratio of the top quark mass to the W boson mass with $X(x_t)$ and $P_c(X)$ being the loop functions for the top and charm quark contributions respectively. The most recent value of the top quark contributions is $X(x_t) = 1.462 \pm 0.017_{\mathrm{QCD}} \pm 0.002_{\mathrm{EW}}$ after including NLO QCD corrections [33, 34] and NLO electroweak corrections [35]. The charm quark contribution

can be expressed as:

$$P_c(X) = P_c^{\text{SD}}(X) + \delta P_{c,u}, \qquad \delta P_{c,u} = 0.04 \pm 0.02, \tag{1.18}$$

with P_c^{SD} describing the short-distance contributions and $\delta P_{c,u}$ the long-distance contributions calculated in [36]. We find using $\lambda = 0.2252$ that

$$P_c^{\text{SD}}(X) = 0.365 \pm 0.012, \tag{1.19}$$

and adding the long-distance contribution results in [37]:

$$P_c(X) = 0.404 \pm 0.024, \tag{1.20}$$

in which the errors have been added in quadrature.

- The parameters R_t and β are defined in the unitarity triangle shown in Figure 1.6. The sides R_t and R_b are defined as:

$$R_t \equiv \frac{|V_{td}V_{tb}^*|}{|V_{cd}V_{cb}^*|}, \quad R_b \equiv \frac{|V_{ud}V_{ub}^*|}{|V_{cd}V_{cb}^*|} \tag{1.21}$$

and can be expressed solely in terms of the angles β and γ:

$$R_t = \frac{\sin\gamma}{\sin(\beta+\gamma)}, \quad R_b = \frac{\sin\beta}{\sin(\beta+\gamma)} \tag{1.22}$$

Similarly, one can obtain an expression for the $K_L^0 \to \pi^0\nu\bar{\nu}$ decay which proceeds through the same Feynman diagrams as the $K^+ \to \pi^+\nu\bar{\nu}$ decay, see Figure 1.5, however the spectator quark is changed from an up quark to a down quark:

$$\mathcal{B}(K_L^0 \to \pi^0\nu\bar{\nu}) = \kappa_L |V_{cb}|^4 \Big[\frac{\lambda\sqrt{\sigma}\sin\beta\sin\gamma}{\lambda^5} X(x_t)\Big]^2, \tag{1.23}$$

where,

$$\kappa_L = (2.231 \pm 0.013) \times 10^{-10} \left[\frac{\lambda}{0.225}\right]^8. \tag{1.24}$$

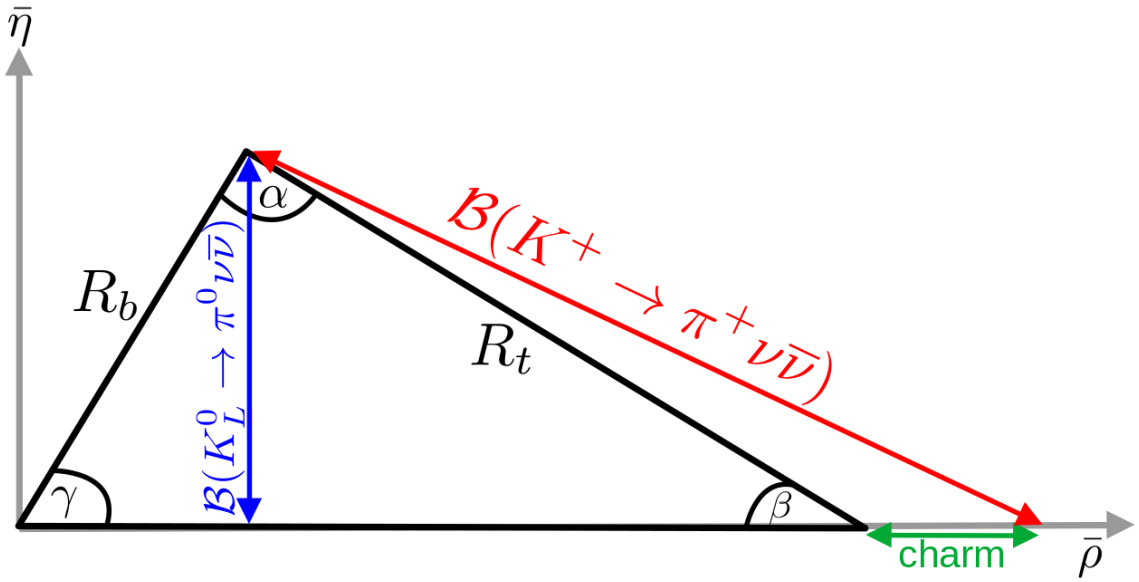

Figure 1.6: Illustration showing the relationship of the $K^+ \to \pi^+\nu\bar{\nu}$ and $K_L^0 \to \pi^0\nu\bar{\nu}$ decays on the unitarity triangle. The sides R_t and R_b are also defined.

By placing the measured values into Equations 1.14 and 1.23, one obtains [37]:

$$\begin{aligned} \mathcal{B}(K^+ \to \pi^+\nu\bar{\nu}) &= (8.4 \pm 1.0) \times 10^{-11}, \\ \mathcal{B}(K_L^0 \to \pi^0\nu\bar{\nu}) &= (3.4 \pm 0.6) \times 10^{-11}. \end{aligned} \tag{1.25}$$

The components contributing the most to the uncertainty of this measurement are the CKM parameter $|V_{cb}|$, and the unitarity triangle angle γ. A diagram showing each parameters contribution to the error budget is shown in Figure 1.7. It is therefore desirable to try to recalculate these branching ratios after removing the $|V_{cb}|$ dependence. Consequently, the latest SM predictions for both of these decays are [29]:

$$\begin{aligned} \mathcal{B}(K^+ \to \pi^+\nu\bar{\nu})^{\mathrm{SM}} &= (8.60 \pm 0.42) \times 10^{-11}, \\ \mathcal{B}(K_L^0 \to \pi^0\nu\bar{\nu})^{\mathrm{SM}} &= (2.94 \pm 0.15) \times 10^{-11}. \end{aligned} \tag{1.26}$$

Each of the branching ratios can also be written explicitly as a function of the

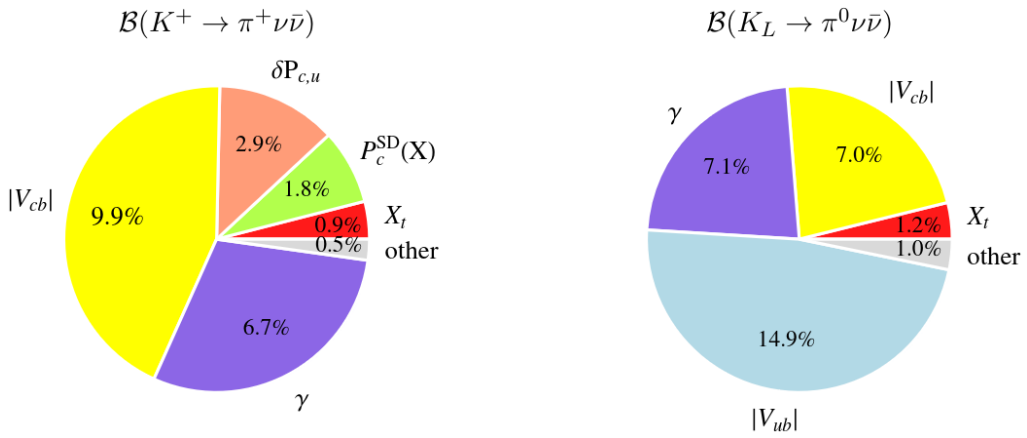

Figure 1.7: Error budget on the theoretical branching ratios of the $K^+ \to \pi^+\nu\bar{\nu}$ and $K_L^0 \to \pi^0\nu\bar{\nu}$ decays. Figure taken from [37].

CKM parameters contributing the most to the uncertainty [29]:

$$\mathcal{B}(K^+ \to \pi^+\nu\bar{\nu}) = (7.92 \pm 0.28) \times 10^{-11} \left(\frac{|V_{cb}|}{41.0 \times 10^{-3}} \right)^{2.8} \left(\frac{\sin\gamma}{\sin 73.2^\circ} \right)^{1.39}, \quad (1.27)$$

where the explicit dependence on λ has been removed and set to $\lambda = 0.225$.

The experimentally measured results for the branching ratio of both the $K^+ \to \pi^+\nu\bar{\nu}$ and $K_L^0 \to \pi^0\nu\bar{\nu}$ decay are as follows:

$$\begin{aligned} \mathcal{B}(K^+ \to \pi^+\nu\bar{\nu})^{\text{NA62}} &= (10.6^{+4.0}_{-3.4}|_{\text{stat}} \pm 0.9_{\text{syst}}) \times 10^{-11}, \\ \mathcal{B}(K_L^0 \to \pi^0\nu\bar{\nu})^{\text{KOTO}} &\leq 3.0 \times 10^{-9} \qquad @\ 90\%\ C.L., \end{aligned} \quad (1.28)$$

as measured by the NA62, using NA62 run-1 data (2016-2018), [12] and KOTO, using data collected in 2015, [38] experiments respectively. Upgrades to both of these detectors since the publications of these results have been performed with more precise results expected from their larger datasets. Further details of the $K^+ \to \pi^+\nu\bar{\nu}$ measurement, and in particular the single event sensitivity for data collected in 2021, are provided in chapter 5.

Chapter 2

The NA62 experiment

The NA62 experiment, located in the CERN North Area, is designed to measure the rare decays of kaons, and in particular the branching ratio of the $K^+ \to \pi^+\nu\bar{\nu}$ decay. Moreover, the physics programme at NA62 includes additional searches for rare decays along with precision measurements, searches for exotic particles and decays forbidden by the SM. For the full NA62 run-1 results (data collected between 2016 and 2018), see [12, 39–50].

A full description of the NA62 beam and detector can be found in [51] whilst this information is summarised below in sections 2.1 and 2.2. Updates to the detector between NA62 run-1 and NA62 run-2 (data collected between 2021 and 2025) can be found in [52–57] and also highlighted in the subsequent sections. The trigger, section 2.3, and simulation framework, section 2.4 are also described.

The coordinate system used when discussing the NA62 detector is defined such that the beam line defines the z axis with its origin at the kaon production point. Beam particles travel in the positive z-direction. The y axis points vertically upwards whilst the x axis is horizontal and directed such that a right-handed coordinate system is formed. Additionally, the phrase 'upstream' ('downstream') either refers

to the negative (positive) z-direction or to the region $z < 102.4\,\mathrm{m}$ ($z > 102.4\,\mathrm{m}$).

2.1 The NA62 beam

The NA62 beam originates from $400\,\mathrm{GeV}/c$ protons extracted from the SPS hitting a beryllium target known as T10. The secondary hadron beam produced at the T10 target is referred to as the K12 beam with a central momentum value of $75\,\mathrm{GeV}/c$, selected to maximise the fraction of kaons decaying in the fiducial volume per proton on target. A schematic of the K12 beam line can be seen in Figure 2.1.

After T10, a 950 mm long water-cooled copper collimator with a choice of different aperture bores selects the secondary particles; a 15 mm hole is normally used. A set of three quadrupole magnets (Q1, Q2, and Q3) are used to collect the beam with a large solid angle acceptance. Following this, the beam passes through an achromat (A1) to select the beam with a central momentum of $75\,\mathrm{GeV}/c$ and a root mean square (RMS) of 1%. The achromat is composed of four vertically displacing dipole magnets; the first two displacing the $75\,\mathrm{GeV}/c$ beam downwards by 110 mm from the beam axis, and the second two returning the beam to its original axis. Between the two sets of dipole magnets are a set of graduated holes in two beam-dump units (TAX1 and TAX2), which make the momentum selection and absorb the remaining proton beam along with any unwanted secondary particles. In between TAX1 and TAX2, a tungsten radiator is introduced, optimised to cause positrons to lose enough energy via Bremsstrahlung such that they can be rejected [51].

An additional three quadrupoles (Q4, Q5, and Q6) refocus the beam whilst the collimators (C1 and C2) limit the vertical and horizontal acceptance. Positrons interacting with the tungsten radiator between TAX1 and TAX2 have now lost sufficient energy that they are absorbed by the C3 collimator. The beam then passes

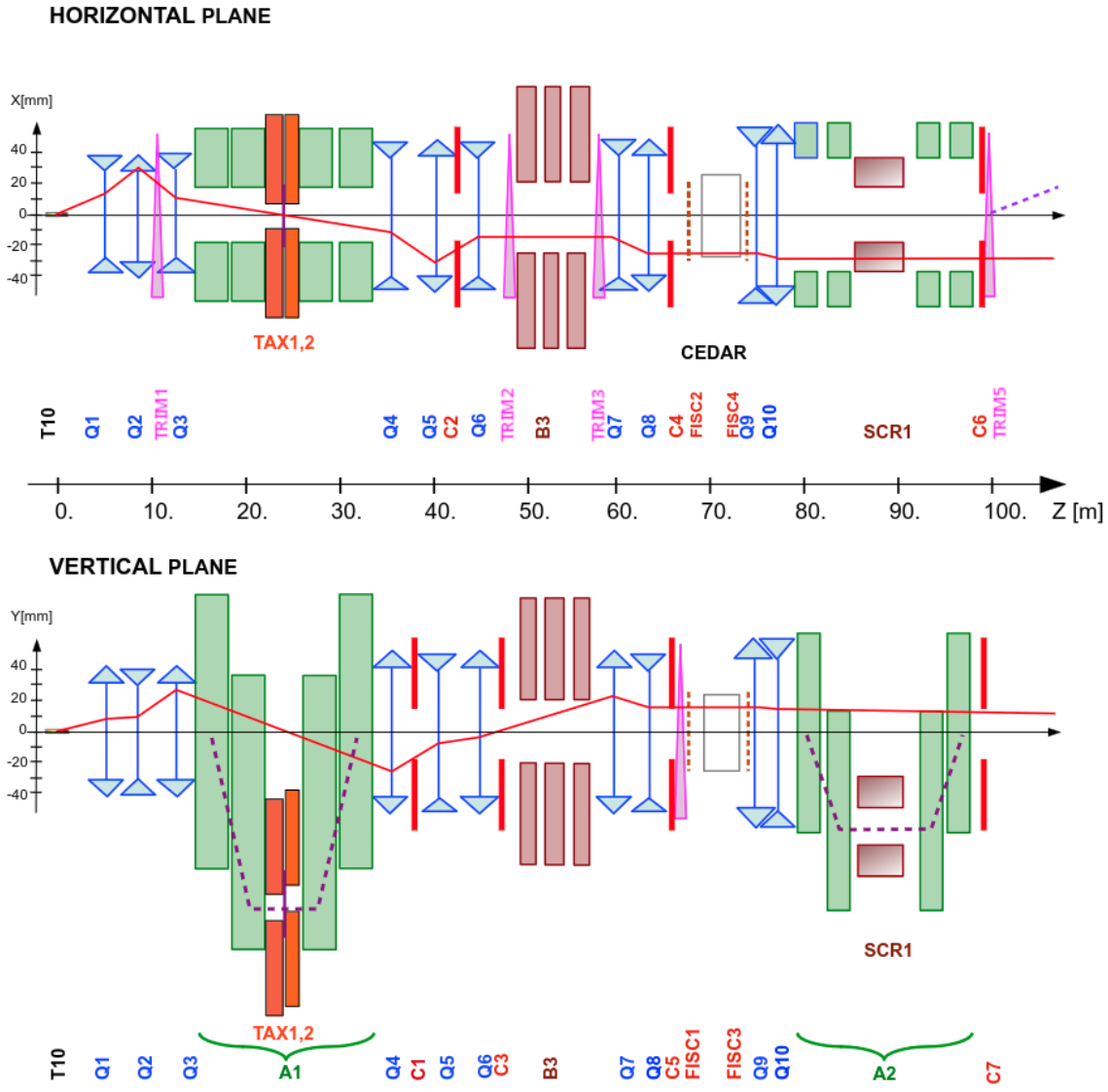

Figure 2.1: Schematic of the K12 beam line originating from the fixed beryllium target (T10) up to the decay region. The solid line in each view corresponds to the trajectory of a particle leaving the centre of T10 at the angle specified at nominal momentum. The dashed line indicates the path of an initially on-axis particle at a momentum of 75 GeV/c. Figure modified from [51].

through three dipole magnets (B3), each 2 m long with iron plates between them. A 40 mm, almost field-free, bore is present for the beam to pass through whilst the vertical magnetic field in the iron sweeps any positive or negative muons. TRIM2 and TRIM3, steering dipoles, cancel any deviations of the beam due to stray fields inside the bore.

The CEDAR detector, described further in subsection 2.2.1 and chapter 3, requires the beam to be parallel and as such is preceded by two more quadrupoles (Q7 and Q8). Cleaning collimators (C4 and C5) absorb particles in the tails of the beam. Filament scintillator counters (FISC) surround the CEDAR to measure the beam divergence; FISC1 and FISC3 measure the vertical plane whilst FISC2 and FISC4 measure the horizontal plane [51].

More quadrupoles (Q9 and Q10) follow the CEDAR focusing the beam into the GTK detector, described further in subsection 2.2.2 and depicted in Figure 2.2. In NA62 run-1, the GTK detector was composed of three stations with an achromat (A2) occupying the space between GTK1 and GTK3.[1] An iron collimator (SCR1) defocuses muons which later leave the beam between the second and third magnets of the achromat. GTK2 is situated just after SCR1 where the 75 GeV/c beam has a downward displacement of 60 mm whilst remaining parallel to the beam axis. Two cleaning collimators (C6 and C7), visible in Figure 2.1, are situated before GTK3 to intercept background outside of the beam acceptance.

A horizontal steering magnet (TRIM5) is used to deflect the beam in the positive x-direction by an angle of 1.2 mrad before it enters the decay region. The kick in positive x is such that the subsequent, 3.6 mrad, deflection in negative x by the MNP33 magnet downstream directs the beam through the central aperture of the LKr calorimeter and subsequent detectors. Table 2.1 describes the main parameters of the K12 beam as it reaches the decay volume.

[1] An additional station, GTK0, was added upstream of GTK1 for NA62 run-2.

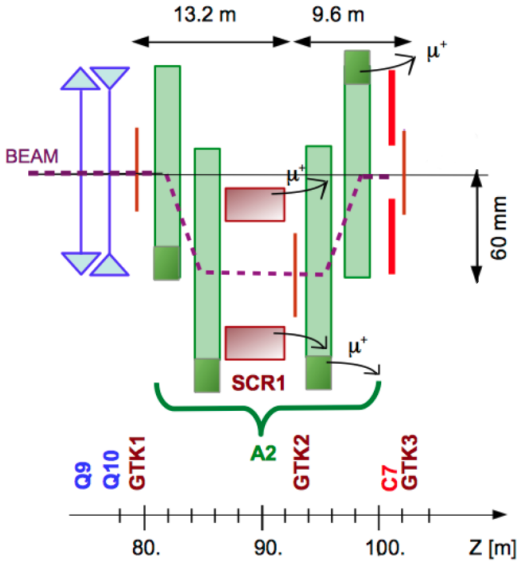

Figure 2.2: Schematic of the second achromat in the K12 beam line (Y vs Z view) situated between GTK1 and GTK3. The beam is deflected vertically downards by 60 mm for the momentum measurement before being returned to its nominal direction. The scraper SCR1 sweeps away muons from the beam. Figure adapted from [51].

As seen in Figure 2.3, a 117 m long vacuum tank is situated after GTK3, 102.4 m downstream of T10, with a residual pressure of $\sim 10^{-6}$ mbar marking the start of the decay volume. The fiducial decay volume is normally defined to be 60 m long however variations of this definition are used depending on the decay topology and backgrounds under study. The vacuum tank holds 11 stations of LAV detectors, section 2.2.7, and four STRAW chambers, subsection 2.2.5. At the downstream end of the tank, a 2 mm thick aluminium window separates the vacuum tank from the neon gas in the RICH detector, subsection 2.2.6. Attached to this window is a thin-walled aluminium tube, allowing the undecayed beam particles to continue to travel through vacuum. Following the MUV3, subsection 2.2.9, the beam is deflected further towards the negative x-direction by a dipole magnet such that it does not impinge on the SAC detector, section 2.2.7. Finally, any undecayed particles in the beam are absorbed by the beam-dump.

Table 2.1: K12 beam parameters at nominal intensity according to the NA62 design specifications. Table has been adapted from [51].

Protons on target (T10) in 1s of spill		1.1×10^{12}
Beam Acceptance	Horizontal	± 2.7 mrad
	Vertical	± 1.5 mrad
K^+ momentum	mean	75 GeV/c
	$\Delta p/p$ (RMS)	1.0%
Instantaneous beam rates	K^+	45 MHz (6%)
	p	173 MHz (23%)
	π^+	525 MHz (70%)
	μ^+	$\sim$5 MHz (<1%)
Estimated K^+ decays per year (assuming 100 days data taking)		5×10^{12}

2.2 Detectors

The NA62 detector has been specifically designed for the measurement of the branching fraction of the $K^+ \to \pi^+ \nu\bar{\nu}$ decay requiring precise timing, kinematic rejection, particle identification and hermetic vetoing of photons. A schematic of the detector layout for NA62 run-2 can be seen in Figure 2.3 where it remains largely unchanged from that in NA62 run-1. The remainder of this section will focus in on each of the subdetectors and the role they play in in the $K^+ \to \pi^+ \nu\bar{\nu}$ measurement as well as in other measurements and searches performed at NA62. Table 2.2 shows the role of each subdetector.

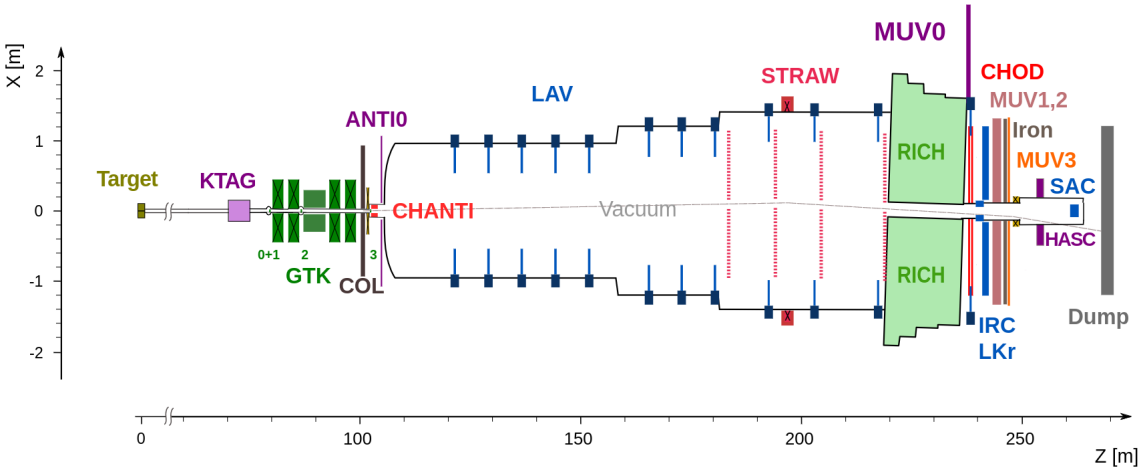

(a) x vs z view.

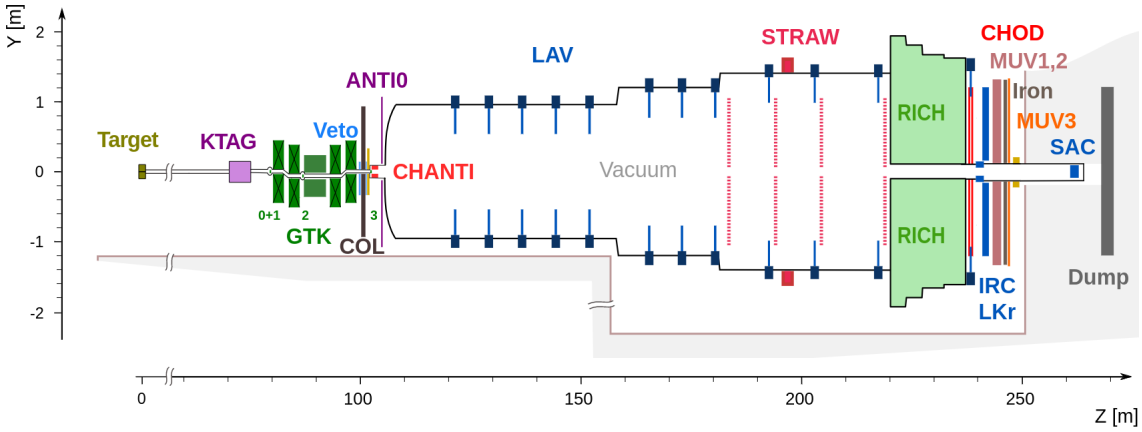

(b) y vs z view.

Figure 2.3: Schematic of the NA62 detector for run-2 data collection. All of the subdetectors, most of which are approximately cylindrical in shape, are labelled and shall be discussed further in this section. In addition to the run-1 layout, an additional GTK station, the Vetocounter (labelled Veto), ANTI0, and a second HASC station have been added.

Table 2.2: Summary table of the NA62 subdetectors.

Role	Detector	Primary purpose
Timing	NA48-CHOD	Measures time of charged downstream tracks.
	CHOD	Measures time of charged downstream tracks.
Tracking	GTK	Measurements of beam momentum, direction and timing.
	STRAW	Measurements of charged decay products momenta. Also aids in PID when combined with information from the LKr.
Particle identification (PID)	KTAG	Identification of kaons in the beam along with time-stamping them.
	RICH	Identification of downstream charged tracks.
Muon Vetoes	MUV1/2	Identification of pions and muons.
	MUV3	Identification of muons.
Photon vetoes	LAV	Detects photons emitted at angles 8.5-50 mrad.
	LKr	Detects photons emitted at angles 1-8.5 mrad. Also provides energy measurements of decay particles and aids in PID.
	IRC/SAC	Detects photons emitted at angles 0-1 mrad.
Other background rejection	CHANTI	Detects inelastic scattering of the beam in GTK3.
	MUV0	Detects π^- from $K^+ \to \pi^+\pi^-\pi^+$ decays that are outside the STRAW acceptance.
	HASC	Detects π^+ from $K^+ \to \pi^+\pi^-\pi^+$ decays that are outside the STRAW acceptance.
	Veto counter	Detection of upstream decays.
	ANTI-0	Detection of the muon halo which may enter the decay volume resulting in a signal event being rejected.

2.2.1 The kaon tagging system

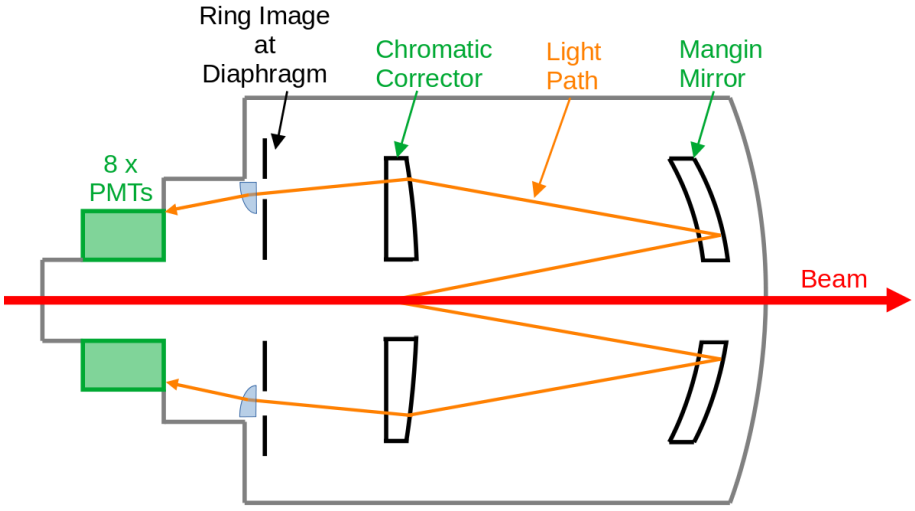

Figure 2.4: Schematic of an original CEDAR showing the path of two photons emitted from a beam particle through the optical components. For NA62, the 8 photomultiplier tubes (PMTs) have been replaced by 8 sectors of 48 PMTs as part of the KTAG upgrade. Figure reproduced from [58].

To identify the kaons in the unseparated beam, a precise tagging system is required. The CEDAR [59] is a Cherenkov differential counter with achromatic ring focus, exploiting that particles at the same momenta, i.e 75 GeV/c, will emit Cherenkov radiation at an angle based on their mass. In this case, a series of mirrors and lenses can be used to focus the light emitted at the kaon angle into a narrow ring and consequently collected by an aperture excluding light from the other particles.

The CEDAR is a $\sim$5 m long vessel situated along the beam line at a position of $z = 69.3$ m. Historically, there are two types of CEDAR vessels: a Cedar-W detector, designed to be used with nitrogen gas as a radiator, capable of separating kaons from pions up to momentum values of 150 GeV/c; and a Cedar-N detector, designed for use with helium gas, working with momentum values up to 300 GeV/c. Up until 2022, NA62 utilised a Cedar-W detector with nitrogen gas at 1.75 bar. As a direct consequence of the work carried out in this thesis, from 2023, a newly built CEDAR detector, using hydrogen gas as the radiator at 3.80 bar, was commissioned and used at NA62.

A schematic of an original CEDAR can be seen in Figure 2.4. NA62 required the timing resolution of the CEDAR to be $< 100\,\text{ps}$ and found the original CEDAR design to be ineffective. An upgraded design called KTAG [60], in which the 8 PMTs were replaced by 8 sectors each containing 48 PMTs was comissioned for NA62 run-1. Whilst each KTAG PMT has a time resolution of $\sim 300\,\text{ps}$, as approximately 18 photons are detected per kaon with the KTAG, a time resolution of 70 ps is achieved. Additionally, with the requirement that a kaon must have a coincident signal in at least 5 sectors, an efficiency of $> 98\%$ is observed. Further details about the operation of CEDAR and KTAG, along with changing the radiator gas to hydrogen and the corresponding performances are discussed in chapter 3.

2.2.2 The GigaTracker spectrometer

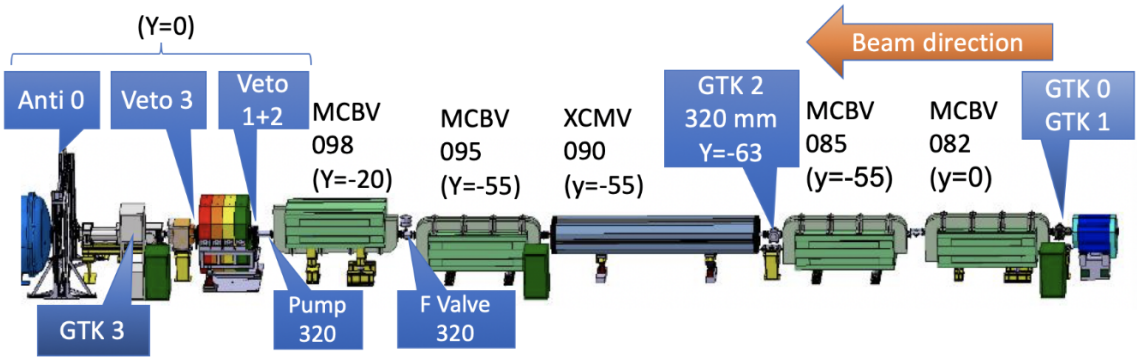

Figure 2.5: Schematic of the GTK station layout for the NA62 run-2 data-taking period [55].

In addition to tagging the kaons in the beam, a measurement of the momentum and direction of all particles in the beam is crucial in reaching the required kinematic rejection level for the $K^+ \to \pi^+\nu\bar{\nu}$ analysis. This is achieved by a silicon pixel detector referred to as the GigaTracker (GTK). For NA62 run-1, three GTK stations were located around four dipole magnets arranged as an achromat with the vertical displacement in the second station used to measure the particle momentum. An upgrade of the GTK detector was performed in 2021 in which an additional

GTK station was added upstream of GTK1 with the aim of reducing the upstream background. A diagram of such an arrangement can be seen in Figure 2.5.

To minimise material in the beam line, the GTK is made of pixels of size $300 \times 300\,\mu m^2$ and $500\,\mu m$ thickness corresponding to a material budget of $< 0.5X_0$ for each station. Additionally, a time resolution better than 200 ps allows the GTK to handle the high beam particle rate of 750 MHz in NA62 [61]. The GTK detector achieves a precision on the particle momenta of 0.2% and on the angular momentum of $16\,\mu rad$.

2.2.3 The upstream vetocounters

Random veto, accidental activity in the NA62 detector causing a signal event to be vetoed, is a large concern for the $K^+ \to \pi^+\nu\bar{\nu}$ measurement. Halo particles (mostly muons) can enter the decay volume close in time to a tagged beam kaon in which case they may contribute to this random veto. The ANTI-0 [62], a cell structure hodoscope added for NA62 run-2, is placed just in front of the vacuum tank with the aim of vetoing such events. To achieve this task, 280 plastic scintillator counters are placed in a chessboard-like manner, see Figure 2.6, and read out by silicon photomultipliers (SiPMs). A time resolution of less than 1 ns is achieved to reduce the effects of random veto.

A source of upstream background occurs from decays happening before the fiducial volume. The VetoCounter, formed of three parallel planes of scintillator tiles and a photon conversion lead plate was added to the NA62 detector for NA62 run-2 to detect such events. More information on the readout and performances of the VetoCounter can be found in [63].

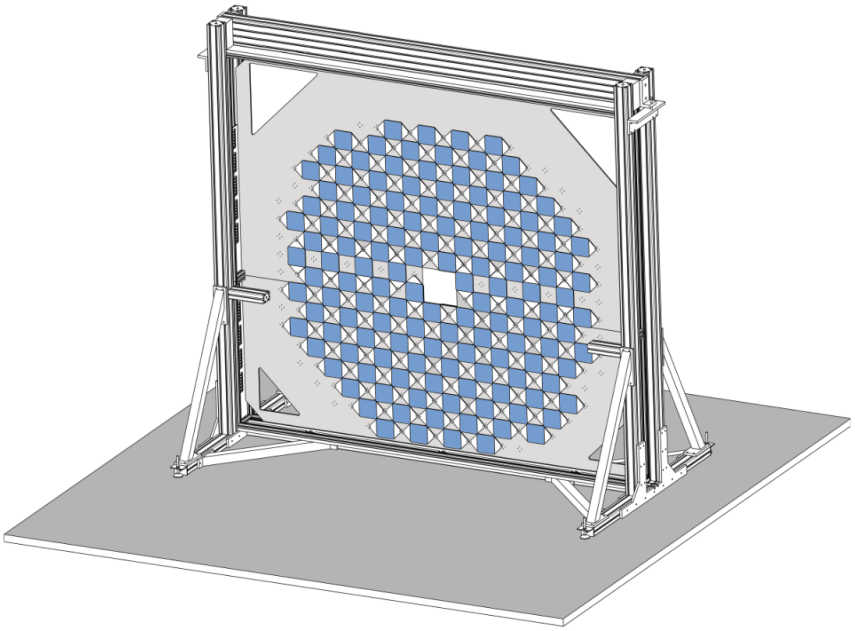

Figure 2.6: Schematic of the ANTI-0 [62].

2.2.4 The charged anti-coincidence detector

Inelastic scattering can occur as the beam passes through the GTK, and if not properly accounted for can mimic a $K^+ \to \pi^+ \nu\bar{\nu}$ signal. Whilst inelastic scattering from the first two stations is not an issue due to the collimator and magnet yokes, scattering from GTK3 is an issue. Six square hodoscope stations, called CHANTI, each $300 \times 300\,\mathrm{mm}^2$ in cross-section with a hole of $95 \times 65\,\mathrm{mm}^2$ for the beam are used to detect such events [64]. In addition to the inelastic scattering, the muon halo close to the beam and a fraction of charged particles from early decays upstream of GTK3 can also be detected by the CHANTI.

The first station is placed at a distance of 28 mm from GTK3 with the distance between stations becoming successively further. With this approach, an angular region of 49 mrad and 1.34 rad is covered; angles less than 49 mrad are detected by the photon veto system, see subsection 2.2.7. A single channel time resolution of 1.14 ns, a spatial resolution of ~ 2.5 mm, and an efficiency greater than 99% is achieved [65].

2.2.5 The STRAW spectrometer

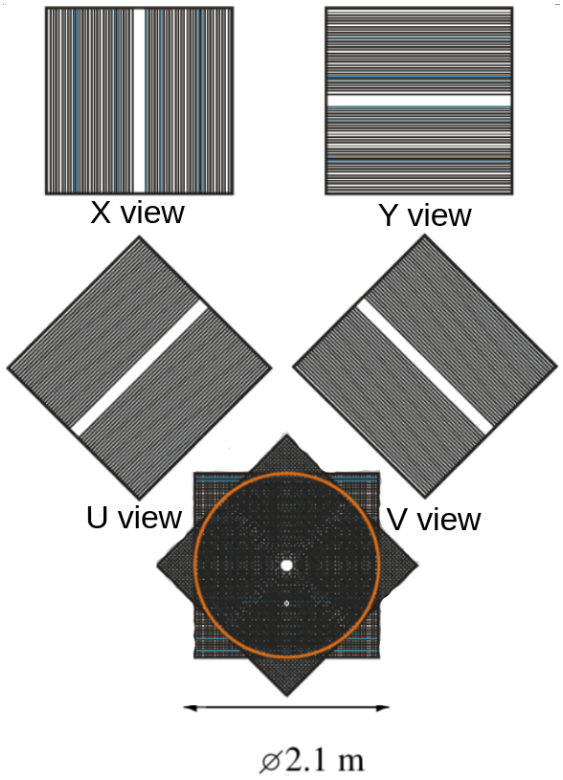

(a) The X,Y and U STRAW views. Additionally, an image of all 4 views overlaid on top of each other is shown in the bottom right.

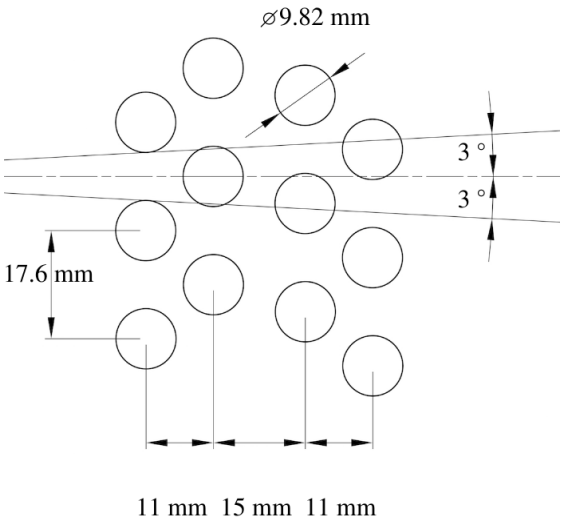

(b) The arrangement of straws inside each view. There are four layers and a track is guaranteed to pass through at least two straws.

Figure 2.7: Schematic of the STRAW highlighting the four different views and the arrangment of the four layers in each view.

The tracking of decay particles and measurement of their direction and momentum is performed by the STRAW spectrometer [66]. The STRAW is composed of four chambers and a large aperture dipole magnet (MNP33), situated between chambers 2 and 3, providing a vertical magnetic field of 0.36 T. To minimise multiple scattering of the charged decay products, the STRAW chambers are installed inside the vacuum tank and correspond to 1.8% X_0.

Each chamber has 4 views (X, Y, U, and V), see Figure 2.7a, with each view composed of 4 layers of parallel drift tubes (straws), see Figure 2.7b. These layers are formed of such a pattern that ensures the geometrical coverage for tracks with

an angle of up to 3 degrees from the normal to the view plane. In addition, each view has a gap of $\sim 12\,\text{cm}$ such that when overlaying the views at an angle of 45°, an octagon shaped hole of 6 cm apothem is created for the beam to pass through. This hole is not actually centred in each chamber but placed to accommodate the beam trajectory deflected by the TRIM5 and MNP33 magnets.

The resolution on the track momentum as measured by the STRAW is [51]:

$$\frac{\sigma_p}{p} = 0.300\% \oplus 0.005\% \cdot p, \tag{2.1}$$

dependent on the particles momentum, p, measured in GeV/c. The angular resolution at a momentum of $10\,\text{GeV}/c$ is $60\,\mu\text{rad}$ whilst this improves to $20\,\mu\text{rad}$ at $50\,\text{GeV}/c$. The measured time resolution is $\sim 6\,\text{ns}$.

2.2.6 The ring imaging Cherenkov counter

Whilst the KTAG detector provides particle identification for kaons in the beam, a ring imaging Cherenkov counter, RICH, provides particle identification for the charged decay particles downstream [67]. The RICH is a 17.5 m long cylindrical vessel filled with neon gas at room temperature and atmospheric pressure. Its main aim is to distinguish pions from muons in the 15–40 GeV/c range for the $K^+ \to \pi^+\nu\bar{\nu}$ analysis.

Mirrors at the downstream end of the vessel reflect the Cherenkov light cone back towards two photodetector planes each containing an array of 976 PMTs. For the $K^+ \to \pi^+\nu\bar{\nu}$ measurement, the identification of positive particles over negative particles is more critical. Hence the RICH mirrors are tilted with respect to the beam axis so they better align with the positive particles deflected by the MNP33 magnet. Moreover, the central axis of the RICH is also angled such that the beam

passes through after its deflection by MNP33.

Particles passing through the RICH have different velocities and therefore produce Cherenkov rings of different radii, see Figure 2.8. Using this information along with the number of photons detected, pions and muons can be separated up to a momentum of $\sim$40 GeV/c and this provides a limiting value for the π^+ in the $K^+ \to \pi^+\nu\bar{\nu}$ analysis. The time resolution of the RICH is $\sim$70 ps and is used as a reference time for the trigger. When combined with the CHOD, see subsection 2.2.8, this forms the minimum bias trigger.

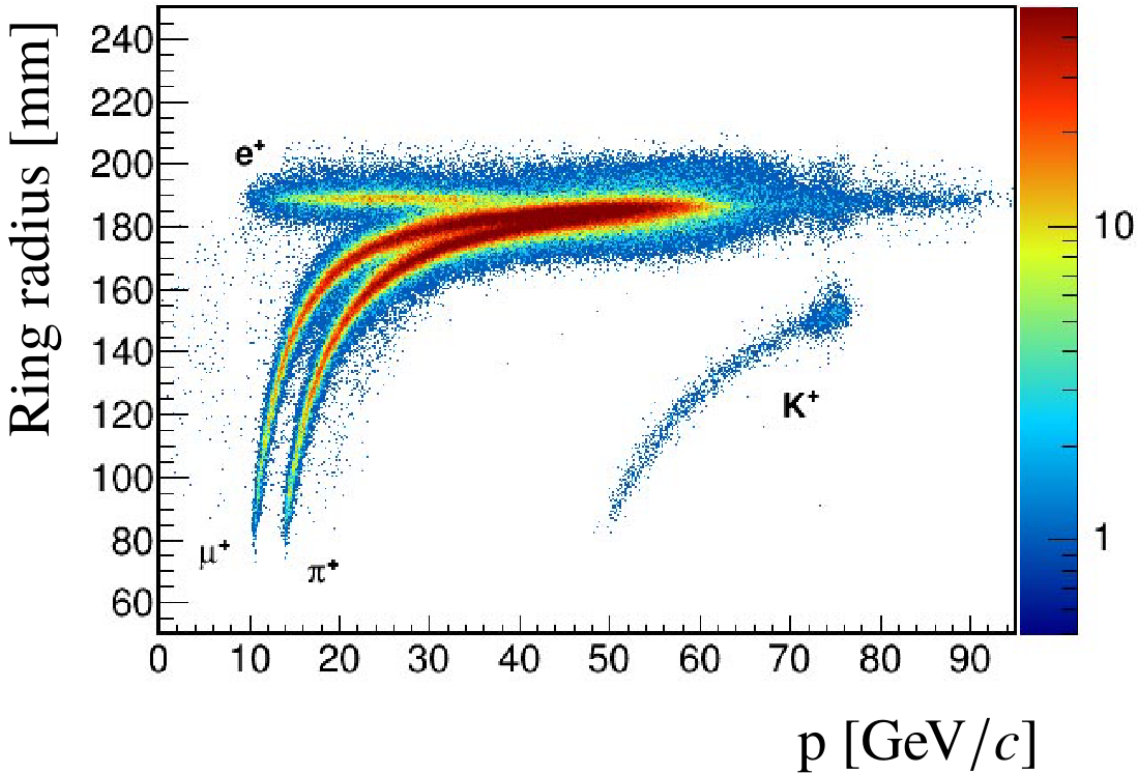

Figure 2.8: Cherenkov ring radius in the RICH detector versus the momentum of the particle. The regions occupied by e^+, μ^+, π^+, and scattered beam kaons are shown. Particles occuping the momentum range >75 GeV/c are due to halo muons [51].

2.2.7 The photon veto system

One of the main backgrounds in the $K^+ \to \pi^+\nu\bar{\nu}$ analysis is the $K^+ \to \pi^+\pi^0$ decay with a branching ratio of $\mathcal{B}(K^+ \to \pi^+\pi^0) = (20.67 \pm 0.08)\%$ and a 99% probability that the neutral pion decays to two photons. To achieve a background supression at the level of $\mathcal{O}(10^{12})$, the kinematic cuts can provide a rejection factor of $\sim 10^4$, leaving a rejection factor of 10^8 to be achieved by the photon-veto systems. Four calorimeters are used to identify decays with photons in the final state, each discussed below. The majority of the rejection power is achieved with the liquid krypton calorimeter (LKr) covering an angular range of 1–8.5 mrad. The large angle veto (LAV) detects low energy photons emitted with an angle larger than that covered by the LKr, 8.5–50 mrad, whilst the intermediate-ring calorimeter (IRC) and small-angle calorimeter (SAC) detect high energy photons that would otherwise escape down the beam pipe.

The large angle veto

The Large-angle veto (LAV) [68] is formed of twelve ring-shaped stations, eleven of which are interspersed in the vacuum tank whilst the final station is situated in air approximately 3 m upstream of the LKr. Each station is formed of radially aligned lead glass blocks previously used in the OPAL experiments electromagnetic calorimeter [69]. Incident photons to these lead glass blocks produce electromagnetic showers and as a result emit Cherenkov photons. These photons are detected by PMTs; one PMT is used per lead glass block with a total of 896 across all the twelve stations.

With the restriction on the π^+ momentum in the $K^+ \to \pi^+\nu\bar{\nu}$ analysis, it is not possible for both of the photons from a $K^+ \to \pi^+\pi^0$, $\pi^0 \to \gamma\gamma$ to have angles larger than that covered by the LAV. It is however possible for one of these photons to be

outside this angular range but this only occurs in ∼0.2% of events with the energy of the escaping photon being less than 200 MeV [51]. To meet the overall photon rejection, the LAV is required to have an inefficiency less than 10^{-4} for photons with energies larger than 200 MeV. The time resolution on the LAV is ∼1 ns for a photon with 1 GeV of energy and an energy resolution better than 10% is required such that a precise veto energy threshold can be applied.

The small angle veto

The small-angle veto (SAV) is formed by the intermediate-ring calorimeter (IRC) and the small-angle calorimeter (SAC), both of which are shashlyk calorimeters [70] with alternating layers of lead absorbers and active scintillator plates. These detectors are designed to measure photons which have energies greater than 5 GeV and would otherwise traverse down the beam pipe undetected. Photon rates of the order of 1 MHz are expected at nominal beam intensity in both detectors however the IRC is also exposed to muons from the decays of beam particles and thus the rate is increased to ∼10 MHz. The time resolution for the SAV is less than 1 ns [51].

The liquid krypton calorimeter

NA62 reuses the liquid krypton calorimeter (LKr), depicted in Figure 2.9, from its predecessor experiment NA48; a detailed description of which can be found in [71]. However, some upgrades were required for the NA62 experiment. Firstly, the readout was upgraded to handle the increased rate [72] and secondly, some of the external components on the cryogenic system needed to be changed such that the detector could sustain another decade of data taking.

The LKr is a quasi-homogeneous calorimeter filled with ∼9000 litres of liquid krypton at 120 K. The LKr cryogenic container extends from the beam pipe at a

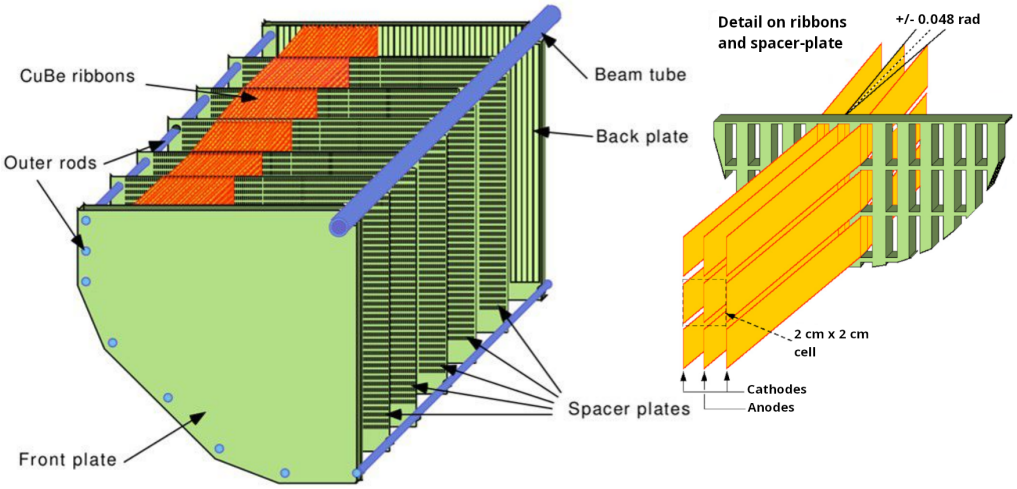

Figure 2.9: Left: Schematic of one quadrant of the LKr calorimeter structure. Right: Detailed diagram of the calorimeter cells. Plot recreated from [51].

radius of 8 cm, to an outer radius of 128 cm with a depth of 127 cm; this volume corresponds to an active material length of $27X_0$. Electrically charged particles and photons passing through the LKr result in electromagnetic showers in which their energy can be measured. The volume is divided into 13248 $2 \times 2\,\text{cm}^2$ cells by Cu-Be electrodes with a zig zag shape to avoid inefficiencies if a particle shower is too close to an anode.

The energy resolution, σ_E, spatial resolution, $\sigma_{x,y}$, and temporal resolution, σ_t, are given by the following equations [51]:

$$\frac{\sigma_E}{E} = \frac{4.8\%}{\sqrt{E}} \oplus \frac{11\%}{E} \oplus 0.9\%, \tag{2.2}$$

$$\sigma_{x,y} = \frac{0.42}{\sqrt{E}} \oplus 0.06, \tag{2.3}$$

$$\sigma_t = \frac{2.5}{\sqrt{E}}. \tag{2.4}$$

Here, the energy is measured in GeV, spatial coordinates in cm and time in ns. The LKr has an inefficiency of 10^{-5} for photons with energies above 5 GeV whilst this increases to 10^{-4} for photon energies between 1 and 5 GeV.

2.2.8 The charged particle hodoscopes

Charged particle hodoscopes cover an area downstream of the RICH, upstream of the LKr, between the IRC outer radius, 145 mm, and the LAV12 inner radius, 1070 mm. The CHODs provide an input for the L0 trigger, and in particular combine with the RICH to form the minimum bias trigger. The hit rate on these detectors is dominated by beam kaon decays but also contributing are beam pion decays and the muon halo.

The NA48-CHOD has been repurposed from the NA48 experiment [71] and is placed upstream of the LAV12 detector. Plastic scintillators of 20 mm thickness are placed into two consecutive planes of 64 vertical and 64 horizontal slabs, see Figure 2.10. Independent time measurements from each plane are combined together with an overall time resolution $\mathcal{O}(0.2\,\text{ns})$.

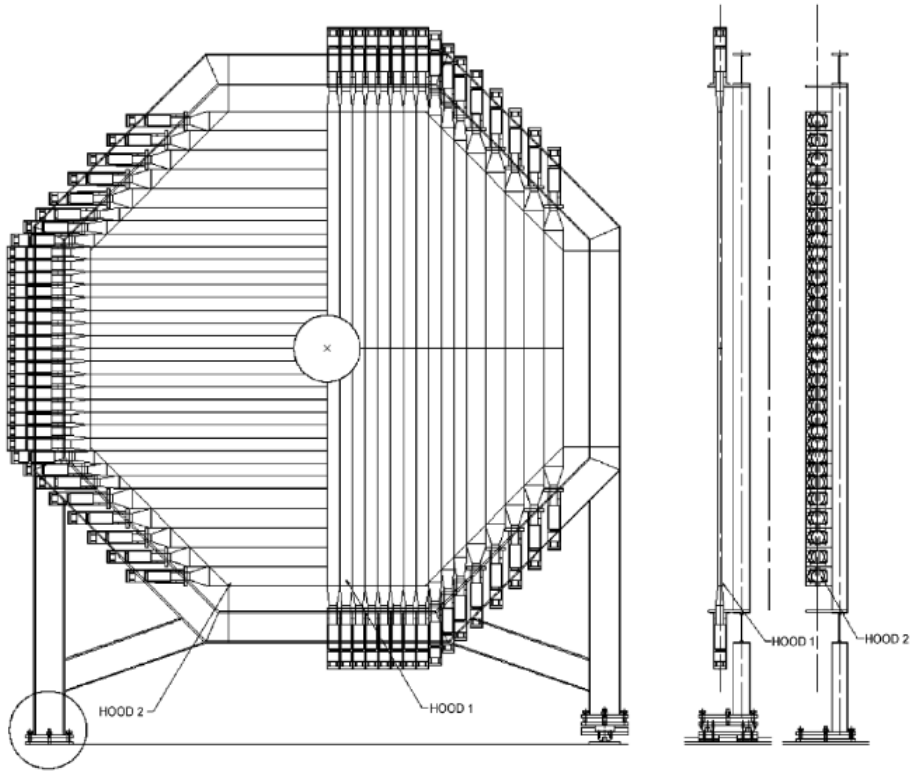

Figure 2.10: Schematic drawing of the NA48-CHOD detector. Only half sections of the horizontal and vertical planes are shown [71].

Conversely, the CHOD is formed of 152 smaller plastic scintillator tiles of 30 mm thickness. Tiles are 108 mm high and either 134 mm or 268 mm wide and placed alternating either side of a central support with a 1 mm overlap, see Figure 2.11. The tile sizes are chosen to optimise the particle flux and those closest to the beam pipe are smallest. A time resolution $\mathcal{O}(1\,\text{ns})$ is achieved.

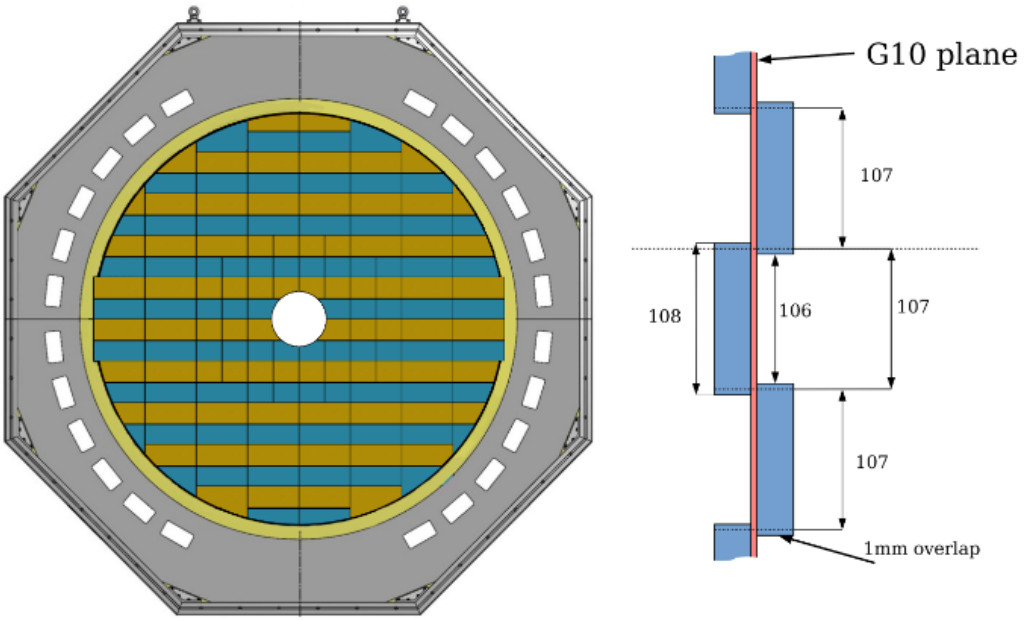

Figure 2.11: Schematic drawing of the CHOD detector [73].

2.2.9 The muon veto detectors

To aid in the discrimination of pions and muons, the hadronic calorimeters MUV1 and MUV2, followed by an 80 cm iron wall and the MUV3 form the muon veto system. Additionally there is a peripheral muon veto system, MUV0, upstream of the CHOD to detect low momentum π^- from $K^+ \to \pi^+\pi^-\pi^+$ decays escaping the RICH acceptance.

The MUV1 and MUV2 detectors are formed from alternating layers of iron and scintillator. MUV2 was inherited from the NA48 experiment whilst the MUV1 was built especially for NA62 with a fine transversal segmentation to better separate the

hadronic and electromagnetic shower components [51].

The MUV3 is located downstream of an 80 cm filtering iron wall and is responsible for the detection of muons that surpass the wall. The MUV3 is made of 148 tiles of size $220 \times 220\,\mathrm{mm}^2$, except for the eight closest to the beam pipe which are smaller due to a higher particle rate, see Figure 2.12.

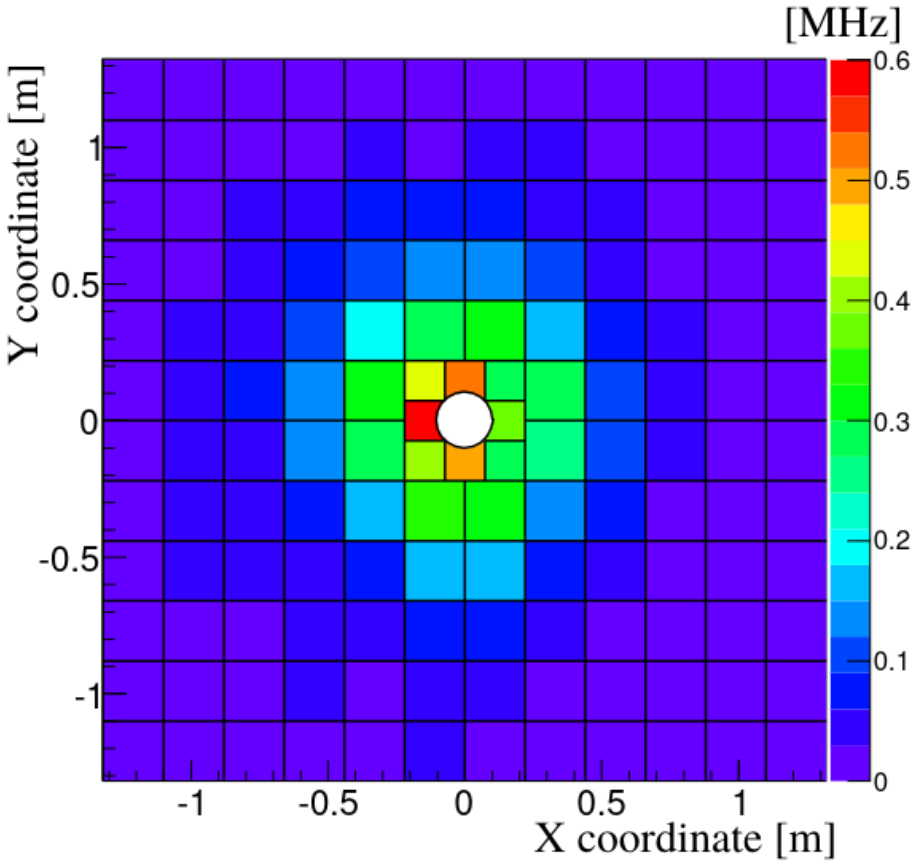

Figure 2.12: Tile geometry of the MUV3 detector along with the expected hit rates in each tile for the nominal beam rate. The 'hot' tile on the negative x side of the beam pipe has a hit rate of 3.2 MHz (off the colour scale) and this is dominated by muons from pions decaying in the beam [51].

2.2.10 The hadronic sampling calorimeter

Whilst the MUV0 detects low momentum pions escaping the RICH acceptance, the HASC detects high momentum pions ($> 50\,\mathrm{GeV}/c$) that travel through the central apertures in the STRAW chambers. To sweep these pions away from the

beam, a dipole magnet is placed upstream of the HASC. The detector itself is a hadronic sampling calorimeter formed of 9 identical modules located downstream of MUV3, covering an acceptance of $-0.48\,\mathrm{m} < x < -0.18\,\mathrm{m}$ and $|y| < 0.15\,\mathrm{m}$. For NA62 run-2, an additional HASC station, placed on the opposite side to the original ($0.18\,\mathrm{m} < x < 0.48\,\mathrm{m}$), was added such that the detector is now symmetric.

2.3 Trigger and data acquisition

In the NA62 experiment, the $K^+ \to \pi^+\nu\bar{\nu}$ branching ratio measurement foresees the collection of $\mathcal{O}(10^{13})$ kaon decays thus a trigger is critical to limit the amount of useful data stored and later analysed. The NA62 trigger system is formed of two stages; the first, L0, is a hardware trigger followed by a software trigger, L1. In some papers, the L1 trigger may also be referred to as the high level trigger (HLT). Each stage of the trigger is designed to reduce the particle rate by about a factor of 10 such that the $\mathcal{O}(10\,\mathrm{MHz})$ rate from the detectors is reduced to $\mathcal{O}(1\,\mathrm{MHz})$ by the L0 trigger, and $\mathcal{O}(100\,\mathrm{kHz})$ written to permanent storage; an event is $\mathcal{O}(1\,\mathrm{MB})$ in size. Trigger primitives, packets of information, from certain detectors are processed by the L0 trigger processor (L0TP), see Table 2.3, whilst information from the remaining detectors is collected if the event meets certain requirements at the L0 stage. The L0TP combines trigger primitives within a time window of 6.25 ns from a specified reference detector, usually the RICH. A detailed description of the L0 trigger system is given in [74].

Table 2.4 shows the trigger lines for data collected in 2018. These have been designed to target specific categories of events and form a sequence of L0 and L1 trigger conditions. If an event meets the criteria for a trigger line at the L0 stage, all of the detector information is collected and sent to an online PC farm in which the L1 trigger algorithms are executed. Three L1 algorithms are available and can

be configured towards the aim of a trigger mask:

- The KTAG algorithm requires an in time kaon with the L0 trigger. A signal in at least 5 sectors is required within 5 ns of the trigger time.
- The LAV algorithm identifies in time activity in the LAV detector. At least three signals in stations 2-11 are required within 6 ns of the trigger reference time.
- The STRAW algorithm reconstructs the tracks of charged particles and calculates their momentum.
  - The main STRAW algorithm is optimised for the $K^+ \to \pi^+\nu\bar{\nu}$ decay. This requires a single track event, with some loose criteria for a 'good' track, originating in the fiducial volume prior to STRAW1.
  - The STRAW-1TRK is similar to the above algorithm although is a less restrictive version, only requiring the single track to have a momentum less than 65 GeV/c.
  - The STRAW-Exo covers multi-track final states, requiring at least one track with negative charge.
  - The STRAW-MT identifies events with at least three tracks originating inside the fiducial volume.
  - The STRAW-DV identifies pairs of tracks forming a displaced vertex at least 100 mm from the nominal beam axis.

Only if all L0 trigger conditions are met, and the L1 algorithms passed for at least one trigger mask the event is stored. In addition to passing all conditions, a downscaling factor can also be applied to reduce certain event categories.[2] The PNN trigger line

[2] A downscaling factor of N indicates that only one in N events are stored.

has a downscaling factor of 1 to maximise the amount of $K^+ \to \pi^+\nu\bar{\nu}$ events stored on disk whilst the control (minimum bias) trigger has a downscaling of 400.

Further information on the NA62 trigger system, including performances, can be found in [75]. Additionally, the performance of the trigger for the $K^+ \to \pi^+\nu\bar{\nu}$ measurement, comparing NA62 run-1 and NA62 run-2 conditions, is described in section 5.3.

Table 2.3: L0 trigger conditions for the kaon operating mode [75].

Detector	Condition	Description
RICH	RICH	At least two signals in the detector
CHOD	Q1	At least one signal in any quadrant
	Q2	At least one signal in each of two different quadrants
	QX	At least one signal in each of two diagonally-opposite quadrants
	UTMC	Upper multiplicity condition: < 5 signals in the detector
NA48-CHOD	NA48-CHOD	At least one signal in any quadrant
MUV3	M1	At least one signal in the detector
	MO1	At least one signal in the outer tiles
	MO2	At least two signals in the outer tiles
	MOQX	At least one signal in each of two diagonally-opposite quadrants
LKr	E10	At least 10 GeV deposited in the LKr
	E20	At least 20 GeV deposited in the LKr
	E30	At least 30 GeV deposited in the LKr
	C2E5	At least 5 GeV deposited in the LKr by at least two clusters
	LKr30	Logical OR between E30 and C2E5

Table 2.4: Trigger lines for kaon decays and their corresponding L0 and L1 trigger conditions. An overline indicates that a condition is used as a veto, for example $\overline{\text{QX}}$ is the requirement that there are no hits in opposite quadrants of the CHOD. MT is a multi-track line whilst DV is a displaced vertex, additionally e and μ require the presence of an electron or muon respectively.

Trigger Line	L0 Trigger Conditions	L1 Trigger Conditions
PNN	RICH · Q1 · UTMC ·$\overline{\text{QX}}$ · $\overline{\text{M1}}$ · $\overline{\text{LKr30}}$	KTAG ·$\overline{\text{LAV}}$· STRAW
Non-μ	RICH · Q1 ·$\overline{\text{M1}}$	KTAG · STRAW-1TRK
MT	RICH · QX	KTAG · STRAW-Exo
2μMT	RICH · QX · MO2	KTAG · STRAW-Exo
eMT	RICH · QX · E20	KTAG · STRAW-Exo
μMT	RICH · QX · MO1 · E10	KTAG ·$\overline{\text{LAV}}$· STRAW-MT
DV-μ	RICH · Q2 · MO1 · E10	$\overline{\text{KTAG}}$· STRAW-DV
DV-2μ	RICH · Q2 · MO2 ·$\overline{\text{E10}}$	STRAW-DV
Neutrino	RICH · Q1 · MOQX ·$\overline{\text{Q2}}$	KTAG ·$\overline{\text{LAV}}$· STRAW-1TRK
Control	NA48-CHOD	None

2.4 The NA62 software framework

The NA62 collaboration maintains a framework of software tools (NA62fw) for detector simulation, physics sensitivity studies and data analysis. There are three main components as seen in Figure 2.13: NA62MC, for the simulation of the detector and events, NA62Reconstruction, for combining raw data into candidate signals, and NA62Analysis, software tools for the analysis of data whether collected or simulated. All software components are constantly updated and improved.

NA62MC is a GEANT4 [76] based collection of tools used to simulate the interactions of particles with detectors. Each detector within NA62 is precisely simulated to be geometrically accurate as well as composed of the correct material. Particle interactions with each of the materials are fully simulated within Geant4. The NA62 beamline and beam is simulated using TURTLE [77] with particles allowed to decay according to NA62 defined generators. These generators handle the decay kinematics such as to include the appropriate matrix elements and transition form factors. An event is defined as the decay of a single beam particle.

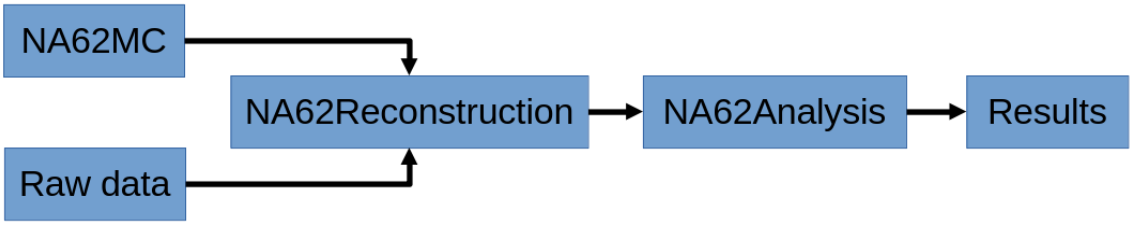

Figure 2.13: Block diagram showing the flow of data through the NA62 software tools.

To convert NA62MC or raw data into useful signals, NA62Reconstruction is used. NA62Reconstruction is based on ROOT [78]. Here each detector constructs 'candidates' from their hits depending on specific detector conditions, usually their space and time distributions. In addition to the single events generated by NA62MC, it is neccessary to reconstruct a simulated event as if other events were occurring very close in time; this is also handled by NA62Reconstruction. Simulated events are overlaid on top of each other depending on an intensity template derived from data. Further details on the work carried out in this thesis for the software generating the intensity templates is given in chapter 4.

NA62Analysis provides a collection of software tools for common tasks performed whilst analysing data. These include things such as data callibration, corrections of time, energy and momentum measurements (depending on data taking conditions), but also the association of candidates from different detectors.

Chapter 3

A CEDAR detector with hydrogen gas

The measurement of the branching fraction of the $K^+ \to \pi^+ \nu\bar{\nu}$ decay depends on the identification and removal of background originating from the dominant kaon decays, along with various upstream sources that result from interactions of the beam particles with material in the beam line and sub-detectors. Although no evidence of any background arising from the nitrogen gas in Cedar-W has been found from the analysis of data thus far, it is possible that some background may emerge in the future as experimental sensitivity increases. Therefore, it is logical to investigate whether CEDAR can be redesigned to use hydrogen as the Cherenkov radiator, resulting in a significant reduction in the multiple scattering of beam particles in the gas. This chapter reports this investigation.

3.1 Working principles of a Cherenkov detector

As it is not feasible to separate in-flight kaons from the other major beam components (i.e., π^+, p) in the small beam line distance of NA62, kaons are tagged using CEDAR, a Cherenkov differential counter. This exploits the fixed momentum beam, resulting in light from each type of particle being emitted at a different angle, which can then be focused into rings of different radii.

There are two base types of CEDAR, known as Cedar-N and Cedar-W, with a historical reference to the North and West experimental areas at CERN where they were first used. They are optimised to cover different momentum ranges. The former can distinguish kaons from pions up to 300 GeV/c using helium gas as the radiator whilst the latter uses nitrogen gas and can separate kaons from pions up to momentum values of 150 GeV/c [59]. NA62 utilised a Cedar-W detector up until 2022 due to its lower momentum beam.

The angle, θ_c at which Cherenkov radiation is emitted at is given by:

$$\cos\theta_c = \frac{1}{n\beta}, \tag{3.1}$$

where β is the velocity of the particle in natural units passing through a medium with refractive index n. Given a beam of fixed momentum, p, a particles velocity is dictated by its mass, m,

$$\beta = \left(1 + \frac{m^2}{p^2}\right)^{-\frac{1}{2}}. \tag{3.2}$$

Therefore, combining this with Equation 3.1, Cherenkov radiation occurs at a fixed angle for each of the major beam components in NA62. As a result, a system of lenses and mirrors can be used to focus the light emitted at a given angle, i.e from kaons, into a narrow, distinguishable ring. The narrow ring formed from kaons is then directed through a small, adjustable aperture and measured by PMTs, the

details of which shall be described in subsections 3.1.1 and 3.1.2.

In addition to the rings being distinguishable, the photons must be detected. The number of photons, N, per unit length, x, per unit wavelength, λ, of the Cherenkov radiation is given by the Frank-Tamm formula [79]:

$$\frac{d^2N}{dxd\lambda} = \frac{2\pi\alpha}{\lambda^2}\sin^2\theta_c = \frac{2\pi\alpha}{\lambda^2}\left(1 - \frac{1}{n^2\beta^2}\right), \tag{3.3}$$

with the fine structure constant α. Moreover, when operating with a gaseous medium such as that at NA62, it is important to understand how the density and pressure of the gas affect the refractive index. For a gas of constant chemical composition,

$$\text{density} \propto (n-1), \tag{3.4}$$

and assuming an ideal gas at a fixed temperature,

$$\text{pressure} \propto (n-1). \tag{3.5}$$

If the radiator gas in the CEDAR is changed from nitrogen to hydrogen, due to the different gas densities, the pressure of the gas must also be changed such that the Cherenkov angle remains the same. Additionally, the dispersive behaviour of the gases differs as a function of wavelength. Therefore, even if the pressure of hydrogen is tuned to match the refractive index of nitrogen for a given wavelength, new CEDAR internal optics must be devised to ensure performance across the photon wavelength spectrum. Combining Equations 3.1, 3.3 and 3.5 show that for an increase in pressure, the angle at which photons are emitted and the number of them also increase.

3.1.1 CEDAR

To create a system capable of distinguishing between different particles in an unseparated beam, the Cherenkov light must first be transformed into discrete rings. One approach is to use a spherical mirror positioned at the downstream end of the CEDAR vessel, which reflects light back towards a diaphragm placed in the mirror's focal plane. In this scenario, the light is focused at the diaphragm at a radius, $R_{\text{diaphragm}}$:

$$R_{\text{diaphragm}} = f\theta_c = \frac{r_m\theta_c}{2}, \tag{3.6}$$

where $f = r_m/2$, is the focal length [80], r_m is the radius of curvature of the mirror and θ_c is the Cherenkov angle defined in Equation 3.1. The ring formed upon the diaphragm plane is broad, primarily due to the spherical aberration introduced by the curved mirror and chromatic aberration of the gas.

To address this issue, a Mangin Mirror, which is a negative-meniscus lens with a reflective back surface, is used instead of the spherical mirror. With carefully chosen parameters, the spherical aberration introduced by the mirror can be cancelled out [81]. However, the use of the lens also introduces an additional contribution to the chromatic aberration. The focal length of such a mirror, f_m, with refractive index, n, is given by:

$$\frac{1}{f_m} = \frac{2n}{r_2} - \frac{2(n-1)}{r_1}, \tag{3.7}$$

with radii of the refracting surface, r_1, and reflecting surface, r_2[3]. For the Cedar-W system, this results in a focal length of 5.031 m, with $r_1 = 6.615$ m and $r_2 = 8.613$ m, or the distance between the mirror and the diaphragm plane.

To reduce the effect of chromatic aberration and minimise the width of the light ring formed on the diaphragm, a second lens is introduced upstream of the Mangin Mirror known as the Chromatic Corrector, see Figure 3.1. The Chromatic

[3]Both radii are positive such that the focal length is greater than 0.

Corrector is a plano-convex lens with opposite sign dispersion to the Mangin Mirror, which allows for the chromatic dispersion to be minimised. The focal length of the Chromatic Corrector is given by:

$$\frac{1}{f_c} = \frac{n-1}{r_c}, \tag{3.8}$$

where r_c is the radius of curvature of the convex surface. For the Cedar-W system, $r_c = 1.385\,\text{m}$, so $f_c = 2.904\,\text{m}$. The resulting combination of the Mangin Mirror and Chromatic Corrector has a total focal length given by:

$$\frac{1}{f_{tot}} = \frac{1}{f_c} + \frac{1}{f_m} - \frac{d}{f_c f_m} \tag{3.9}$$

with a distance, d, between the lenses. This allows for the formation of narrow rings on the diaphragm plane.

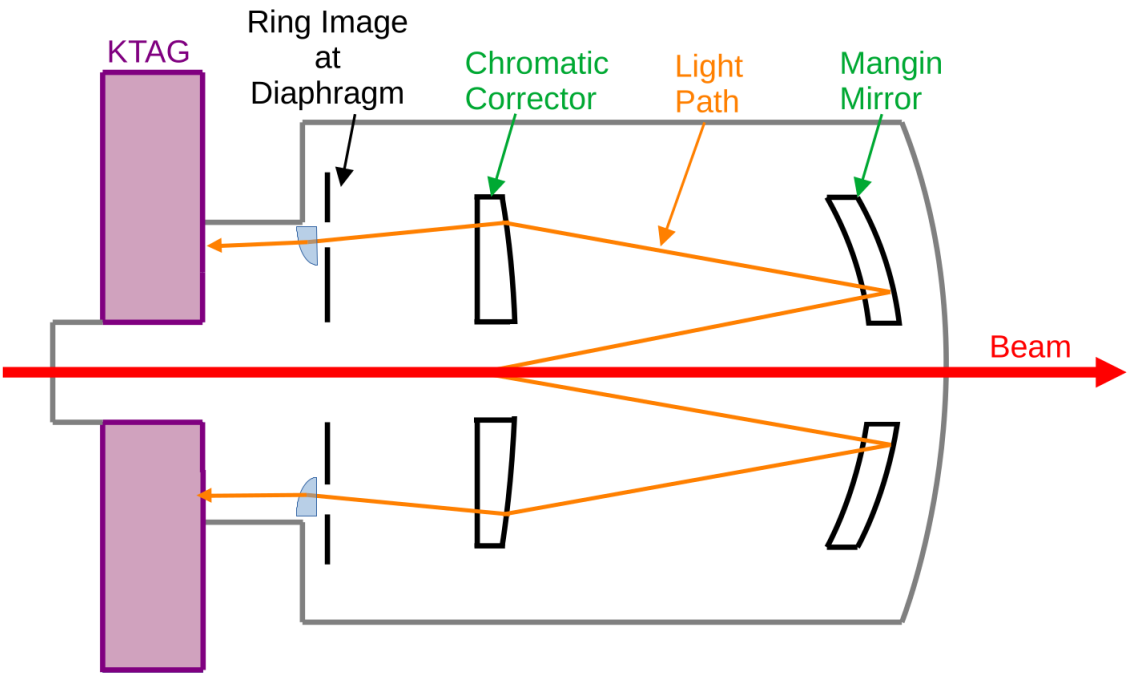

Figure 3.1: Schematic of a standard CEDAR showing the typical path taken by photons. In addition to the standard CEDAR, ending with a ring image formed at the diaphragm plane, the photon detection system, KTAG, has been added by NA62 to improve the detection of photons passing through the diaphragm aperture.

Figure 3.1 depicts an example photon travelling through the CEDAR system. After passing through the Mangin Mirror and Chromatic Corrector, light emitted from kaons passes through an adjustable diaphragm aperture at a radius of 100 mm. To optimize the collection of light from kaons while minimizing light emitted from pions and protons, an aperture width of 2 mm is chosen to effectively accomplish these objectives [82]. After passing through the diaphragm, the light is focused by a set of eight condenser lenses before passing through the quartz windows and entering the KTAG, as described in subsection 3.1.2.

To achieve the best discrimination between particles, it is useful to have a narrow ring focused on the diaphragm aperture. Factors that hinder this and contribute to the broadening of the light ring are as follows [58]:

- Beam angle divergence - one of the more dominant factors, this has been limited to an RMS angle of $\sim 70\,\mu$rad in each plane corresponding to a broadening of the lightspot by 0.2 mm.
- Multiple scattering of the beam - having more material for the beam to pass through increases the chance of multiple scattering occurring. For the Cedar-W filled with nitrogen, the broadening of the lightspot is 0.09 mm. This limitation provides motivation to investigate using hydrogen as the radiator gas, discussed further in subsection 3.1.3.
- Inhomogeneity of the refractive index caused by temperature gradients in the radiator gas - this is minimised by the use of thermal insulation and running the experiment at a stable temperature. For a temperature variation of 1 K the broadening of the lightspot is 0.05 mm.
- Optical aberrations - these have been limited to 6 µm so can be seen as negligible

- Chromatic dispersion - due to the wavelength dependence of the refractive index, photons of differing wavelengths are focused at different radii. This is largely corrected for by the Chromatic Corrector.

3.1.2 KTAG

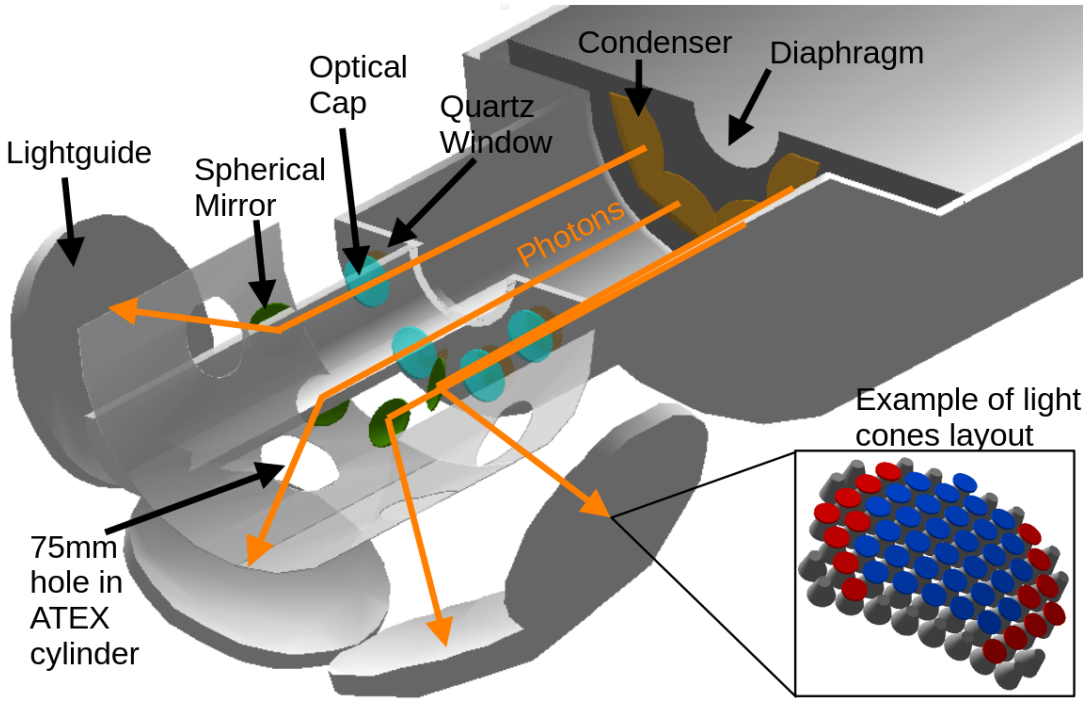

Figure 3.2: Geant4 visualisation of the KTAG optics. Here light travels from right to left through the condensers, quartz windows and optical caps before being reflected radially outwards by the spherical mirrors towards the lightguides.

Although the original CEDAR was designed to be used with 8 PMTs attached to the 8 Quartz Windows, the high intensity beam of NA62 necessitated an upgrade. The criteria for this upgrade were to achieve a kaon tagging efficiency[4] greater than 95%, a pion mis-tag rate of less than 10^{-4}, and a time resolution of 100 ps, as outlined in [58]. Therefore, the PMTs were replaced with a system referred to as the KTAG, shown in Figure 3.2. Only the lower half of the KTAG is shown, along with an example of the light cones in one of the octants.

[4]The kaon tagging efficiency is defined as the number of kaon events with light occupying at least 5 sectors of the KTAG normalised to the total number of kaon events.

Photons leaving the Quartz Window, and hence the CEDAR, pass through an 'optical cap'. This is a plano-convex lens that focuses the light towards a spherical mirror, reflecting it radially outwards towards the lightguides. The use of the spherical mirrors is two-fold: to distribute the light onto larger areas (lightguides) reducing the photon rate on the PMTs, and the PMTs are subjected to less radiation damage from the beam. Each lightguide is equipped with an array of 48 single anode PMTs, as shown in Figure 3.3. There are two types of PMTs installed: the R9880U-110 (blue) in the centre and the R7400U-03 (red) on the outside, details of the PMT technology can be found in [82–84]. The PMTs in the centre have a higher quantum efficiency than those on the outside, see Figure 3.4. The circles shown in white are not yet instrumented but could be in the future if a CEDAR design would benefit from this addition.

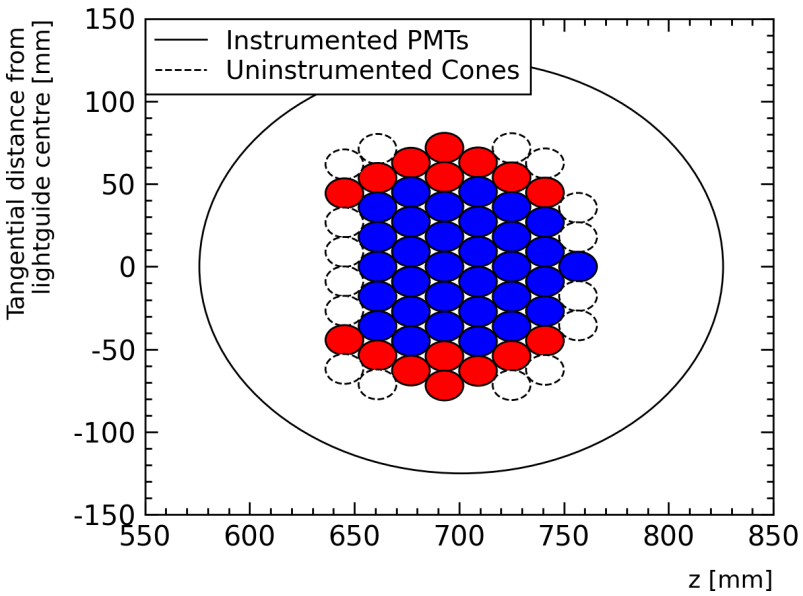

Figure 3.3: Diagram showing the arrangement of PMTs in the lightguide. Here we see the higher quantum efficiency (QE) PMTs (shown in blue), lower QE PMTs (shown in red), and uninstrumented cones (dashed outlines) in which a PMT could be placed in the future.

Another advantage of the lightguides is that the PMTs are able to perform single photon detection with a time resolution of 300 ps. An average of $\sim$ 18 photons detected per kaon in the beam for the NA62 Cedar-W, allows for an overall time

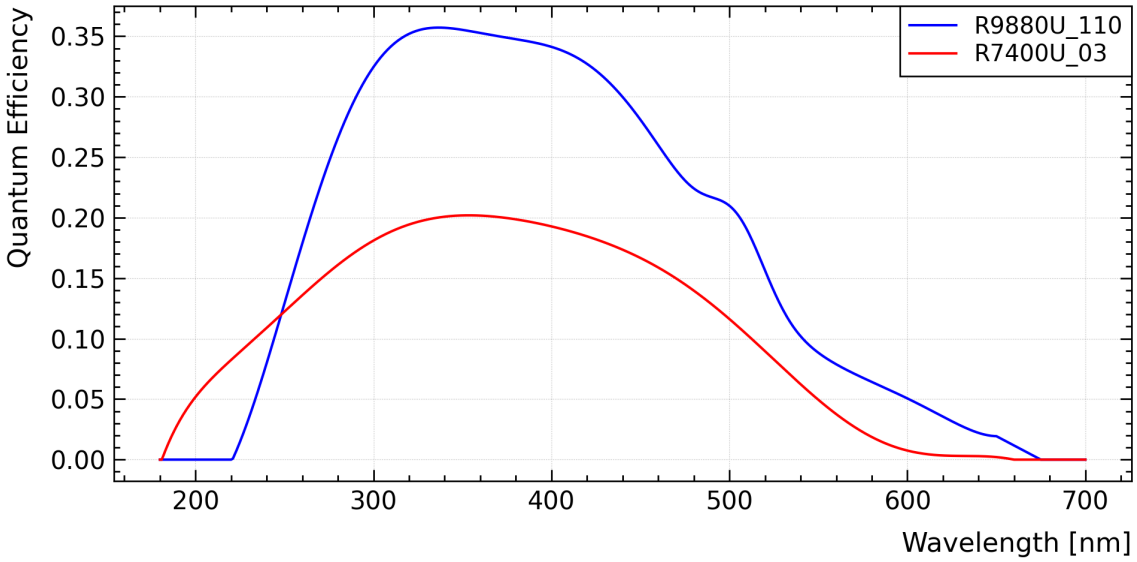

Figure 3.4: Quantum efficiency for the PMTs used in the KTAG as a function of wavelength [85, 86].

resolution of $300\,\text{ps}/\sqrt{18} = 70\,\text{ps}$ [51]. Additionally, requiring that photons be detected in at least five octants to tag a kaon produces a kaon identification efficiency of $\sim 99\%$ whilst keeping the pion mis-identification rate at the level of 10^{-4}.

3.1.3 Why use hydrogen?

The decision to switch to hydrogen as the Cherenkov radiator is motivated by the goal of reducing the material in the beamline consequently reducing the interactions of beam, and resulting in less background originating upstream of the decay region. To achieve the same Cherenkov angle as for nitrogen, the hydrogen pressure would be 3.65 bar compared with 1.71 bar for nitrogen. In this case, the amount of material presented to the beam would be reduced from $3.7\%X_0$ to $0.7\%X_0$ [58]. This does come with one caveat, as the CEDAR was designed for use with nitrogen (which has different dispersive behaviour from hydrogen), the internal optics do not create narrow, distinguishable rings when using hydrogen. As can be seen from Figure 3.5, the wavelength dependence of the radial position of Cherenkov photons reaching the diaphragm of Cedar-W for hydrogen and nitrogen are very different,

with considerable overlap in radial position for photons from kaons and pions in the case of hydrogen. In order to prevent Cherenkov photons from pions passing through the diaphragm, a significant fraction of the photons from kaons would be lost and this would seriously compromise the performance of KTAG. Hence a new optical design, referred to in what follows as Cedar-H, is required. As we wish to exclusively contain the kaon light ring inside the diaphragm aperture, it is logical to compare for each design not only the number of photons detected at the PMTs but also the width of the light ring.

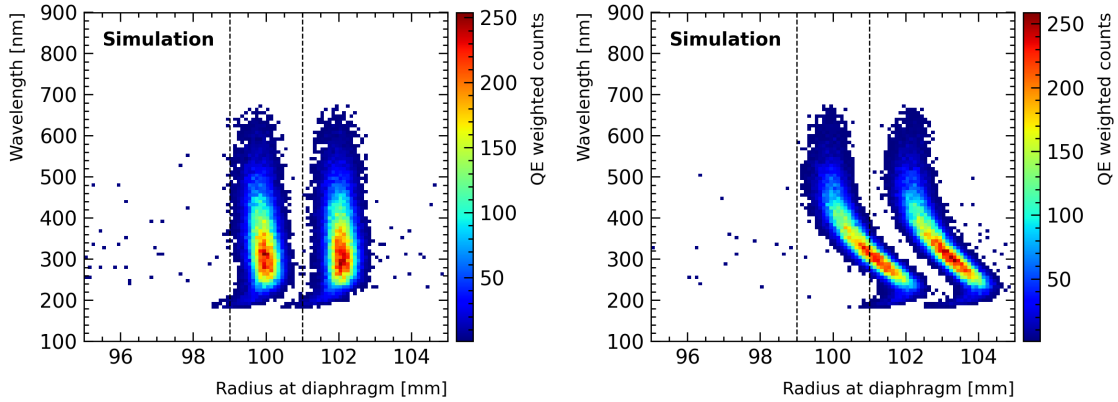

(a) Nitrogen gas at 1.71 bar pressure (b) Hydrogen gas at 3.65 bar pressure

Figure 3.5: Photon radius at the diaphragm versus their wavelength for nitrogen (left) and hydrogen (right) using a standard Cedar-W. In each figure, the kaon light distribution is that on the left and pions on the right. The diaphragm aperture is shown by the dashed lines. 1000 kaons and 1000 pions are simulated.

3.2 Previous work

Prior to my contributions, a design for a new Cedar-H had been discussed, see Chapter 3 in [87], and an overview relevant to the parameters of my work shall be described below. Firstly, due to the NA62 detector using a Cedar-W with nitrogen gas, this base CEDAR type was initially investigated as to whether this could be adapted for use with hydrogen. However, once it was confirmed that a spare Cedar-N type became available at CERN, and that work could be done to it, the task became

optimising the Cedar-N instead for use with hydrogen.

Due to the higher cost of the mechanical supports for the lenses compared to the lenses themselves, optimisation was performed under certain constraints. To keep the supports unchanged, the lenses were kept in the same position along the optical axis, and their diameters constant. The radii of curvature of the Mangin Mirror and the radius of curvature of the Chromatic Corrector were then altered to find the optimal optical design under these constraints. A new design was found with the addition of adapting the KTAG optics so that the light could be maximised at the PMTs. This entailed changing from Cedar-N condensers to Cedar-W condensers so light was focused on the centre of each Quartz Window, and moving the spherical mirror inside the KTAG radially inwards by 2 mm. This provided an acceptable light spot on the PMTs with performances equivalent to the NA62 Cedar-W with respect to light yield, kaon tagging, and pion misidentification.

The remainder of this Chapter discusses work carried out by the author in further optimising Cedar-H with the aim of not only matching the Cedar-W performance, but additionally increasing the light yield.

3.3 Redesign of CEDAR/KTAG

The redesign of Cedar-H falls naturally into two parts: first the number of Cherenkov photons (weighted by the quantum efficiency of the PMTs) passing through the narrow CEDAR diaphragm aperture must be maximised; secondly, this Cherenkov light must be redistributed by the optics external to Cedar-H into a pattern that fully illuminates the PMT arrays. The aim is to find a design that produces more photoelectrons per kaon than is achieved with the nitrogen radiator, and for safety reasons the working pressure with hydrogen in Cedar-H should be as

low as can be reasonably achieved. A discussion of the NA62 Cedar-W performances can be found in [60].

The new Cedar-H design is based on an existing Cedar-N, which has an identical body and mechanical layout to a Cedar-W. This means, for example, that either of the two rather complex condenser lenses can be used for Cedar-H, the choice of which helps in simplifying the optics external to the CEDAR. The mechanical frame, rigidly fixed on the inside of the CEDAR body, that hold and align the Mangin Mirror and Corrector Lens, Figure 3.6, are both complex and sophisticated and it was agreed with CERN engineers that no changes would be made to them. This means that the positions and maximum radii of the Mangin Mirror and Corrector Lens are fixed. The parameters to be modified were the two radii of the Mangin Mirror, and the radius of the convex surface of the plano-convex Corrector Lens.

Figure 3.6: Image of an opened CEDAR, photograph taken by Serge Mathot (CERN). The mechanical frame holding the diaphragm, Mangin Mirror and Chromatic Corrector on the optical axis is visible.

The work outlined in this chapter from this point forwards was completed in collaboration with Dr Fry [88]. His independent simulation of the CEDAR vessel aided in finding and verifying the new designs. Small modifications to his designs

were required to correct from his toy MC to the full Geant4 simulation, i.e accounting for aberration, simulated using the NA62 software, NA62MC. All designs presented in this thesis have been directly measured in simulations by the author. Additionally, the required modifications to the KTAG simulation were performed solely by the author.

3.3.1 Design methodology for Cedar-H

To simplify the optimisation, we consider the CEDAR (up to the diaphragm) and KTAG (diaphragm to the PMTs) as separate optimisations. The optical design of the CEDAR aims to achieve as good a focus as possible of Cherenkov light at the diaphragm aperture by minimising the defocussing contributions from geometrical aberrations and chromatic dispersion in the quartz and hydrogen media. The balance between geometrical aberrations and chromatic dispersion changes with gas pressure, and this results in solutions for the optimal radii of curvature of the three surfaces that are specific to the particular gas pressure.[5] To quantify the optimum solution, we consider the Gaussian width of the light ring; a smaller width here promoting the collection of all kaon light whilst minimising light from pions. As a guideline, a Gaussian width of 0.5 mm was chosen as the boundary condition for a satisfactory CEDAR design under the assumption that the diaphragm aperture will remain at 2 mm.

To solve this four-dimensional problem (3 radii of curvature and pressure), an iterative approach was undertaken starting from the design outlined in [87]. By changing the radius of curvature for one of the surfaces, the width of the light rings at the diaphragm would change. The radius at which the narrowest ring was formed was selected and the pressure amended to centre this ring on the diaphragm aperture.

[5]Two of these surfaces come from the Mangin Mirror, reflective and refractive surfaces, and one from the plano-convex Chromatic Corrector.

Following this, the other radii of curvature were adapted until a solution converged. The resultant design from this method shall be labelled as the 'free pressure' design. After talks with engineers at CERN sparked safety concerns, the focus shifted to finding designs at lower pressures.

Similarly to the free pressure design, an iterative approach was also utilised. However this time, the Mangin Mirror radii of curvature were independently modified to minimise the width of the kaon light ring, and the radius of curvature of the Chromatic Corrector was used to centre the light ring at the diaphragm aperture. A limitation found with this method was that it is only valid for small changes to the Chromatic Corrector radius of curvature due to this consequently changing the width of the light ring at the diaphragm. Thus an alternate method was also used. Here designs were found by successive scans with increasing granularity, before then applying the iterative method to fine tune the solution. In addition to reducing the computational power required to find solutions, this also tested the stability of the solution.

In addition to modifying the radii of curvature of the lenses, the surface area of each lens was also investigated. Whilst the outer radius cannot be changed due to the constraints of not modifying the support structures, the inner radius can. An increase in the light focused onto the diaphragm aperture was achieved by reducing the Mangin Mirror inner radius while ensuring that the particle beam could still pass through safely. Values decreasing from the nominal 50 mm to 30 mm show an approximately linear increase in the number of photons measured at the diaphragm due to the surface area increasing proportional to $r\,\mathrm{d}r$, see Figure 3.7. The new value of the inner radius was agreed to be 40 mm such that the beam can pass through without interacting with the lens.

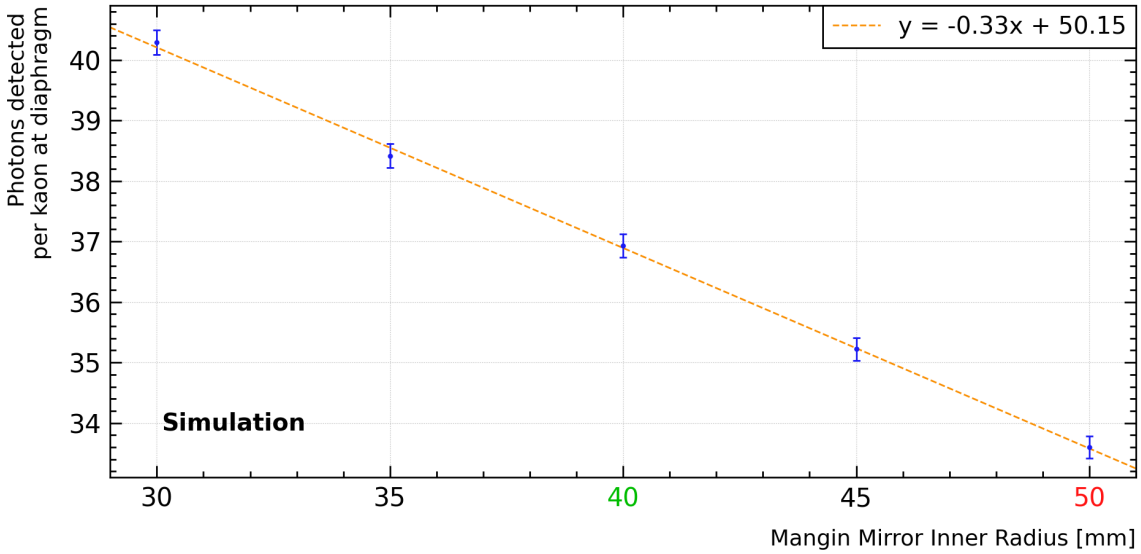

Figure 3.7: Number of photons measured at the diaphragm aperture, weighted with the QE of the PMTs, as a function of the inner radius of the Mangin Mirror. As the inner radius is reduced, the surface area of the mirror increases and thus the number of detected photons increases. Here the NA62 Cedar-W value is highlighted in red, whilst the new agreed upon value for Cedar-H is highlighted in green.

3.3.2 Further KTAG optical considerations

When optimising the KTAG optics to work with Cedar-H there were two requirements: first that the light was correctly directed towards the PMTs, and secondly that the light spot formed was of an appropriate size and shape. It was found that the Condenser lens from Cedar-W, rather than that from Cedar-N, was the better starting point, since the further changes required to the optics were minimal. These involved replacing the eight spherical mirrors that directed light onto the PMT arrays with a minor adjustment to their radial position. As an aside it was found that spherical mirrors formed by convex lenses with a radius of curvature, $r = 77.52\,\text{mm}$, available from an optical catalogue are perfectly satisfactory; no significant gain was achieved when customising the radius of curvature. The posibility to change the lenses immediately outside the eight quartz windows was investigated but found to be unnecessary.

3.3.3 Performance of CEDAR designs

In Table 3.1 the performance of the redesigned KTAG for six Cedar-H designs (1 free pressure, 5 fixed pressure) can be seen, compared with the performance of the Cedar-W filled with nitrogen. The comparison is made using the identical NA62MC framework, where Cedar-W is optically and mechanically unchanged from the detector used up until 2022. We note that the predicted (average) number of photoelectrons detected per kaon is higher for Cedar-W than is measured in the experiment and assume this to be true also for Cedar-H.

From Table 3.1 it can be seen that the Gaussian width of the kaon ring decreases with increasing pressure, while the light yield at the diaphragm increases, as more Cherenkov photons are emitted. This might suggest that the performance of KTAG would be superior at higher pressures. However, this is not the case for two reasons. First, the width of the kaon ring is small compared with the aperture of the diaphragm and all light is collected, so that a decrease in ring width does not bring an added benefit. Secondly, as the pressure increases so does the Cherenkov angle and the size of the spot at the PMT array. Thus, we see a roughly constant number of photoelectrons detected as the pressure increases. Finally, we note from Table 3.1 that both the kaon identification efficiencies and pion misidentification probabilities more than meet the requirements set out in the NA62 design specification [58] at all pressures, and indeed the predicted average number of detected photoelectrons per kaon is approximately 30% higher for Cedar-H than for Cedar-W.

Table 3.1: Performance of Cedar-H designs. The kaon tagging condition is the time coincidence of photons detected in at least 5 sectors; similarly the pion misidentification is also for a coincidence of at least 5 sectors. For comparison, the values for NA62 Cedar-W have also been included.

Pressure [bar]	Gaussian width of K^+ ring [mm]	Photons at diaphragm per K^+	Photons at PMTs per K^+	Photons at PMTs per π^+	K^+ identification efficiency [%]	π^+ mis-identification probability
3.70	0.43	37.3	32.1	0.09	99.2	$\lesssim 10^{-4}$
3.80	0.36	38.1	32.3	0.11	99.5	$\lesssim 10^{-4}$
3.90	0.38	38.8	32.8	0.10	99.5	$\lesssim 10^{-4}$
4.00	0.33	39.3	32.9	0.16	99.6	$\lesssim 10^{-4}$
4.10	0.27	39.5	32.1	0.33	98.8	$\lesssim 10^{-4}$
4.54	0.24	41.0	31.3	0.49	99.6	$\lesssim 10^{-4}$
Cedar-W (N_2 @ 1.71 bar)	0.27	33.8	23.5	0.04	99.2	$\lesssim 10^{-4}$

3.4 Proposed KTAG with Cedar-H at 3.8 bar

A pressure of 3.8 bar has been chosen for Cedar-H, which combines a well-behaved distribution of light at the diaphragm aperture, Figure 3.8, with excellent illumination of the PMT array, Figure 3.9. The path of light through CEDAR and into the KTAG can be seen in Figure 3.10. A further comparison of its performances with NA62 Cedar-W is given in Table 3.2, where the numbers of 4- and 5-fold coincidences for 1,000 kaons and 10,000 pions are presented. The choice to simulate 10 times more pions better reflects the beam composition and also allows us to measure the pion misidentification probability to the order of 10^{-4} as specified in the design specification [58]. We see that this design meets this criteria.

Due to the predicted 30% increase in the number of detected photons compared with Cedar-W, care needs to be taken to ensure the read-out electronics can process such an increase of PMT hits. Figure 3.11 shows the simulated hit rate in the PMTs for a nominal kaon rate of 45 MHz [51] and CEDAR filled with hydrogen. The maximum rate that the current read-out system can process is 5 MHz [82] and for PMTs exceeding this value, a partial loss of detected photons is expected. A decrease in the number of detected photons could lead to a degradation of the kaon

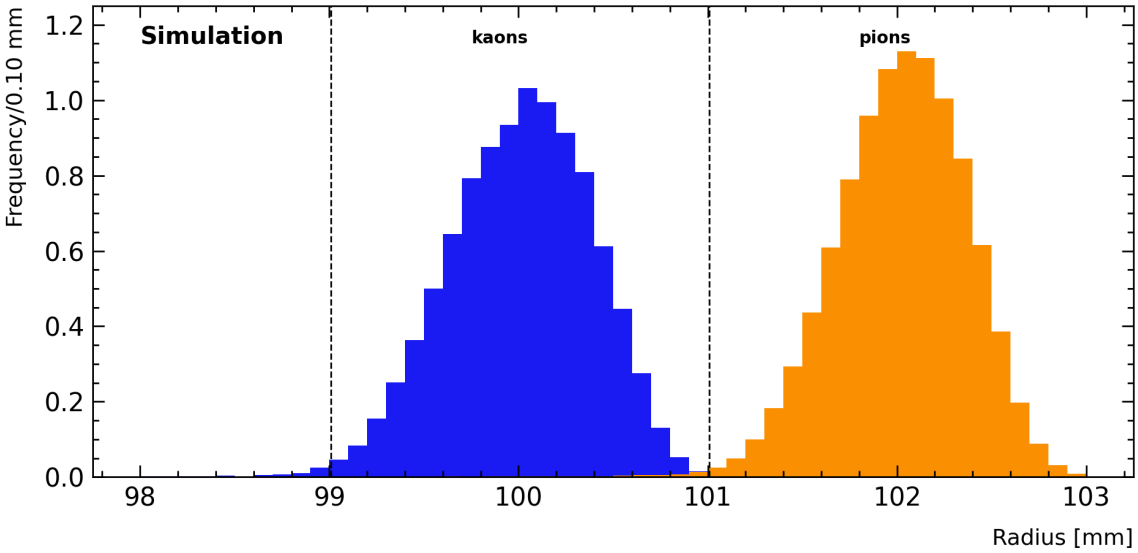

Figure 3.8: Light distribution at the diaphragm for the Cedar-H with radiator gas pressure of 3.80 bar. 1000 kaons (left) and 1000 pions (right) have been simulated. Quantum Efficiency (QE) of the PMTs has been applied.

identification efficiency. Therefore, if the simulated hit rate in the PMTs is confirmed with data, tuning of the beam intensity or of the photon distribution on the PMT planes can be used to ensure good detector performance.

Figure 3.12 shows the radius at the diaphragm as a function of wavelength for the new Cedar-H, contrasted with the unoptimised Figure 3.5b. The kaon light is now contained inside the diaphragm aperture excluding wavelengths below 200 nm. These wavelengths can safely be ignored as the QE of the PMTs is negligible at this wavelength in addition to UV filters that are applied to the Cedar-H Quartz Windows also minimising the contribution of this light.

Table 3.2: Performance of KTAG for the new Cedar-H and NA62 Cedar-W. Both designs show a high probability of identifying kaons with a low probability of detecting pions.

CEDAR design	1,000 kaons		10,000 pions	
	≥ 4 sectors	≥ 5 sectors	≥ 4 sectors	≥ 5 sectors
Cedar-H	995	995	3	0
Cedar-W (N_2)	993	992	2	0

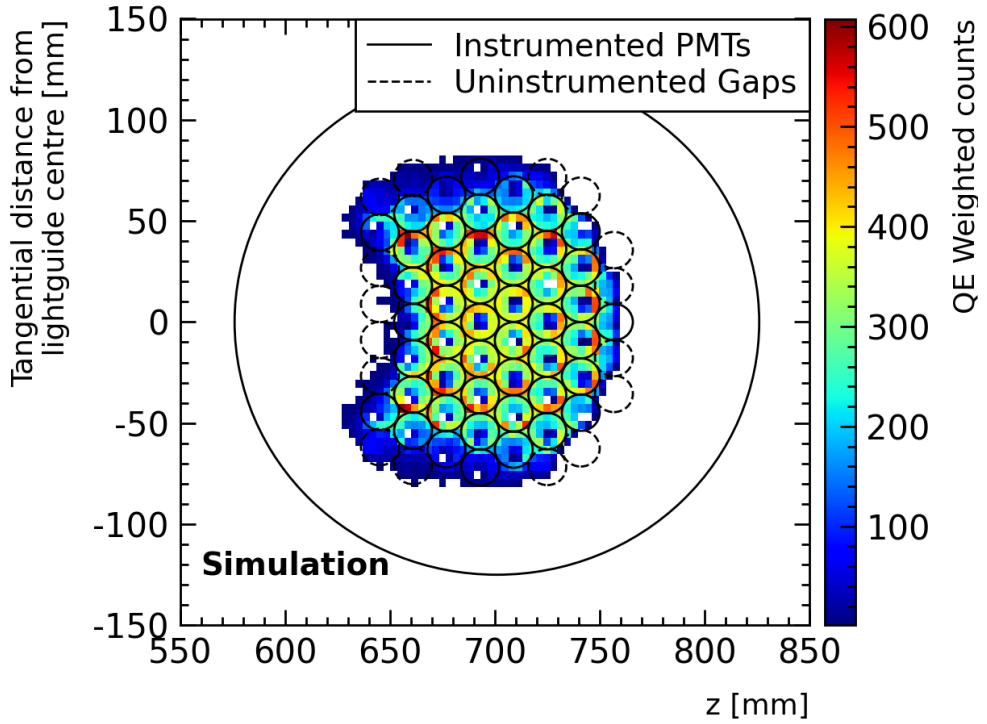

Figure 3.9: Distribution of light over the PMT array for a hydrogen radiator gas pressure of 3.80 bar. The circled areas indicate either an instrumented PMT (solid line) or uninstrumented gap (dashed line) where a PMT may be placed if this would be beneficial to the number of photons detected.

When calibrating CEDAR the pressure must be adjusted to obtain the maximum kaon yield; for this to be successful the pion and kaon peaks must be separated. Figure 3.13a shows a simulated pressure scan (on a linear scale) displaying the pion and kaon peaks for a diaphragm aperture of width 2 mm and perfect alignment of the detector with the beam. The kaon and pion peaks are clearly distinguishable. Such perfect alignment is unlikely to be achieved, however, and the effect of a misalignment of 100 µrad, comparable to the beam divergence of 70 µrad, is shown in Figure 3.13b. The separation between the kaon and pion peaks is lost for 4-fold coincidences, but reappears for 5- and 6-fold coincidences.

Table 3.3 summarises the parameters in the new Cedar-H design that have been modified from the NA62 Cedar-W; a complete list of all KTAG parameters for each changed component is given in Appendix A.

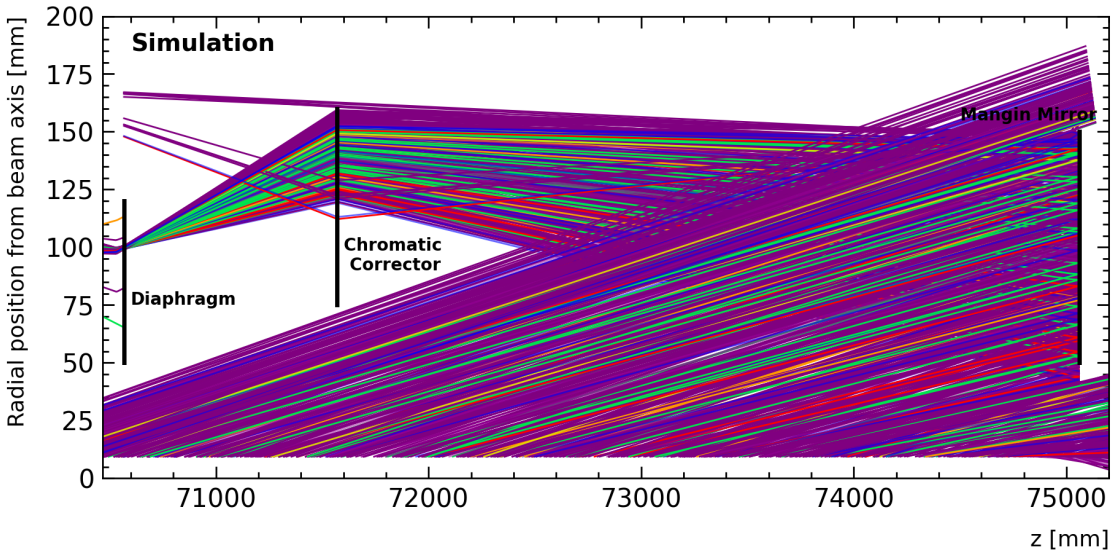

(a) CEDAR internal optics. Cherenkov photons emitted by kaons are traced from the beam (bottom) to the Mangin Mirror (right), they are reflected back towards the Chromatic Corrector and refracted onto the diaphragm plane.

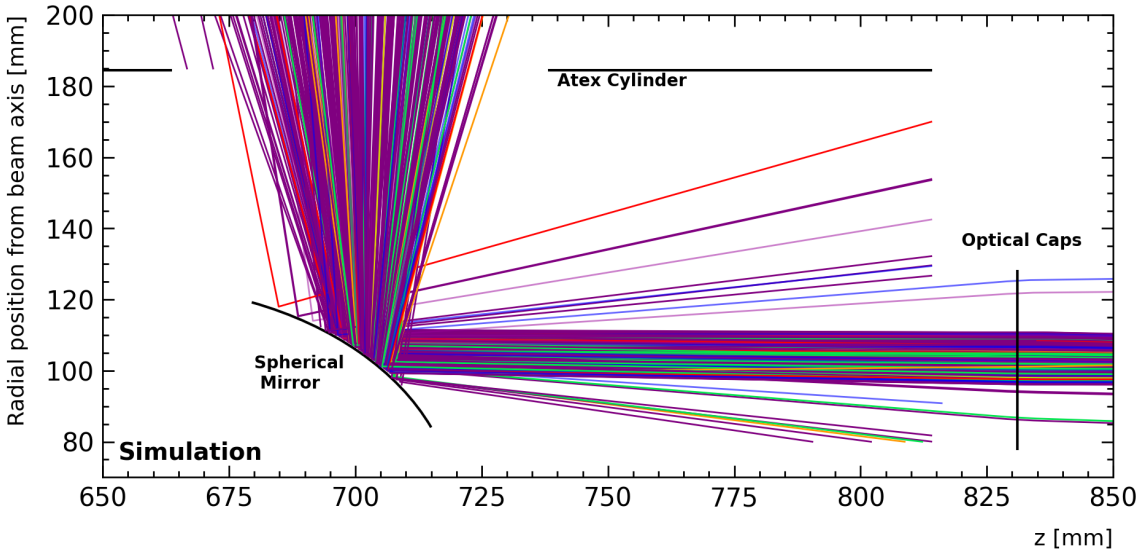

(b) CEDAR external optics. After the diaphragm, photons are focused by condenser lenses onto 8 Quartz Windows followed by optical caps before being reflected radially outward by 8 spherical mirrors and into the lightguides containing the PMT arrays.

Figure 3.10: Ray tracing through the CEDAR for a hydrogen radiator gas at 3.80 bar pressure. Here the colour of each line approximately represents its wavelength.

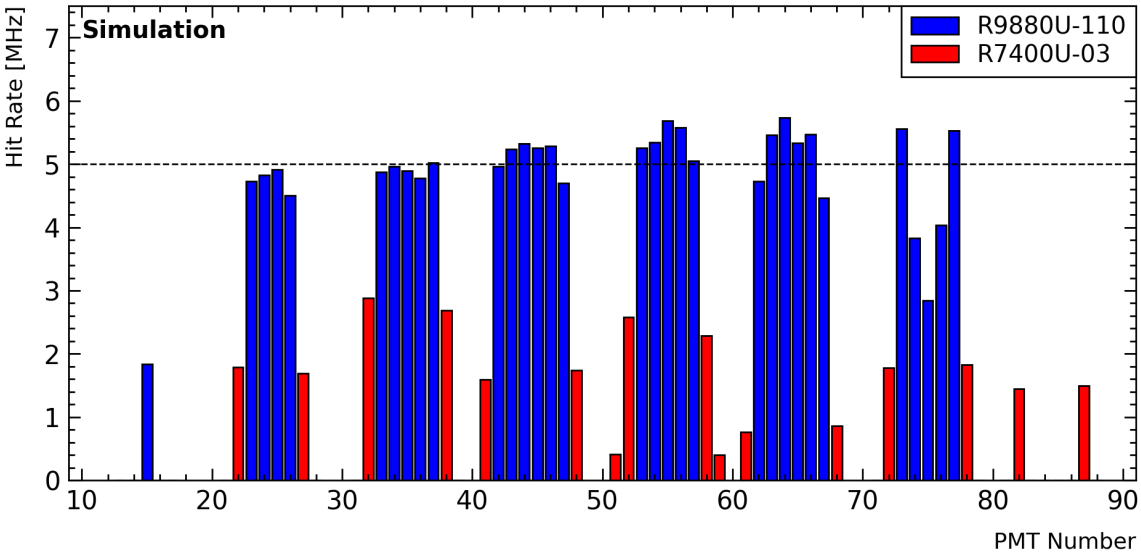

Figure 3.11: Average hit rate in each photomultiplier tube (PMT) for the new Cedar-H design assuming a kaon rate of 45 MHz. The colour of each bar represents the type of PMT used with those in blue operating with a higher quantum efficiency than those in red. Current electronics allows for a maximum of 5 MHz (dashed line) per channel with any additional information lost.

Table 3.3: Required changes to the CEDAR internal and external optics for the new Cedar-H design. All other parameters remain unchanged from the NA62 Cedar-W and are reported in the appendix.

Parameter	Value [mm]
Pressure	3.80 bar
Mangin Mirror reflective radius of curvature	9770
Mangin Mirror refractive radius of curvature	8994
Chromatic Corrector radius of curvature	1307
Mangin Mirror inner radius	40
Spherical Mirror surface radius	77.52
Spherical Mirror radial offset	106.0

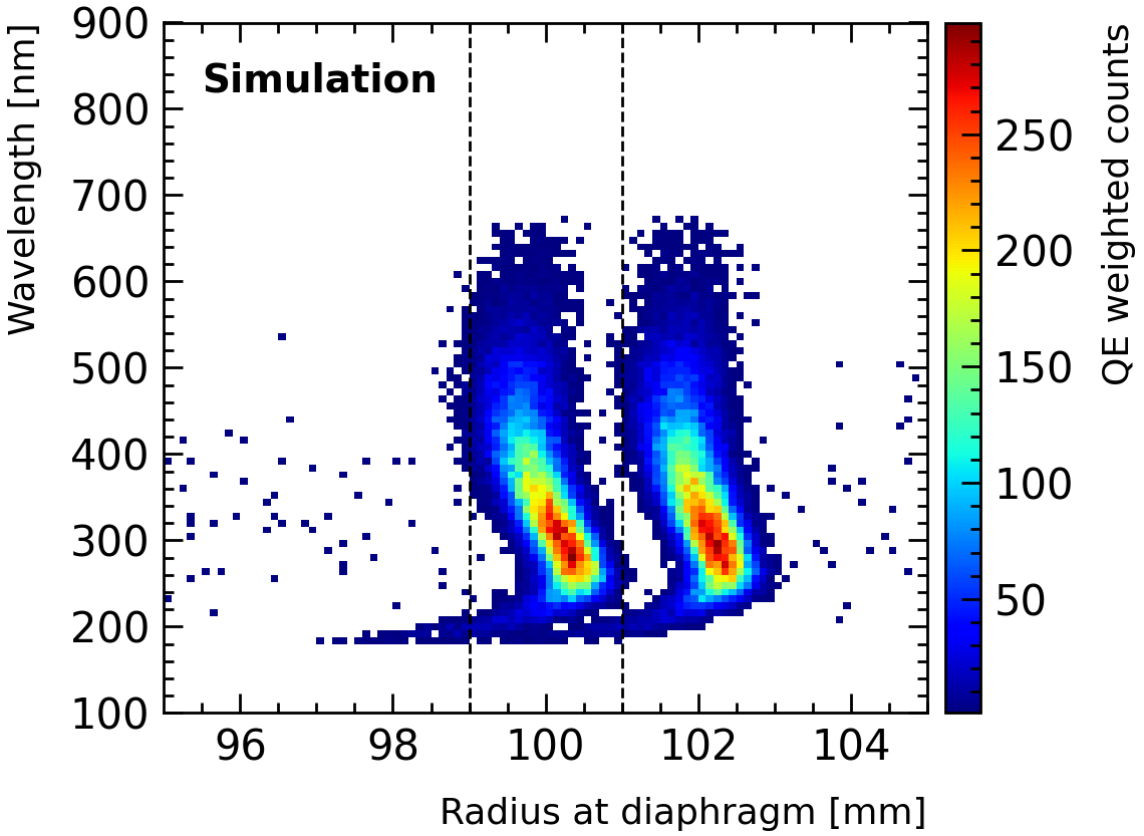

Figure 3.12: Photon radius at the diaphragm versus their wavelength for Cedar-H. The light from kaons is that focused through the diaphragm aperture (shown by the dashed lines) and the pion light is focused at a larger radius. 1000 kaons and 1000 pions are simulated.

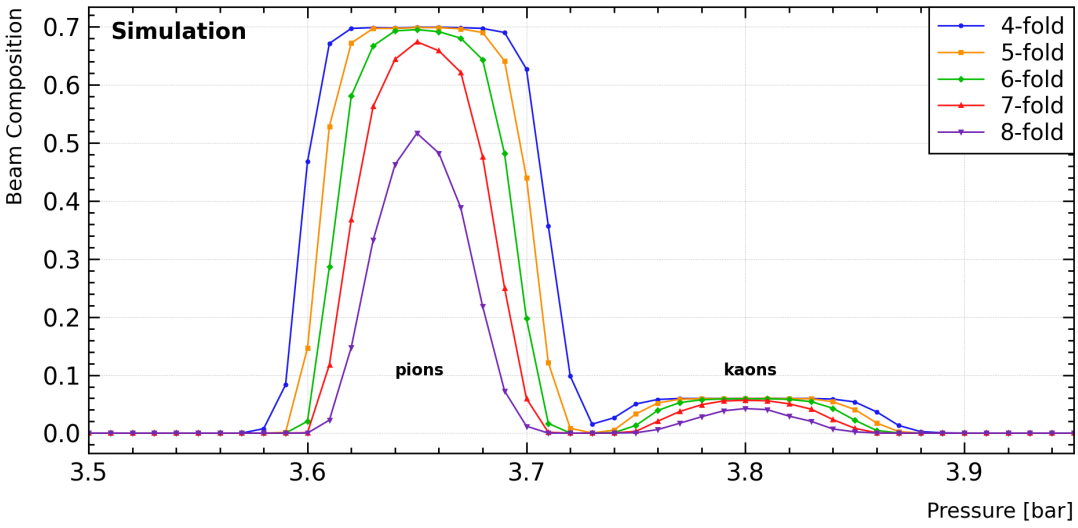

(a) Perfectly aligned CEDAR

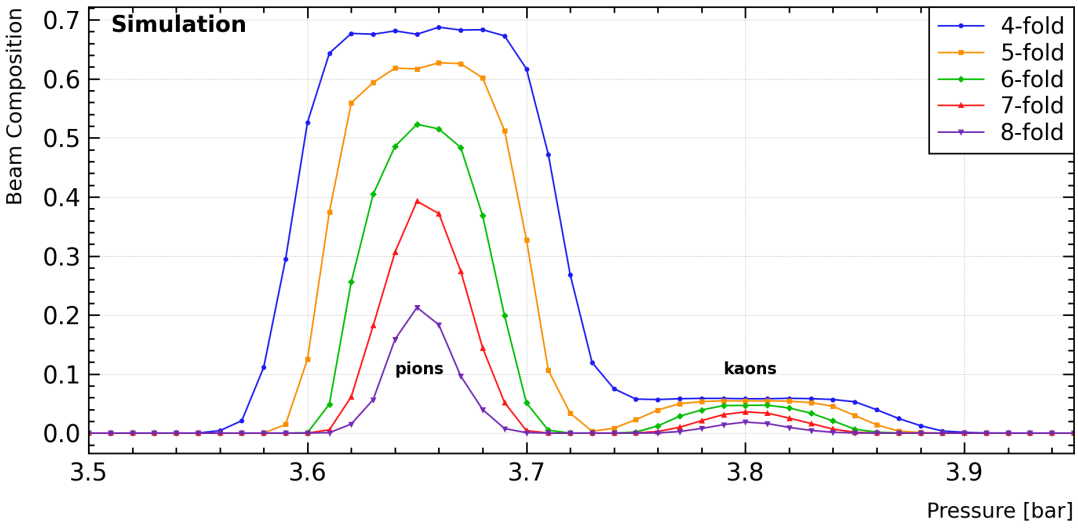

(b) Misalignment of the Mangin Mirror by 100 µrad

Figure 3.13: Pressure scans for Cedar-H with a diaphragm aperture of 2 mm.

3.5 Tolerances on optical and mechanical parameters

In order to build the new Cedar-H it is necessary to determine the tolerances on the radii of curvature of the three optical surfaces and locations of their centres of curvature, together with the angles of tilt of the Mangin Mirror and Corrector Lens, so that the detector performs as expected. To calculate these tolerances, each parameter was individually varied and the number of photoelectrons at the PMTs calculated. A loss of 10% in the average number of detected photoelectrons per kaon was chosen as a measure of the tolerance on each parameter. There are three reasons why the loss may occur:

- altering of the light ring radius at the diaphragm;
- broadening of the light ring;
- displacement/distortion of the light ring.

Of these, the changing radius can be accommodated by a change in the gas pressure, while the broadening of the light ring was found to be insignificant. Light losses resulting from a displacement of the ring cannot be recovered, and thus strict tolerances need to be found for the parameters that cause this. In general, any parameter that breaks the cylindrical symmetry of the CEDAR will cause a displacement or distortion of the ring, and so the tolerances on the alignment of the lenses, together with the positions of their centres of curvatures, are likely to be critical.

Table 3.4 shows the required tolerances for building the Mangin Mirror and Chromatic Corrector for the new Cedar-H design along with their alignment in the CEDAR vessel. It is important to note that the tilt of each lens is defined as the z distance between the outer radius of the lens and its nominal position.

Additionally, the tolerance of non-uniformity in refractive index was assessed by randomly choosing a value of refractive index, n, from a Gaussian distribution for each Cherenkov photon intersecting the lens. The tolerance is the RMS of the distribution that results in a 10% reduction in the detected number of photoelectrons. All parameters are straightforward for a manufacturer to achieve, but great care is required when aligning the Mangin Mirror inside the CEDAR vessel as the tolerance is exceedingly small.

All plots used in calculating the tolerances can be found in Appendix A.2 with the tolerance on the refractive index described further in Appendix A.3.

Table 3.4: Tolerances for building and positioning the new lenses and mirrors in Cedar-H.

	Value
Mangin Mirror	
Radial Position of Lens [mm]:	1.00
Radius of Curvature (reflect) [mm]:	50
Radius of Curvature (refract) [mm]:	100
Radial Position of Centre of Curvature (reflect) [mm]:	0.7
Radial Position of Centre of Curvature (refract) [mm]:	2.0
Thickness [mm]:	5
Tilt (dZ) [μm]:	15
Δn/n	2%
Chromatic Corrector	
Radial Position of Lens [mm]:	2.0
Radius of Curvature [mm]:	10
Radial Position of Centre of Curvature [mm]:	1.7
Thickness [mm]:	5
Tilt (dZ) [mm]:	15
Δn/n	0.1%
Spherical Mirror (KTAG)	
Radial Offset [mm]:	1.50
z Position [mm]:	10.0

3.6 Summary

3.6.1 Summary of this work

A new Cedar-H at 4.54 bar pressure was designed before safety concerns shifted the focus of the project to lower working pressures. Designs ranging from 3.70 bar to 4.10 bar were presented as alternate solutions to the problem. All of these designs were based on a Cedar-N but required changes to the Mangin Mirror and Chromatic Corrector radii of curvature whilst maintaining the support structures as requested by CERN engineers. In addition, the condensers are changed to Cedar-W and new spherical mirrors are required to maximise the light detected in the KTAG.

A satisfactory design of a Cedar-H, using hydrogen at 3.8 bar as the Cherenkov radiator, has been developed and its performance shown to compare favourably with the current Cedar-W filled with nitrogen. The methodology employed has been shown to be robust, cross-checked with an independent study, and the tolerances on all parameters determined.

3.6.2 Since leaving the project

This section outlines work not carried out by the author but has been included for completeness. The 3.80 bar Cedar-H design was approved and built by CERN engineers [89]. Performance of the new Cedar-H was evaluated in a dedicated test beam including pressure scans identifying the kaon, pion and proton peaks [90].

Further simulations of Cedar-H revealed a decrease in the number of L0 triggers caused by beam scattering upstream of GTK3. Specifically, 37% of beam tracks measured on data in the L0 output of the $K^+ \to \pi^+\nu\bar{\nu}$ trigger mask exhibit scattering upstream of GTK3. For Cedar-W with nitrogen, 0.08% of simulated events included

a track with scattering upstream of GTK3, whilst this value is reduced to 0.05% for Cedar-H, representing a reduction of 37.5%. Consequently, the effect on spurious L0 triggers amounts to 14% (37% $\times$ 37.5%), resulting in a reduction of approximately 320,000 triggers per burst at L0 for the $K^+ \to \pi^+\nu\bar{\nu}$ trigger mask.[6] It is worth noting that scattered beam particles also contribute to other trigger masks, although to a lesser extent.

With the successful test beam and the expected reduction in trigger rate, Cedar-H was approved for use in NA62 and has successfully been installed at the beginning of 2023 replacing the Cedar-W containing nitrogen. Preliminary results on data collected in 2023 show improved performance with hydrogen, 21.5 photons per kaon, compared to that with nitrogen, 18 photons per kaon.

[6]This is approximately 10% of the total L0 trigger rate.

Chapter 4

Beam intensity simulations

In this chapter, the simulation of pile-up in the NA62 detector is described. Pile-up refers to the additional events that occur in a small time window surrounding the interesting physics event. High-energy physics experiments often strive for the highest beam intensity with the aim of maximising the amount of data collected provided that this can be efficiently analysed. An increase in intensity comes with the caveat of more pile-up events. Hence, Monte-Carlo (MC) simulations of these overlapping events are vital in describing the data, and care is needed to produce the intensity templates used to replicate the beam intensity in MC. Additionally, as the intensity distribution might change for each data-taking year, multiple templates are required. Therefore, it is essential to develop software that can accurately and automatically create new intensity templates as more data is collected.

4.1 Motivation for updating intensity templates

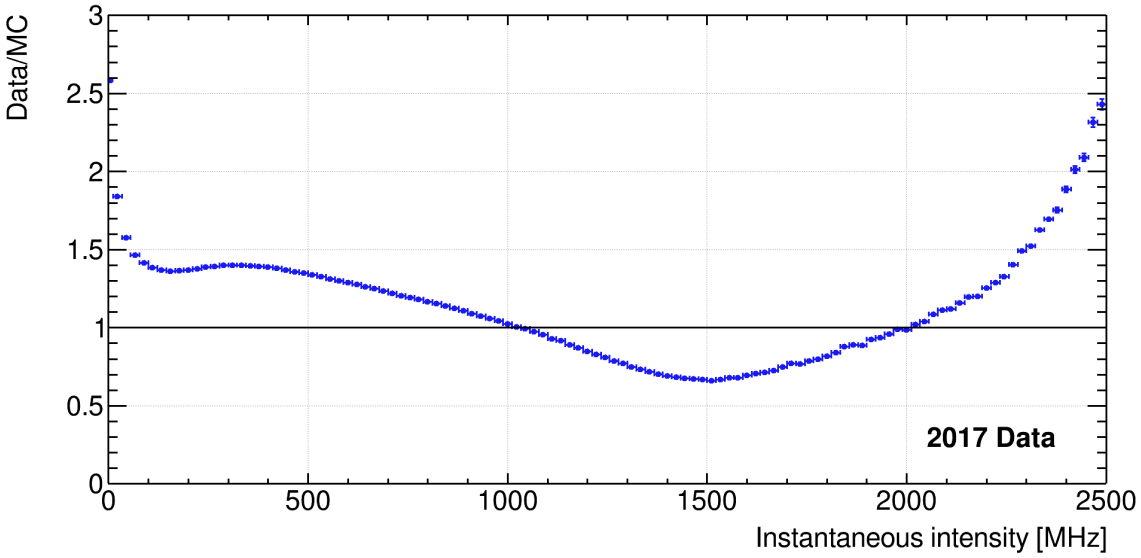

Figure 4.1: Data/MC ratio for the beam intensity measured with minimum bias data collected in 2017 and MC events generated using a beam intensity template based on 2017 NA62 run conditions.

To reproduce the distribution of instantaneous intensity observed in data within MC simulations, one requires some input template, which is then sampled. The intensity sampled from this template distribution is denoted as the true intensity value throughout this thesis. Subsequently, the sampled value undergoes convolution with detector resolutions, acceptances, and inefficiencies to yield the measured intensity desired to replicate the data distribution.

An intensity template based on 2017 run conditions, hereinafter referred to as the 2017 intensity template, was previously generated and successfully described data. Significant modifications of the software framework over time resulted in the discrepancies shown in Figure 4.1. Moreover, when considering data collected in running conditions different from those of 2017, additional intensity templates must be created.

Another factor to take into account is that this original template has a cut-off intensity at 2500 MHz. Whilst this value is reasonably large in comparison to the

design intensity of 750 MHz [58], it was found that approximately 1% of events in the 2017 dataset had intensity estimates larger than this cut-off. Therefore, as the 2017 template is to be updated, and templates for other data taking periods are needed, the cut-off value should be optimised to include high-intensity events. Additionally, providing MC simulations at higher intensities would help to better understand the impact of running the experiment at a higher beam intensity.

4.2 The beam intensity

The instantaneous intensity of the NA62 beam is estimated in data by counting the number of hits in each GTK station during a given out-of-time window, defined as [-25, -2.5] ns and [2.5, 25] ns around the trigger time of an event. The central part of the window, [-2.5, 2.5] ns, is excluded to avoid hits from the physics event that would bias the estimate. In this out-of-time window of 45 ns, the number of hits, n, detected by a given GTK station is converted to an intensity estimate, I:

$$I = \frac{n}{45\,\text{ns}}. \tag{4.1}$$

This value is then averaged across all three (NA62 run-1) or four (NA62 run-2) stations. In an ideal situation, a beam particle will leave a single hit in each station, but this may not always be true due to detector or DAQ inefficiencies.

The intensity distribution for a subsample of data taken in 2018 is shown in Figure 4.2. The binning in the figure is obtained from Equation 4.1 for $n = 1$ with the selected time window; one bin is 22.2 MHz. Notably, a maximum is observed at 410 MHz; this corresponds to approximately 55% of the design intensity [58], and to the 2018 running conditions. The tails in this distribution are caused by the spill structure of the beam provided to NA62 and in particular a large initial spike, see Figure 4.3. This was not an issue for the lower beam intensity of NA62 run-1

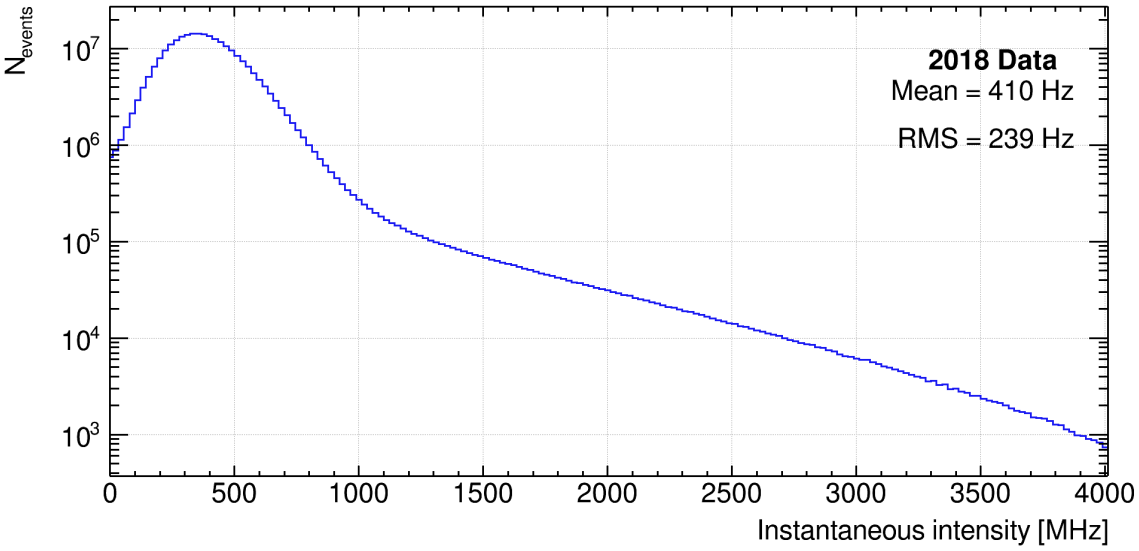

Figure 4.2: Distribution of the beam intensity for a subsample of the 2018 dataset selected with a minimum bias trigger. The number of out-of-time hits detected in the GTK is used to determine the intensity of the beam. The binning reflects the granularity of this estimator, $I = 22.2\,\text{MHz}$, and is controlled by the size of the time window used in counting hits.

however did become an issue in 2021 and consequently was fixed for 2022 onwards.

In NA62 MC simulations, a single beam particle decay, along with its secondary interactions, is called an event. To account for pile-up, additional MC events are overlaid to the interesting physics event. This leads to two questions, firstly how many events should be overlaid and secondly which event topologies.

Given an input intensity template, we can randomly select a true intensity value to be simulated. For the selected intensity value, the number of beam particles, N_b, can be calculated by rearranging Equation 4.1 and assuming a beam particle will leave a single hit in each GTK station:

$$N_b = I \times 45\,\text{ns}, \tag{4.2}$$

We note that intensity values provided to this equation are discrete and correspond to the integer values of N_b. The number of beam particles can then be split further to replicate the NA62 beam by applying a weight, W_i, corresponding to the beam

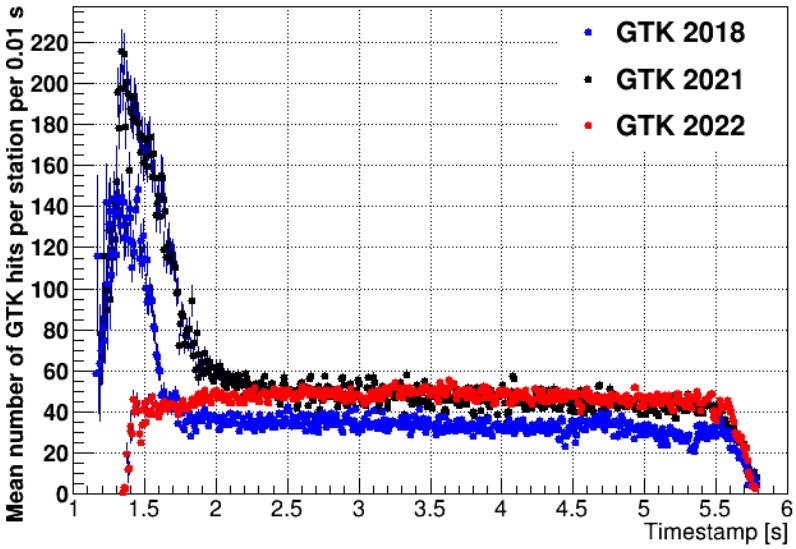

Figure 4.3: Spill structure of the beam provided to NA62 for 2018, 2021 and 2022 data-taking periods. Prior to 2022 we see a large initial spike followed by a more uniform distribution of particles leading to large tails in the intensity distribution.

particle composition, as shown in Table 4.1:

$$N_{b,i} = I \times 45\,\text{ns} \times W_i. \tag{4.3}$$

Again, this value should correspond to integer values and in the case of only a single beam particle, only a pion decay shall be overlaid. Once the number of beam particles has been selected, Poisson statistics is applied to determine the number of events that shall be overlaid together. Each event has a random timing offset applied such that an approximately uniform intensity across the given time window is observed. Hits in the same GTK channel with overlapping time windows are combined together, and an inefficiency as a function of the true intensity is applied to the number of hits ranging from 98% at zero intensity down to 92% at 2000 MHz, see Figure 4.4 [91].

Table 4.1: Weights corresponding to the beam particle composition of the unseparated NA62 hadron beam.

Particle:	K^+	π^+	p
Weight (W_i):	0.06	0.70	0.24

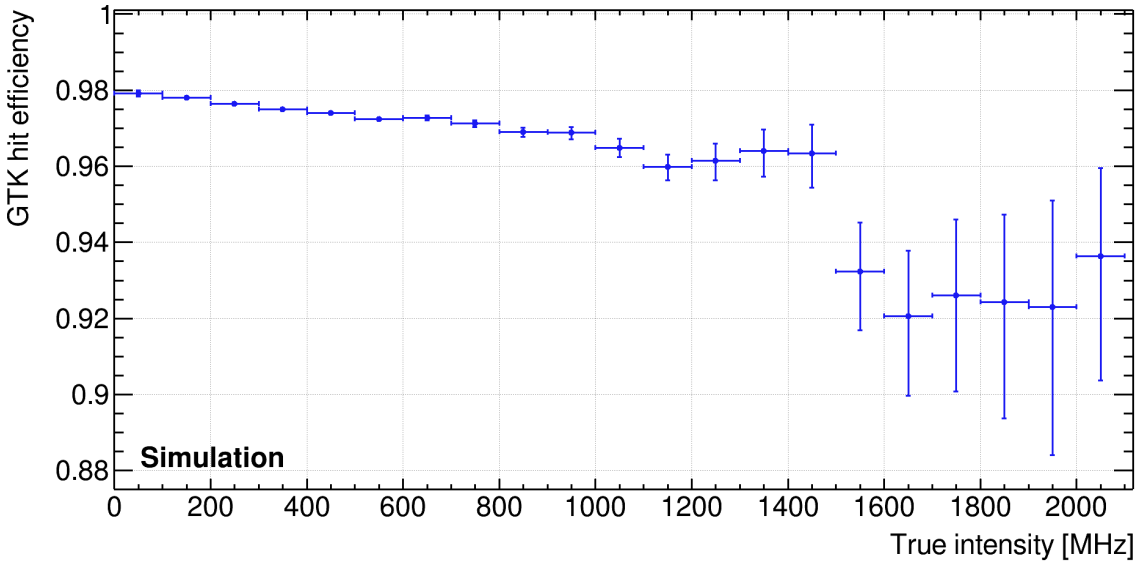

Figure 4.4: GTK hit efficiency, representing the proportion of successfully detected hits, as a function of true intensity; it is expected that each beam particle will leave one hit in each GTK station. Hits outside of this intensity range will use the efficiency of a hit at $I = 2100\,\text{MHz}$ by default.

As this study only concerns the number of hits measured in the GTK detector, the decay mode of the kaon is irrelevant. For data, a minimum bias trigger is used to provide a large dataset. Samples from each year are used independently such that the different data taking conditions can be studied and simulated.

4.3 Methods for template creation

In section 4.1, the motivations for updating the intensity template have been outlined. In this section, three potential approaches for updating the template are discussed.

4.3.1 Reweighting with data/MC ratio

One possible approach for creating the intensity template is to use the ratio of data/MC to identify deficits, or surpluses, of MC events at a given intensity. This

ratio can be used as a multiplicative factor to reweight the initial template in the corresponding intensity bins, resulting in an increase or decrease in the number of events in bins with deficits or surpluses, respectively. This updated template can then be used to generate a new MC sample and the ratio validated.

However, there are some caveats to this approach. Firstly, since each measured intensity value does not originate from a single true intensity value, this simplified approach requires multiple iterations to converge to an accurate template. Secondly, as we only reweight the measured intensity values, there is no guarantee that the template will converge. This makes this method unreliable as an automatic method for generating templates.

4.3.2 Reweighting with 2D histogram

An improved method for updating the intensity template is to exploit the MC in the reweighting procedure by generating a plot of the measured intensity as a function of true intensity. For each measured intensity bin, a projection in true intensity can be extracted and scaled by the corresponding data/MC value. To create the new template, one then needs to sum all of these scaled projections. This approach explicitly reweights the source of the measured values, i.e., the true intensity in which the measured value originated from, instead of the measured values themselves. As we do not account for how the simulation converts a true intensity into a measured intensity, an iterative approach may still be required for convergence.

4.3.3 Unfolding

The final approach discussed involves the use of linear algebra, and is known as unfolding, see Figure 4.5. It starts with the assumption that the conversion from

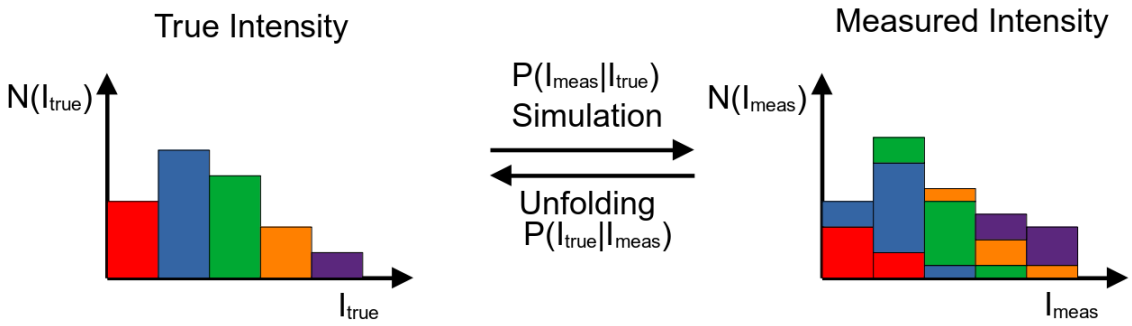

Figure 4.5: Example graphic of the folding and unfolding procedures and their relationship. The colours of each bar represent the true value of intensity and on the right we see how these are distributed in some sample measured distribution. The process of unfolding is reversing this process and 'sorting' the measured distribution back into its true bins when the truth is unknown.

true intensity template, $\underline{T}$, to measured output, $\underline{M}$, is governed by a response matrix, $\underline{\underline{R}}$, such that,

$$\underline{M} = \underline{\underline{R}}\,\underline{T}. \tag{4.4}$$

In this matrix is the detector response containing the convolution of detector resolutions, acceptances, and inefficiencies. To obtain the true intensity template from a measured output, one can multiply Equation 4.4 by the inverted response matrix to obtain:

$$\underline{T} = \underline{\underline{R}}^{-1}\,\underline{M}. \tag{4.5}$$

As we wish to replicate the data distribution in MC, the inverted response matrix can be multiplied against the measured data histogram, $\underline{D}$, to obtain an input MC template,

$$\underline{T} = \underline{\underline{R}}^{-1}\,\underline{D}. \tag{4.6}$$

This provides a consistent conversion from the measured intensity in data to the required true intensity template for MC, assuming that the response matrix can be created and inverted. However, it should be noted that this inversion of the response matrix is likely to be very computationally intensive and may be subject to precision errors.

Whilst it is possible to create a response matrix analytically, a simpler approach is to use the normalised plot of measured intensity as a function of true intensity, similar to the previous method. This approach then provides a probability map describing the likelihood of obtaining a measured intensity for any given true intensity based on our simulation framework.

One significant advantage of using the unfolding procedure is that under the assumption that the way in which MC reconstructs the chosen variable remains unchanged, the calculated response matrix remains valid. Hence, the same response matrix can be used for different data samples and conditions, as long as the simulation framework remains consistent in how the GTK is simulated. This makes the unfolding method a reliable approach that does not require iterations of MC generation like the other methods, which can be computationally intensive. Additionally, there are numerous algorithms available for unfolding that have been thoroughly tested [92]. Therefore, this method was chosen for its expected reliability and efficiency in accurately reflecting simulations.

4.4 Unfolding data

4.4.1 The response matrix

The diagonal values of the response matrix will be the largest in their respective rows and columns, with the off-diagonal values becoming smaller as they move away from the central value due to the Poissonian nature of the problem. Figure 4.6 (unnormalised), shows an example plot of a response matrix generated using the intensity template based on 2017 data as input to an MC sample. Generating the response matrix directly from the output of the MC simulation is advantageous, as it accurately reflects how true intensity is transformed into measured intensity in

the simulations despite the statistical fluctuations introduced. Care does need to be taken in distinguishing the structural components of the response matrix in relation to the statistical fluctuations introduced.

In theory, the underlying template used to create the response matrix is of little importance. There are two schools of thought, either use a flat template such that the errors across the entire intensity range are uniform or alternatively, use a more data-like template in the creation of the response matrix such that the errors around the peak are smaller whilst precision in the tails might be lost; either way a systematic error should be applied to reflect the choice in underlying distribution. For this analysis, a new flat template extending beyond the intensity range of the 2017 template, is used to improve the statistics of events at high intensity. A uniform intensity template ranging from 0–6000 MHz is used to simulate a sample of 200 million kaon decays. The resulting response matrix, shown in Figure 4.7, can be compared to the response matrix generated using the 2017 template shown in Figure 4.6. Additionally, a response matrix using 4 GTK stations, valid for NA62 run-2, is also created.

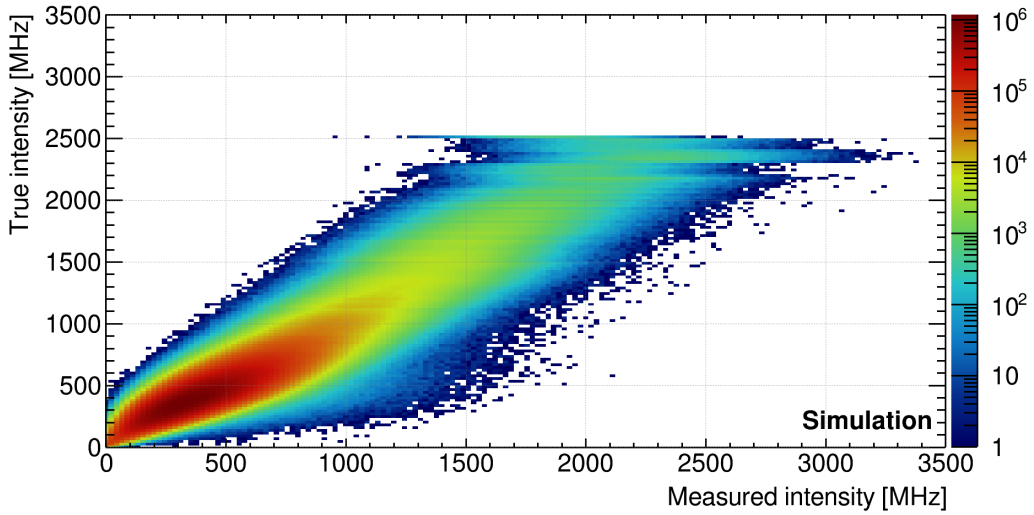

Figure 4.6: Histogram of true intensity versus measured intensity for a sample of 200 million MC events using the intensity template based on 2017 data.

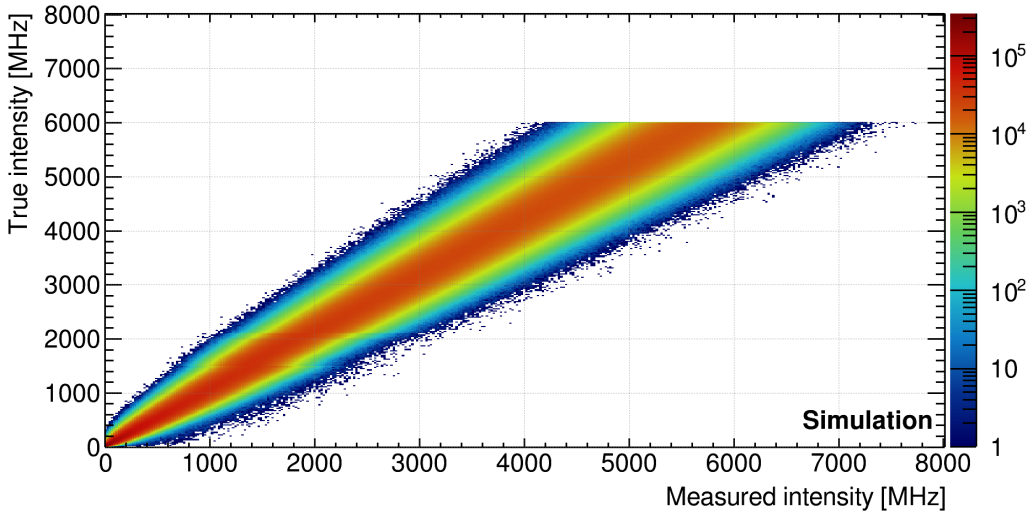

Figure 4.7: Histogram of true intensity vs measured intensity for a sample of 200 million MC events using a uniform intensity template extending up to 6000 MHz.

4.4.2 Unfolding algorithms

For the unfolding procedure, an external root package was utilised, RooUnfold [93], containing eight algorithms each with their advantages. The choice of an external package provides a straightforward approach to solving the problem with thoroughly tested algorithms. In this section, three of the methods will be discussed and a comparison of all methods can also be found in [92]. Two of these methods include an additional parameter which would need to be optimised by the user if chosen.

Bin-by-Bin

One of the simpler methods included in the RooUnfold package attempts to unfold the measured distribution by applying correction factors to the MC with no migration of events between bins. Further details of such can be found in [94]. For this method to work effectively, the measured distribution and true distribution must employ the same binning, and the detector smearing must be smaller than the bin width. However, this approach is unlikely to be feasible for the intensity distribution, which relies heavily on Poisson statistics applied to the number of tracks.

Iterative Bayesian

Also known as Richardson-Lucy deconvolution, this algorithm iteratively applies Bayes' theorem to invert the response matrix. Some advantages to this method are that it is theoretically well grounded, takes into account any type of smearing and also does not require matrix inversion [95]. The RooUnfold package uses the training truth as the initial prior, rather than a flat prior, allowing for the optimum solution to be reached in fewer iterations while not biasing the result; no additional smoothing is applied as this has been found to bias the result [93]. The regularisation strength of this method is characterised by the number of iterations, which is a parameter that would need to be optimised if chosen. As the number of iterations increases, the solution will approach the maximum-likelihood estimator. Errors on the data sample are accounted for but those on the response matrix are not.

Iterative Dynamically Stabilized Unfolding (IDS)

This algorithm, as the name implies, aims to stabilise the unfolded solution against features that are present in data but are not a part of the model [96]. This is achieved by basing the regularisation function, $f(\Delta x, \sigma, \lambda)$, on the statistical significance of the absolute difference between the observed and simulated data, Δx, with error σ; a scaling factor, λ, can also be applied. The regularisation function is smooth and monotonous ranging from 0 when $\Delta x = 0$ to 1 when $\Delta x >> \sigma$. Altering the parameters of the regularisation function affects the discrimination between real and statistical fluctuations; examples of this can be found in [96]. As a result, the convergence of this method when there are structures found only in data is improved. Caution needs to be taken with this method if the measured distribution involves background subtraction as these are errors that would need to be accounted for. This is not a problem for the use case in this thesis as no manipulation of the data is performed.

4.4.3 Selecting the method

The optimal method and, if required, its regularisation parameter for generating a new intensity template was chosen by looking at the normalised residuals between true intensity and unfolded intensity on MC samples. The decision of using MC samples over data is simple; unfolding the measured distribution of MC should return the initial template. Consequently, this can provide confidence in the method such that when data is unfolded, a template that should recreate this measured intensity will be returned.

The normalised residual bias, B, is defined as:

$$B(I) = \frac{T(I) - U(I)}{T(I)}, \tag{4.7}$$

where T and U correspond to the true (template) and unfolded intensity respectively. The bias is plotted for each of the methods outlined above, see Figure 4.8. To analyse the efficiency for each of the methods, a chi-squared per degree of freedom for a constant fit is used along with visually inspecting the resultant unfolded distributions, see Figure 4.9. Both the Iterative Bayesian and IDS methods required a regularisation parameter to be optimised and only that creating the smallest chi-squared per degree of freedom is shown.

From the plots in Figures 4.8 and 4.9, it is clear that only two methods are potentially feasible for this particular study. The iterative dynamically stabilized unfolding (IDS) method with 15 iterations, although performance drops at high intensity, and the Bayesian method with 30 iterations, consistent at all intensities. It is important to note that care needs to be taken to ensure that the model is not overfitted, thus whilst these are the number of iterations producing the lowest chi-squared per degree of freedom, a satisfactory result may be produced from a lower number of iterations. To verify this, templates were produced at varying numbers of

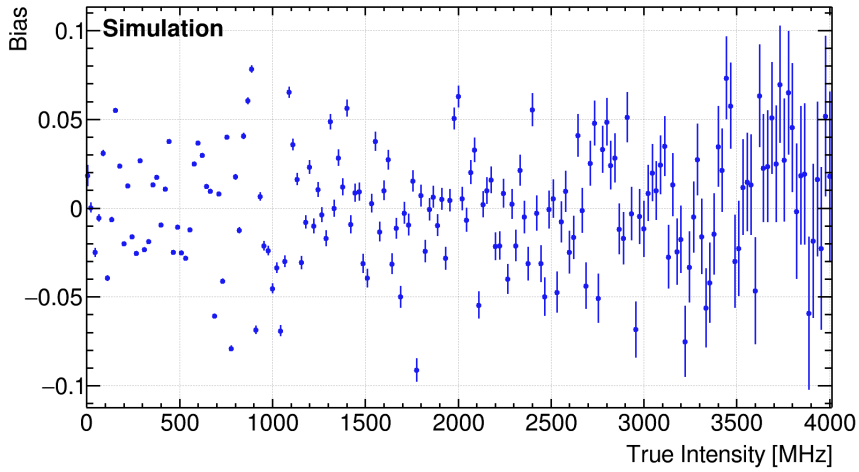

(a) Iterative Bayesian method (30 iterations)

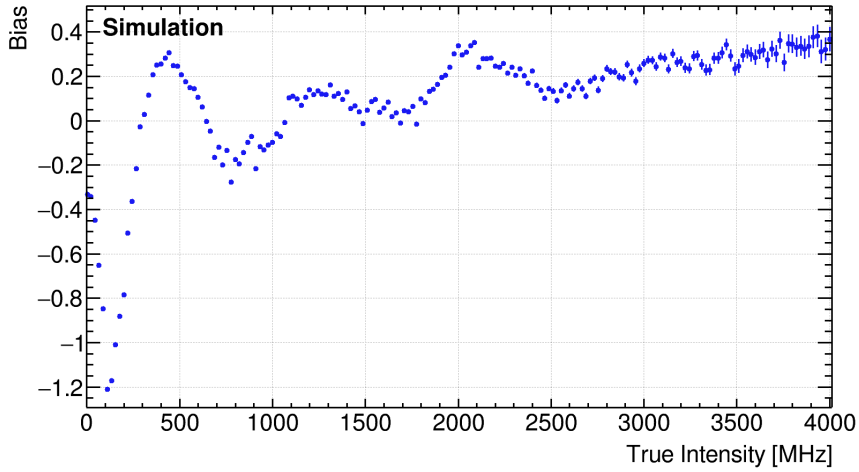

(b) Bin-by-bin method

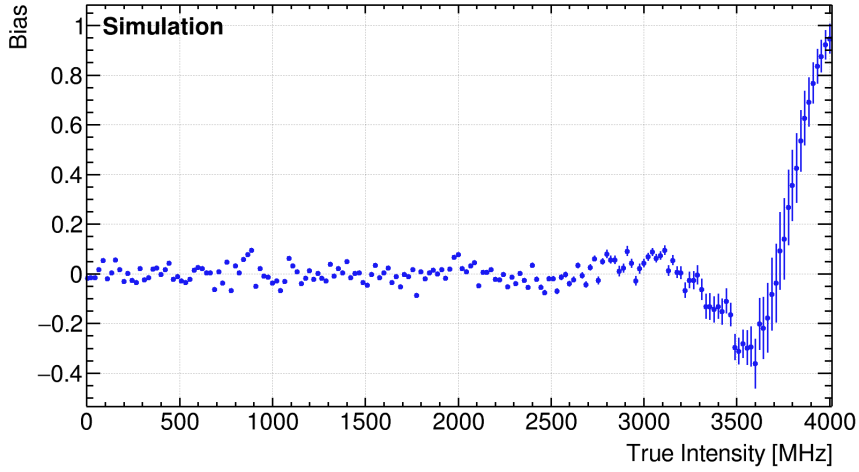

(c) IDS method (15 iterations)

Figure 4.8: Distribution of the bias defined in Equation 4.7 as a function of intensity for each of the four methods described in this thesis from the external RooUnfold package. The expected bias should be zero across all of the intensity range. Each plot has been fitted with a zeroth order polynomial and chi squared per degree of freedom has been calculated to aid in choosing the optimal method.

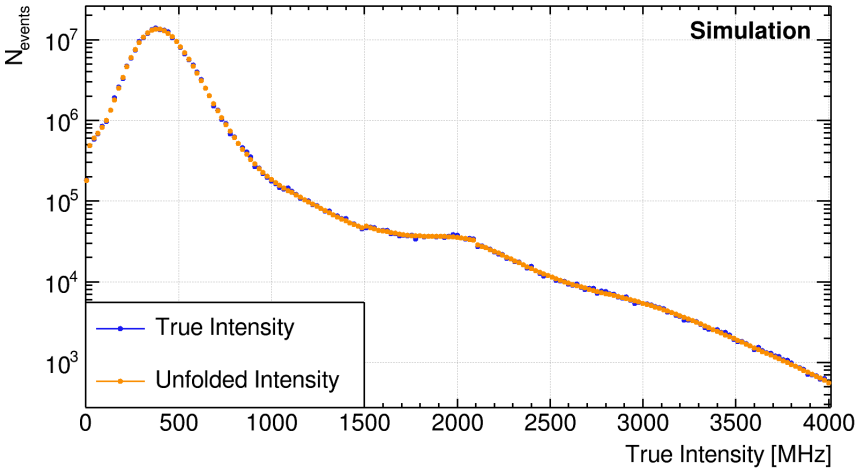

(a) Iterative Bayesian method (30 iterations)

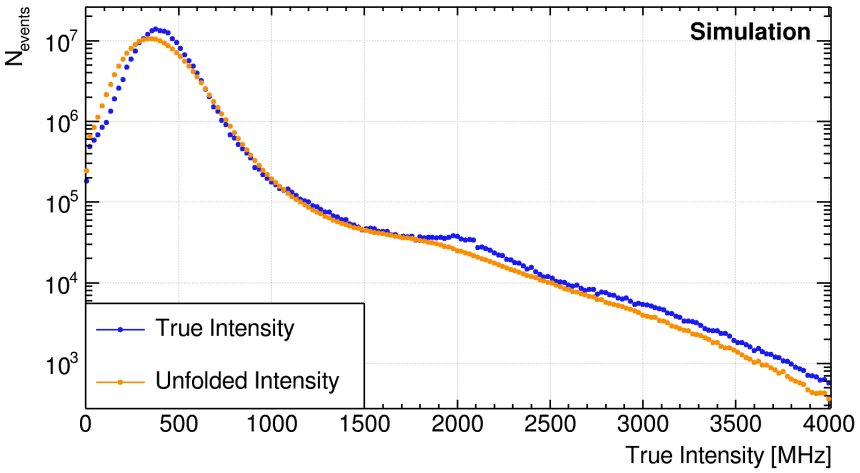

(b) Bin-by-bin method

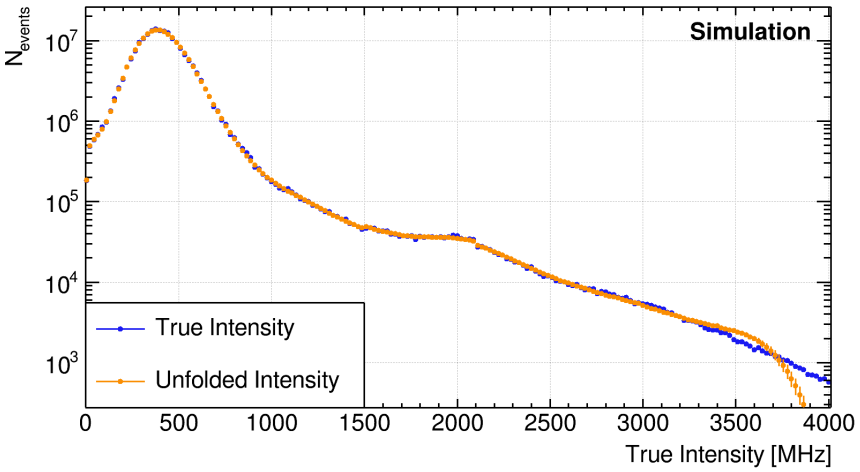

(c) IDS method (15 iterations)

Figure 4.9: Plots showing the true intensity input into the MC simulations alongside the unfolded truth distributions from applying each of the four methods described in this thesis from the external RooUnfold package to the measured output. The expected behaviour is that the two curves should match completely.

iterations for each of these methods and compared. It was found that 20 iterations was satisfactory for the Bayesian unfolding method to avoid this overfitting whilst the IDS remained at 15 iterations.

New templates were created by unfolding minimum bias data collected in 2018 with the Bayesian and IDS methods. Overlay MC was generated using these templates, and the data/MC ratio is plotted in Figure 4.10. From this, one can see that while both provide reasonable results, Bayesian unfolding seems to perform better overall.

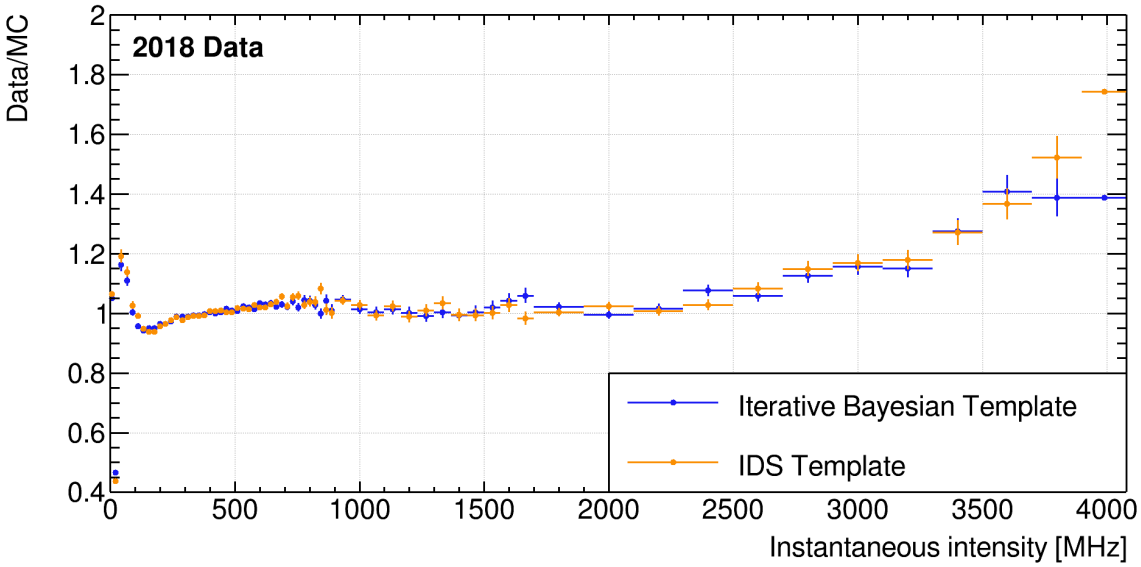

Figure 4.10: Data/MC ratio using minimum bias data taken in 2018 and MC generated using the templates created by unfolding this data using the Iterative Bayesian method (blue) and Iteratively Dynamically Stabilised unfolding method (orange).

4.5 New MC templates

Templates for each data year were produced by unfolding the intensity distribution for their respective datasets using the Bayesian unfolding method with 20 iterations. The resulting templates can be seen in Figure 4.11. Here we see a clear need for the different templates especially when considering the NA62 run-1 (2017

and 2018) templates versus the NA62 run-2 (2021 and 2022) templates. Moreover we note the improved spill structure of 2022 in comparison to the previous data-taking conditions.

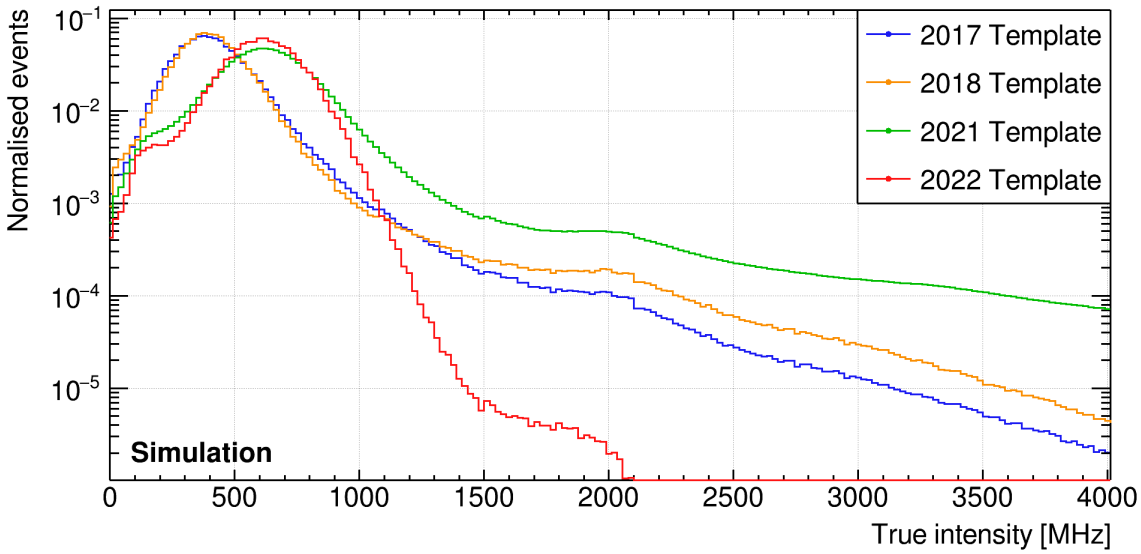

Figure 4.11: Normalised intensity templates for each data year utilising the iterative Bayesian unfolding algorithm with 20 iterations.

With the templates prepared, MC can be produced for each data year and compared to their respective datasets. Figure 4.12 shows the resulting data/MC ratio for the 2017 run conditions using the updated template, in contrast to the old data/MC ratio shown in Figure 4.1. Overall there is good agreement across the intensity range 0–4000 MHz. Similarly, we see good agreement for the templates: 2018 in Figure 4.13, 2021 in Figure 4.14, and 2022 in Figure 4.15 respectively.

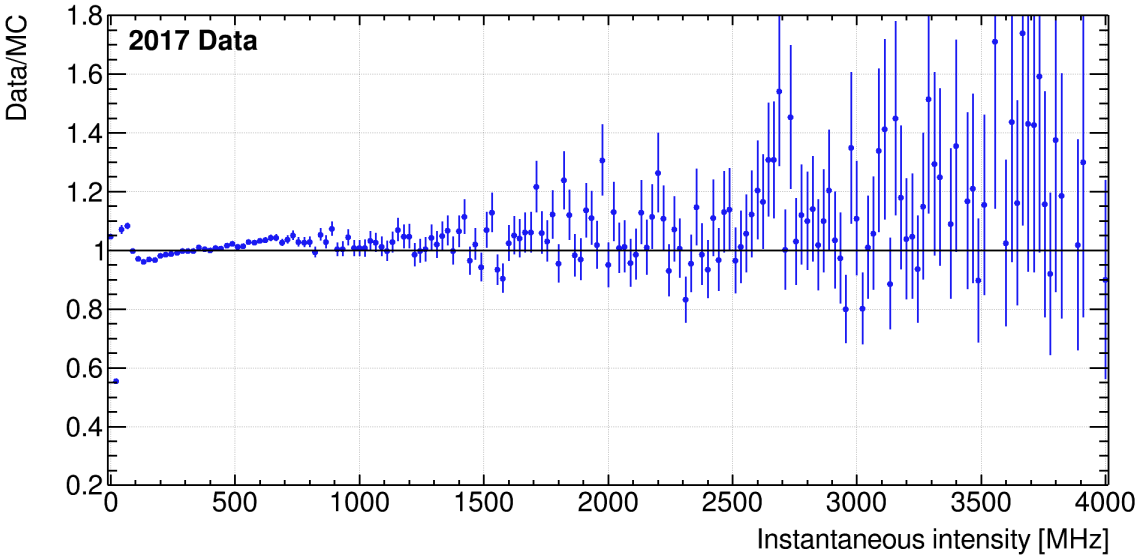

Figure 4.12: Data/MC for the beam intensity using minimum bias data collected in 2017 and MC generated using the updated 2017 template produced by using the Bayesian unfolding method.

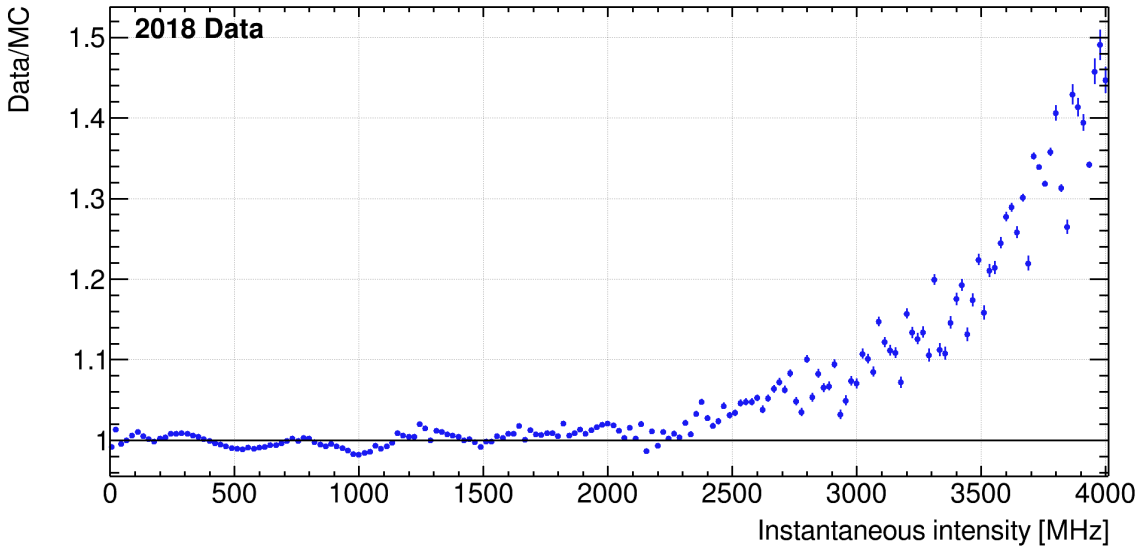

Figure 4.13: Data/MC for the beam intensity using minimum bias data collected in 2018 and MC generated using the new 2018 template produced by using the Bayesian unfolding method.

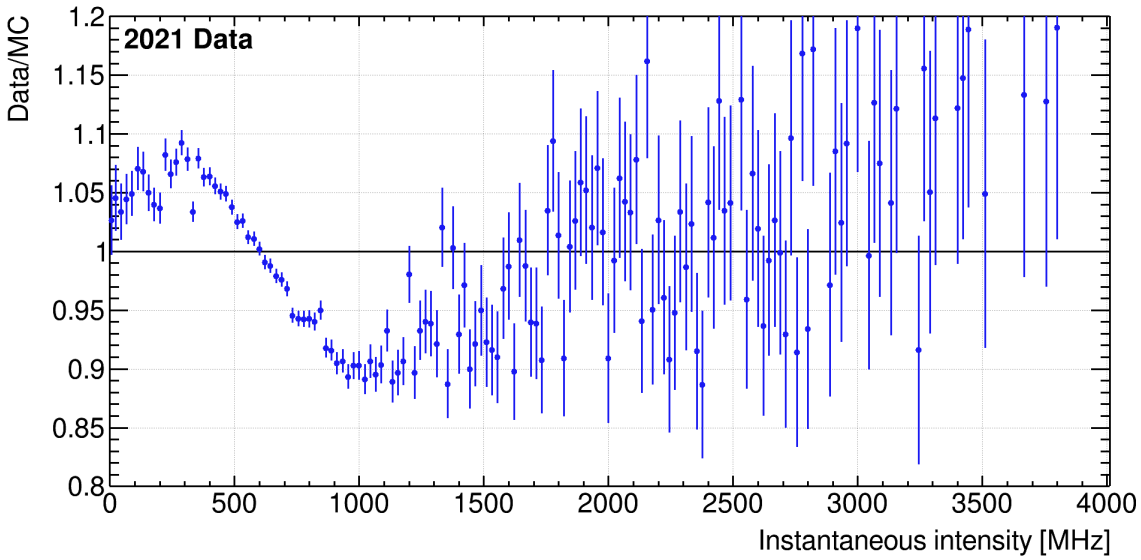

Figure 4.14: Data/MC for the beam intensity using minimum bias data collected in 2021 and MC generated using the new 2021 template produced by using the Bayesian unfolding method.

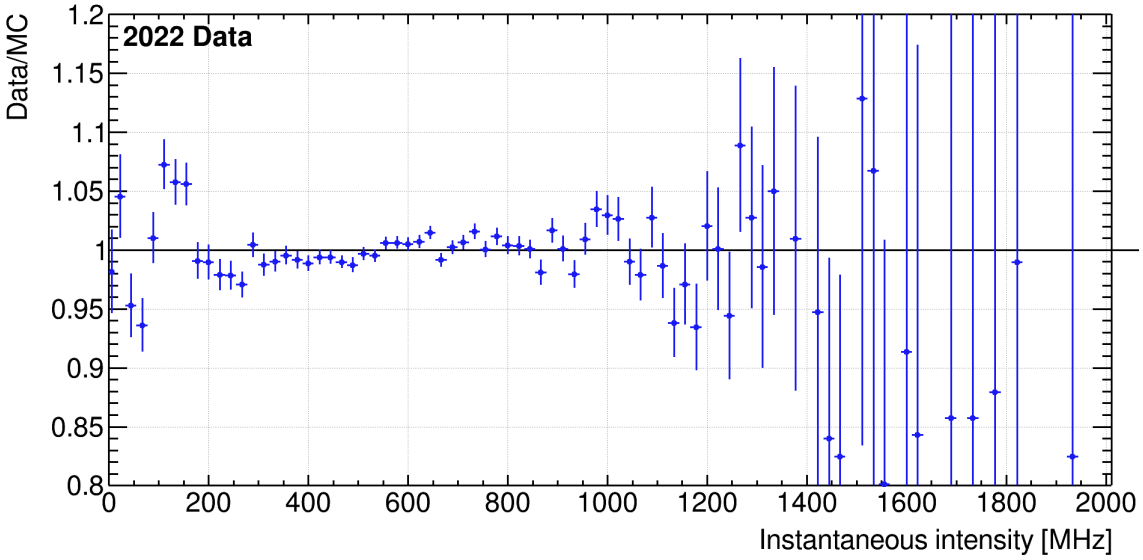

Figure 4.15: Data/MC for the beam intensity using minimum bias data collected in 2022 and MC generated using the new 2022 template produced by using the Bayesian unfolding method. The reduced intensity range compared to the other data-taking years is due to a lack of statistics in the data distribution.

4.6 Stability of the template

Two approaches were investigated to try and quantify the stability of the template created by the unfolding method. Firstly, we can unfold the measured distribution obtained in MC and compare this to the template used in generating said MC. Here the 2018 dataset has been used. Figure 4.16 shows the ratio of the template to the unfolded MC intensities for a new 2018 MC sample. Whilst there are some fluctuations across the intensity range, there is agreement on the level of 4% up to an intensity value of 2.5 GHz. Values larger than this intensity value are contained in the tails of the distribution and thus it is not considered critical to resolve this issue. We also note that this is the same behaviour as in the data/MC ratio shown in Figure 4.13.

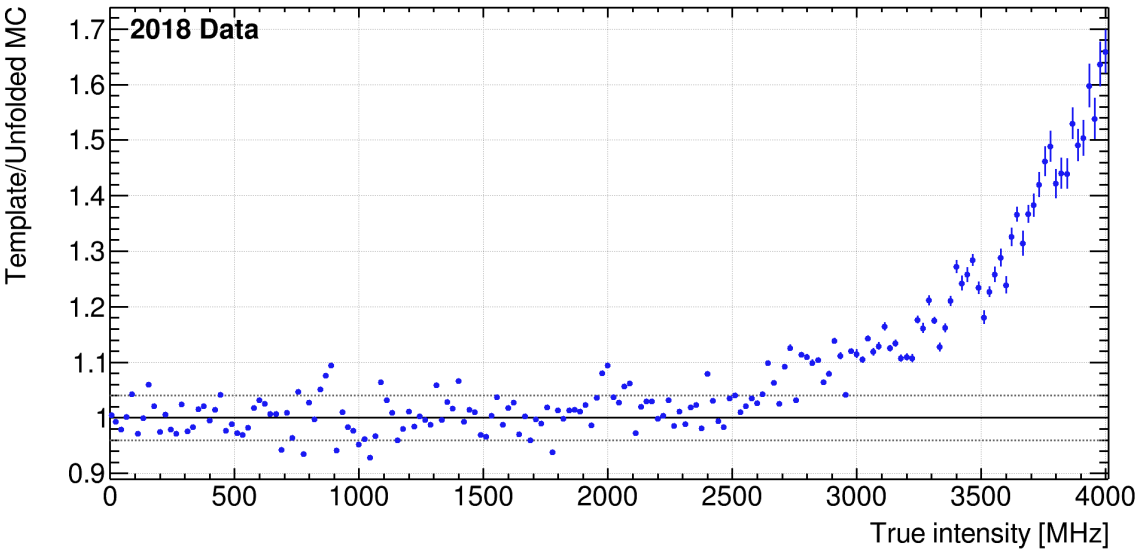

Figure 4.16: Unfolding the measured intensity of MC generated using the 2018 template to obtain the input intensity template. Here we see no more than a 4% discrepancy.

Secondly, an investigation into the effect of unfolding data with a different response matrix was also performed. In generating the new templates, a uniform response matrix was utilised to increase the statistics at higher intensities. However, alternatively, we could have used a beam intensity distribution closer to that seen

in data. Figure 4.17 shows the ratio of templates created by unfolding data with a uniform response matrix and a more data-like response matrix. The sample sizes of the response matrices were chosen to be the same, 200 million events, to remove statistical effects, and the 2018 MC sample used to generate the alternate response matrix was different to that used in testing. Again, we see consistent values across the entire intensity range to the level of 10% and a systematic error should be applied moving forwards to reflect this discrepancy.

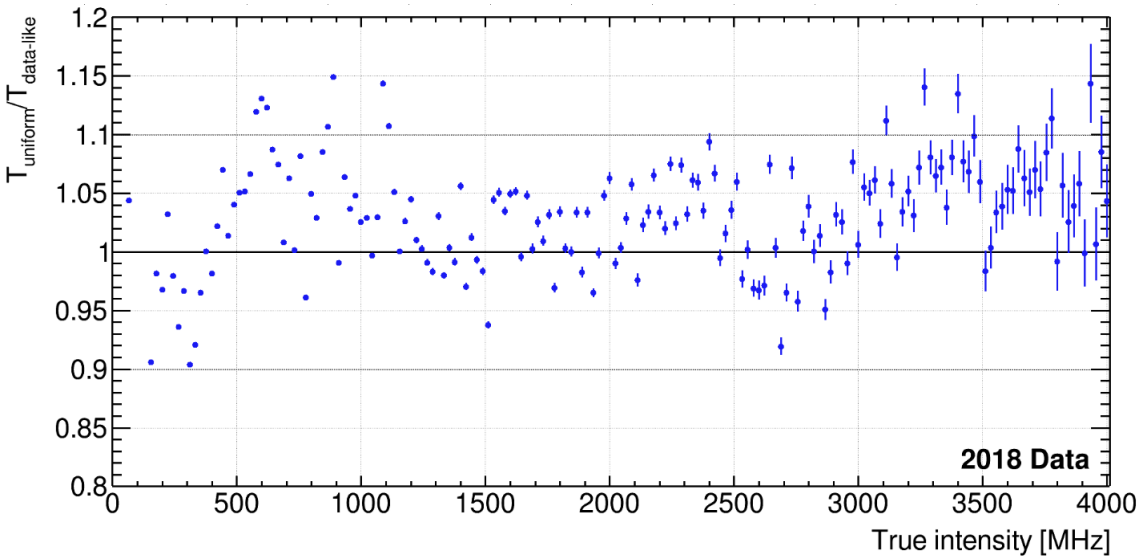

Figure 4.17: Ratio of templates produced from unfolding 2018 control data with a uniform response matrix, T_{uniform}, and a more data-like response matrix, $T_{\text{data-like}}$ We see that the choice of response matrix does not greatly effect the final result and a discrepancy of $\sim 10\%$ is seen.

4.7 Summary

The intensity distribution of Monte-Carlo simulations did not have good agreement with the data collected in 2017. Additionally, this distribution is different for each data taking period and thus also did not agree with the data collected in 2018. Therefore, it was clear that new templates were required. Moreover, it will also be beneficial to automate this procedure such that templates can be produced for data

collected in future years, as well as updating templates if the simulation framework is modified in ways that affect the intensity estimate.

Methods for generating new templates have been discussed in section 4.3 and subsection 4.4.2. Unfolding the measured intensity distribution using the iterative Bayesian algorithm with 20 iterations was found to be the most effective method, and a piece of software was written within the work of this thesis to automate this procedure. Performance of the resulting templates prove to be satisfactory.

Chapter 5

Studies of $K^+ \to \pi^+ \nu\bar{\nu}$ as a function of beam intensity

In this chapter, the study of the $K^+ \to \pi^+ \nu\bar{\nu}$ decay as a function of the NA62 beam intensity is discussed. The main goal of the NA62 experiment is the precise measurement of the branching ratio of the ultra-rare $K^+ \to \pi^+ \nu\bar{\nu}$ decay for which it is vital to collect a large dataset with minimal background contamination. Whilst in principle a higher intensity promotes the collection of more events, in practise the $K^+ \to \pi^+ \nu\bar{\nu}$ signal yield is affected by several effects. Online, hardware components limit the maximum beam intensity that can be sustained by the trigger and data acquisition. Offline, a large proportion of the $K^+ \to \pi^+ \nu\bar{\nu}$ analysis relies on efficiencies that vary with the beam intensity. Therefore, it is crucial to define the optimal value at which to operate NA62 that maximises the efficiency of the analysis procedure and minimises losses due to hard failures.

Encapsulating the efficiency of the analysis and the size of the dataset is the single event sensitivity (SES), defined as the branching ratio required for the observation of a single signal event, discussed further in subsection 5.1.5. This chapter focuses

on the components that contribute to this single event sensitivity measurement, how they vary as a function of beam intensity and any improvements between NA62 run-1 and run-2 at the time of submission.

5.1 Fundamentals of the $K^+ \to \pi^+\nu\bar{\nu}$ analysis

5.1.1 Analysis procedure

When searching for the $K^+ \to \pi^+\nu\bar{\nu}$ decay, one is looking for the incoming kaon decaying into an outgoing pion with some missing energy/momentum. Table 5.1 shows the main background sources to this analysis. With the SM predicting a branching ratio of $\mathcal{B}(K^+ \to \pi^+\nu\bar{\nu}) = (8.60 \pm 0.42) \times 10^{-11}$ [29], it is imperative to reduce the background by kinematically isolating the signal. This can be done by studying the missing mass variable defined as:

$$m^2_{\text{miss}} = (P_K - P_\pi)^2, \tag{5.1}$$

where P_K ,P_π define the 4-momenta of the kaon and pion respectively. Figure 5.1 shows the distribution of m^2_{miss} for the signal and background channels scaled by their branching ratio. A background suppression of the order of 10^{-4} is achieved by defining two kinematic signal regions either side of the $K^+ \to \pi^+\pi^0$ peak, shown by the yellow highlighted regions in the plot. These signal regions are defined in the m^2_{miss} ranges of (0.000–0.010) GeV^2/c^4, signal region 1, and (0.026–0.068) GeV^2/c^4, signal region 2. In addition to the missing mass, the signal regions are further constrained by the momentum of the outgoing pion, p_{π^+}. For NA62 run-1 analysis this is defined to be between 15 and 35 GeV/c to match the design of the RICH and photon veto systems. However, for NA62 run-2, signal region 2 has been extended to 45 GeV/c due to improvements in the offline analysis. A two dimensional plot of the signal regions in $m^2_{\text{miss}} - p_{\pi^+}$ space is shown in Figure 5.2.

Table 5.1: Main backgrounds to the $K^+ \to \pi^+\nu\bar{\nu}$ analysis

Decay	Branching Ratio	Explanation
$K^+ \to \pi^+\pi^0$	0.2067 ± 0.0008	π^0 is undetected
$K^+ \to \pi^+\pi^-\pi^+$	0.0558 ± 0.0002	$\pi^+\pi^-$ are undetected
$K^+ \to \mu^+\nu_\mu$	0.6356 ± 0.0011	μ^+ mistaken for π^+

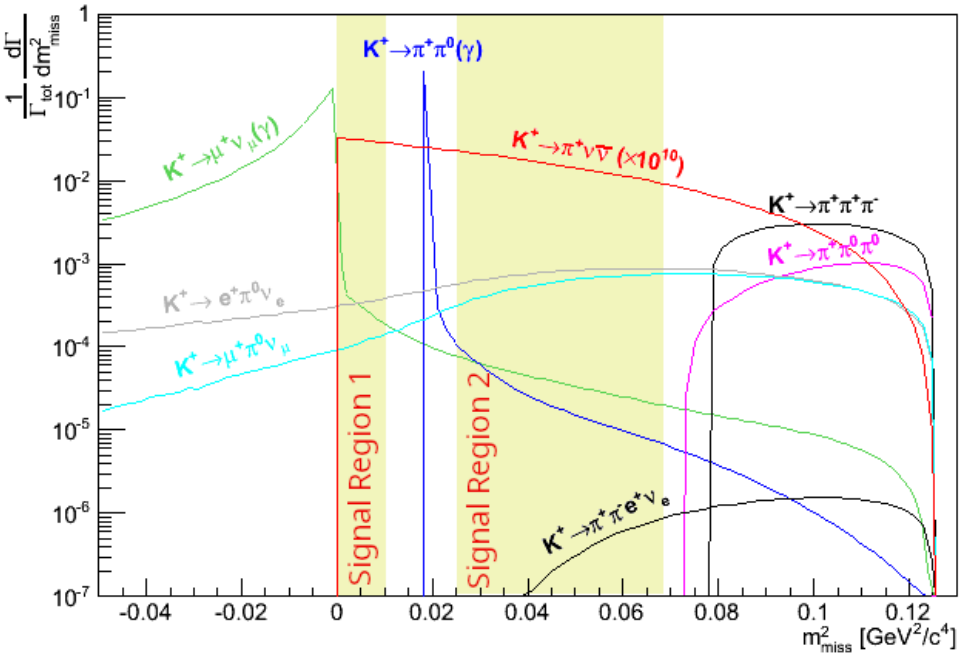

Figure 5.1: Distribution of m^2_{miss} for the signal and background channels scaled by their branching ratio. Common backgrounds from K^+ decays are shown. The signal regions, shown in yellow, are defined to be the missing mass regions: (0.000–0.010) GeV$^2/c^4$ and (0.026–0.068) GeV$^2/c^4$. Plot modified from [51].

The definition of these signal regions alone is not sufficient to reduce the background to the required level and hence further selection is required. Additional background suppression is achieved through particle identification (PID), mostly distinguishing π^+ from μ^+ using a combination of the RICH and MUV detectors, and the photon veto system. Multiplicity cuts reject events with additional charged particles indicating the presence of multi-body decays or photon conversion occurring inside the detector. The full $K^+ \to \pi^+\nu\bar{\nu}$ selection is briefly discussed in subsection 5.1.3 whilst an in depth description is provided in [12, 97, 98]. The analysis of the NA62 run-2 data remains blinded until the selection has been finalised to avoid biasing the results.

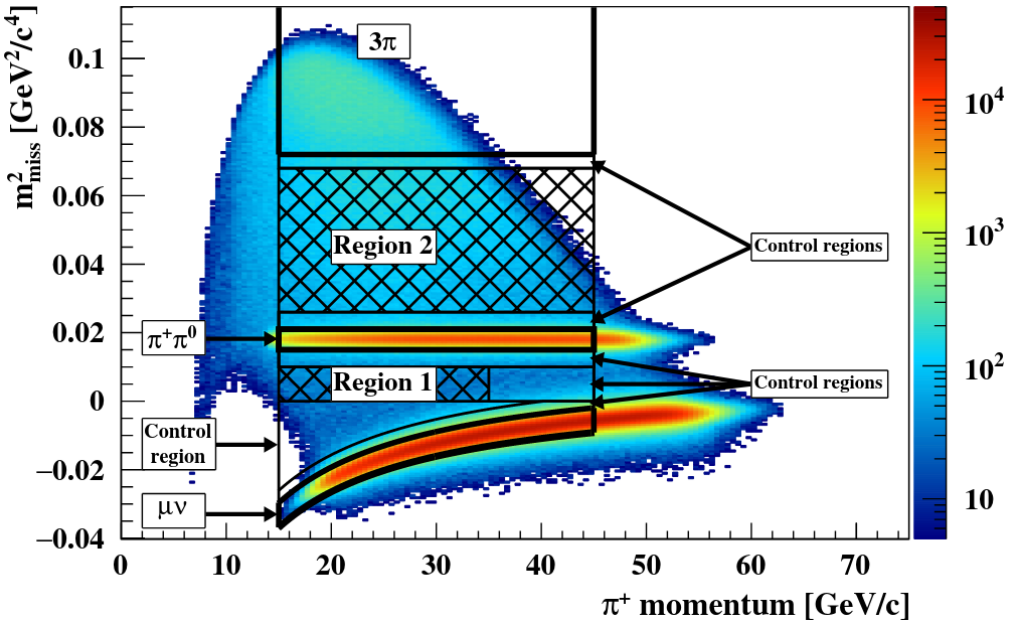

Figure 5.2: $K^+ \to \pi^+\nu\bar{\nu}$ signal regions defined by the squared missing mass and momentum of the positive pions. Here the $K^+ \to \pi^+\nu\bar{\nu}$ selection has been applied to minimum bias data with the exception of the π^+ identification and photon rejection. The hatched areas show the signal regions with the $K^+ \to \pi^+\pi^-\pi^+$ (labelled 3π), $K^+ \to \pi^+\pi^0$, and $K^+ \to \mu^+\nu_\mu$ background regions shown by solid contours [12].

5.1.2 Data & MC samples

This thesis focuses on the data collected in 2021 at the start of NA62 run-2. Comparisons to NA62 run-1 data, collected between 2016 and 2018, are made throughout this chapter with an emphasis on the 2018 dataset analysed and published in [12].

Data collected with a number of trigger lines are used for the $K^+ \to \pi^+\nu\bar{\nu}$ analysis. A minimum bias trigger, using information from the NA48-CHOD detector, is used for the collection of $K^+ \to \pi^+\pi^0$ normalisation events in NA62 run-1. For NA62 run-2, $K^+ \to \pi^+\pi^0$ events are collected with a Non-μ trigger that uses information from the RICH, CHOD and MUV detectors. Normalisation events collected with the Non-μ trigger are a subsample of those selected by the PNN trigger used for the reconstruction of the signal, and thus allow for cancellations in the evaluation of the single event sensitivity. Additionally, a minimum bias trigger is also used for the collection of a control sample of $K^+ \to \mu^+\nu_\mu$ events for the study of the random veto

efficiency discussed in section 5.2. The definition of the minimum bias trigger for NA62 run-1 and run-2 is described further in section 5.3. For each of these trigger lines, a downscaling factor is applied to limit the number of less interesting events being saved to disk; a downscaling factor of N indicates that only one in N events are stored. The PNN trigger line has a downscaling factor of 1 whilst the minimum bias trigger has a downscaling of 400.

MC samples based on each data-taking year using the templates created in chapter 4 are also used. Whilst the final estimate is fully data-driven, overlaid MC is essential in estimating the upstream background and kinematic tails entering into the signal regions. Furthermore, the acceptance of the selection criteria can only be measured on MC.

5.1.3 $K^+ \to \pi^+\nu\bar{\nu}$ selection

The $K^+ \to \pi^+\nu\bar{\nu}$ selection can be categorised in the following way:

Parent kaon

The definition of the parent kaon is a signal in at least five sectors of the KTAG forming a candidate within 2 ns of a downstream particle. Additionally, a beam track in the GTK in time with this KTAG candidate and also associated with the downstream track in the STRAW is required. Association between the KTAG, GTK and STRAW relies on a discriminant based on the time difference between the KTAG and GTK candidates and also the closest distance of approach (CDA) of the downstream particle to the beam track, with the largest value of this discriminant being identified as the parent kaon. To protect against accidental association of a pileup-track in the GTK with the KTAG candidate, a cut on the minimum allowed value of this likelihood discriminator is applied. Moreover, no more than five GTK tracks are allowed.

Downstream charged particle

The downstream charged particle selection is characterised by a track reconstructed in the STRAW spectrometer matching signals both spatially and temporally in both of the hodoscopes, the LKr and in the RICH. The track must be positively charged and any events including a negative track are rejected to remove $K^+ \to \pi^+\pi^-\pi^+$ and $K^+ \to \pi^+\pi^- e^+\nu$ decays. The time of the track is calculated as a weighted mean of the signal time in the STRAW, NA48-CHOD and RICH detectors weighted by their respective time resolutions. Additionally, events with no more than two reconstructed tracks are allowed, and the track closest in time to the reference trigger time is selected as belonging to the $K^+ \to \pi^+\nu\bar{\nu}$ event.

By extrapolating the STRAW track to the downstream detectors, one can associate signals in the NA48-CHOD, CHOD, LKr and RICH to the downstream particle. Associations of the track to the NA48-CHOD and CHOD candidates are made using discriminants based on time and spatial coordinates. An LKr cluster is associated to the charged particle if the distance between the cluster and the expected particle impact point at the LKr front plane is less than 100 mm. A RICH ring is associated to the track if the centre of the ring lies within the expected impact point of the track at the front plane of the RICH.

Kaon decay

The vertex of the decay is defined as the point in space with the CDA between the parent kaon and the downstream track; the z position of the vertex must be in the fiducial volume. The definition of the fiducial decay volume for this analysis is momentum-dependent to reduce backgrounds from the $K^+ \to \pi^+\pi^0$ and $K^+ \to \pi^+\pi^- e^+\nu$ decays. A boosted decision tree (BDT) with nine input variables, the spatial coordinates and direction of the STRAW track along with the spatial

coordinates of the decay vertex, is used to veto early upstream decays. A cut based on the output of the BDT provides the same background rejection as a typical cut-based approach whilst improving the signal acceptance by 8% [12]. No signal in the CHANTI detector is allowed within 3 ns of the downstream track time to reduce background from inelastic scattering in GTK3.

Particle identification

Particle identification of the downstream track is achieved through a combination of the calorimeters and the RICH; additionally no signal in MUV3 must be present within 7 ns of the π^+ time. A BDT is used with the calorimetric information of the downstream particle including the shape of any clusters and the energy shared between the LKr, MUV1 and MUV2. As for the RICH, two approaches are utilised. Firstly, a likelihood is created from comparing the observed hit positions to the expected ring radii assuming each mass hypothesis using the expected impact point of the pion as the centre of the RICH ring. Secondly, the centre and radius of the observed ring are calculated by a χ^2 fit and the downstream particle mass is derived from its momentum. Cuts on the largest non π^+ likelihood and on the measured mass are applied to separate pions from muons.

Photon and multiplicity rejection

The signal selection requires that there are no in-time photons with the downstream particle and additionally no extra charged particles must be present. The LAV, IRC, SAC and LKr are used to veto events with photons in the final state. As for the additional charged particles, association of in-time signals in the NA48-CHOD, CHOD and LKr not associated with the π^+ track are used. Moreover, signals in the MUV0 and HASC detectors are also used to reject events with extra particles

in the final state. For more information on the photon and multiplicity rejection criteria, see section 5.2.

Kinematic Region

The $K^+ \to \pi^+\nu\bar{\nu}$ signal regions are defined in the $m^2_{\text{miss}} - p_{\pi^+}$ space and are shown in Figure 5.2. To calculate the squared missing mass, the 3-momenta measured by the GTK and STRAW spectrometers are used assuming the kaon and pion mass hypotheses. Additionally, further constraints can be applied by supplementing this information with the nominal beam momentum or the downstream particle momentum as measured by the RICH. Events originating from $K^+ \to \pi^+\pi^0$ accumulate around the π^0 invariant mass peak whilst the $K^+ \to \mu^+\nu_\mu$ events have negative missing mass due to the incorrectly assigned π^+ mass in the m^2_{miss} computation. To reject these backgrounds, two signal regions are defined. Region 1, $0.000 < m^2_{\text{miss}} < 0.010\,\text{GeV}^2/c^4$ with the pion momenta between 15 and 35 GeV/c, and region 2, $0.026 < m^2_{\text{miss}} < 0.068\,\text{GeV}^2/c^4$ with pion momenta between 15 and 45 GeV/c. The signal regions are masked (blind) until the analysis has been finalised to avoid bias.

5.1.4 $K^+ \to \pi^+\pi^0$ and $K^+ \to \mu^+\nu_\mu$ selections

In the studies involved in this thesis, control samples of $K^+ \to \pi^+\pi^0$ and $K^+ \to \mu^+\nu_\mu$ decays are required. The selections of these decays should be as close to the $K^+ \to \pi^+\nu\bar{\nu}$ selection as possible such that these control samples are representative of the signal sample.

For the $K^+ \to \pi^+\pi^0$ decay, a kaon matched to a downstream pion is still required, however the photon and multiplicity rejection cuts are now removed with

the exception of still vetoing a multi-track vertex. This is to allow for the π^0 to decay to photons. Events are required to have a missing mass in the range of $0.010 < m^2_{\text{miss}} < 0.026\,\text{GeV}^2/c^4$ with $15 < p_{\pi^+} < 45\,\text{GeV}/c$ and are therefore situated in the $K^+ \to \pi^+\pi^0$ region between signal region 1 and signal region 2, see Figure 5.2.

Similarly, the $K^+ \to \mu^+\nu_\mu$ selection also requires a kaon matched to a downstream particle, however the PID conditions are inverted such that a muon is selected instead of a pion. Additionally, a signal is required to be found in the muon veto detectors and the photon and multiplicity cuts are also applied. The missing mass squared variable under the hypothesis of the muon mass is required in the range $-0.010 < m^2_{\text{miss}} < 0.010\,\text{GeV}^2/c^4$.

5.1.5 Single event sensitivity

The single event sensitivity (SES), $\mathcal{B}_{SES}$, is defined as the branching ratio corresponding to the observation of a single signal event. This is inherently linked to the efficiency of the analysis and the size of the dataset available. The SES is then defined by:

$$\mathcal{B}_{SES} = \frac{1}{N_k\ \epsilon_{\pi\nu\nu}} \tag{5.2}$$

with N_k corresponding to the number of effective kaon decays (i.e the size of the dataset) and $\epsilon_{\pi\nu\nu}$ describing the efficiency of the $K^+ \to \pi^+\nu\bar{\nu}$ analysis.

A normalisation channel is used to calculate the number of kaon decays which, to minimise the uncertainty in the final result, should satisfy the following criteria:

- The branching ratio should be precisely known.
- The normalisation selection should match the signal selection as closely as possible, see subsections 5.1.3 and 5.1.4.

- The selected sample should be large such that the statistical uncertainty is minimised.

- The selected sample should also be, as much as possible, free from background contamination.

The $K^+ \to \pi^+\pi^0$ decay matches these criteria well and the event selection is outlined in subsection 5.1.4. Unfortunately, the PNN trigger line[7] can not be used to collect $K^+ \to \pi^+\pi^0$ events as it has been designed to veto photons in the final state. Thus for NA62 run-1 the minimum bias (CTRL) trigger is used, and for NA62 run-2 the Non-μ trigger line is used such that some of the trigger conditions between the normalisation and signal collection are in common.

The number of kaons can be calculated using:

$$N_k = \frac{N_{\pi\pi}\ D}{A_{\pi\pi}\ \mathcal{B}_{\pi\pi}\ \epsilon^{\text{trig}}_{\pi\pi}}, \tag{5.3}$$

where $N_{\pi\pi}$ is the number of $K^+ \to \pi^+\pi^0$ events collected with an acceptance of $A_{\pi\pi}$ using a trigger line with efficiency, $\epsilon^{\text{trig}}_{\pi\pi}$, and a Downscaling factor, D. The branching ratio of the $K^+ \to \pi^+\pi^0$ decay, $\mathcal{B}_{\pi\pi}$ also contributes to this calculation.

The efficiency of the $K^+ \to \pi^+\nu\bar{\nu}$ decay is defined as the product of the PNN trigger efficiency, $\epsilon^{\text{trig}}_{\pi\nu\nu}$, the acceptance, $A_{\pi\nu\nu}$, and the random veto efficiency, ϵ_{RV}:

$$\epsilon_{\pi\nu\nu} = A_{\pi\nu\nu}\ \epsilon^{\text{trig}}_{\pi\nu\nu}\ \epsilon_{\text{RV}}. \tag{5.4}$$

Where $(1 - \epsilon_{\text{RV}})$ is defined as the probability for a signal event to be rejected due to accidental activity in the detector. Combining Equations 5.2, 5.3 and 5.4 and

[7]The definition of all the trigger lines is provided in section 2.3 whilst those discussed in this section are further discussed in section 5.3.

grouping similar terms we find:

$$\mathcal{B}_{SES} = \mathcal{B}_{\pi\pi}\frac{A_{\pi\pi}}{A_{\pi\nu\nu}}\frac{1}{N_{\pi\pi}\ D}\frac{\epsilon^{\text{trig}}_{\pi\pi}}{\epsilon^{\text{trig}}_{\pi\nu\nu}}\frac{1}{\epsilon_{RV}}. \tag{5.5}$$

Additionally, as the majority of these components depend on the momentum of the π^+ and on the instantaneous beam intensity, one can write:

$$\mathcal{B}_{SES} = \mathcal{B}_{\pi\pi}\sum_{p_\pi}\sum_{I}\frac{A_{\pi\pi}(p_\pi, I)}{A_{\pi\nu\bar{\nu}}(p_\pi, I)}\frac{1}{DN_{\pi\pi}(p_\pi, I)}\frac{\epsilon^{\text{trig}}_{\pi\pi}(p_\pi, I)}{\epsilon^{\text{trig}}_{\pi\nu\bar{\nu}}(p_\pi, I)}\frac{1}{\epsilon_{RV}(p_\pi, I)}. \tag{5.6}$$

With the single event sensitivity defined, one can now calculate the expected number of signal events, $N^{\text{exp}}_{\pi\nu\nu}$, given the standard model branching ratio, $\mathcal{B}^{SM}_{\pi\nu\nu}$:

$$N^{\text{exp}}_{\pi\nu\nu} = \frac{\mathcal{B}^{\text{SM}}_{\pi\nu\nu}}{\mathcal{B}_{SES}}. \tag{5.7}$$

Whilst the signal regions remain blinded as the analysis is ongoing, one can estimate the current status of the analysis and make adjustments accordingly.

5.1.6 Summary of NA62 run-1 results

With the data collected in NA62 run-1 (2016-2018), a total of 20 events were observed with an expected background of 7.0 events. Using a background only hypothesis test, a signal significance of 3.4σ is achieved [12]. A single event sensitivity of $(0.839 \pm 0.054) \times 10^{-11}$ is calculated corresponding to 10.0 SM $K^+ \to \pi^+\nu\bar{\nu}$ events under the assumption that the Standard Model branching ratio of the $K^+ \to \pi^+\nu\bar{\nu}$ decay is $(8.4 \pm 1.0) \times 10^{-11}$ [8]. The measured branching ratio is reported as $\mathcal{B}(K^+ \to \pi^+\nu\bar{\nu}) = (10.6^{+4.0}_{-3.4}|_{\text{stat}} \pm 0.9_{\text{syst}}) \times 10^{-11}$ at a 68% confidence level,

[8] We note that the Standard Model branching ratio has been calculated to an improved precision, $\mathcal{B}(K^+ \to \pi^+\nu\bar{\nu}) = (8.60 \pm 0.42) \times 10^{-11}$ [29], since the NA62 analysis of this dataset and publication of this result [12].

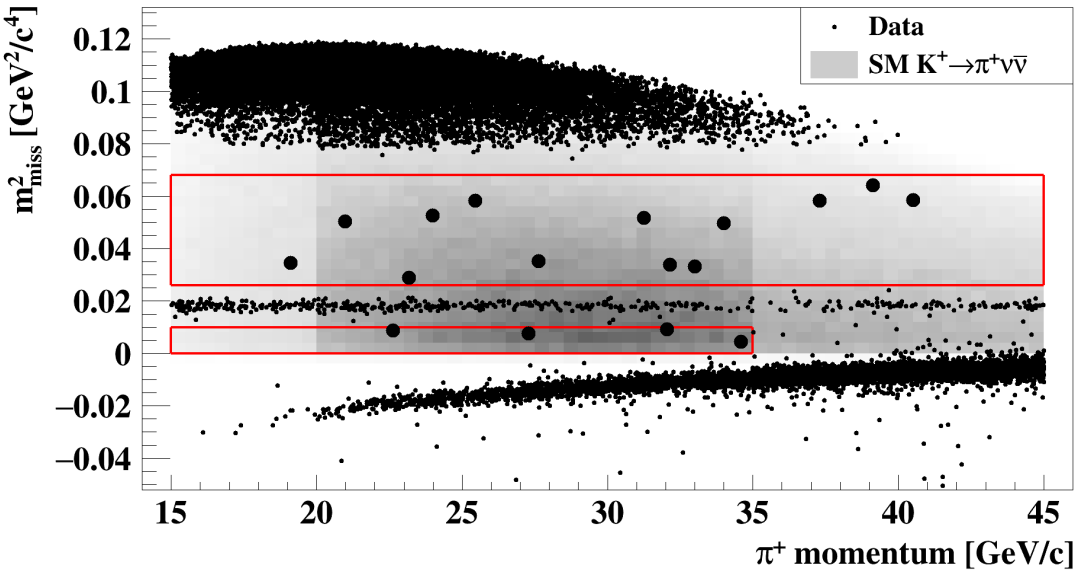

Figure 5.3: Unblinded signal regions (shown by the red boxes) for 2018 data. We see the observation of 17 $K^+ \to \pi^+\nu\bar{\nu}$ events [12].

consistent with the SM prediction within 1σ. A full description of the 2016 and 2017 analyses can be found in [97, 98] respectively, whilst the 2018 dataset (shown in Figure 5.3) and the combined NA62 run-1 results are shown in [12].

5.2 Random veto

Accidental activity in the NA62 detector can cause a signal event to be rejected, and this is known as random veto. As the instantaneous beam intensity increases there is more accidental activity and thus a larger probability of a signal event being rejected. This section aims to quantify the effect of the random veto as a function of the beam intensity and to highlight areas in which this might be reduced. The random veto is independent of the momentum of the π^+ due to its origin.

Several detectors contribute to independent sources of random veto in the single event sensitivity calculation. For detector conditions used in both the $K^+ \to \pi^+\nu\bar{\nu}$ and $K^+ \to \pi^+\pi^0$ selections like the GTK, CHANTI, STRAW and MUV3, these effects will cancel out.

The remaining random veto contributions can be separated into two components, photon vetoes and multiplicity vetoes. As photon and multiplicity rejection cuts are not applied to $K^+ \to \pi^+\pi^0$ events they contribute to ϵ_{RV} in Equation 5.6. To measure each veto condition, a sample of $K^+ \to \mu^+\nu_\mu$ events is selected from minimum bias data. The $K^+ \to \mu^+\nu_\mu$ decay is chosen for the similarities to the $K^+ \to \pi^+\nu\bar{\nu}$ signature; the selection of both decays is identical bar the inverted PID conditions (a μ^+ is required instead of a π^+) and the kinematic regions selected.

5.2.1 Photon vetoes

The detectors contributing to the photon veto system are the LAV, IRC, SAC and LKr. Low energy photons are emitted at a large angle and thus are expected to be detected in the LAV. The event is rejected if there is a signal within 3 ns of the trigger time in a LAV station downstream of the decay vertex; this ensures that activity in stations that could not have originated from the candidate event is not taken into account.

The event is rejected if a candidate photon is found in the LKr at least 100 mm away from the pion impact point and within an energy-dependent time window. Improvements to the LKr reconstruction algorithm, not carried out by the author, has allowed for a significant relaxation in the veto criteria, particularly at high energies, compared to the NA62 run-1 analysis. Moreover, further relaxation for clusters between 2.5 GeV and 15 GeV have been suggested and implemented by the author. The modification of the veto criteria can be seen in Figure 5.4 comparing the solid grey line to the dotted black line.

The IRC and SAC detect high energy photons emitted at small polar angles down to 0° that would otherwise escape down the beam pipe. Signals are read out using TEL62 and CREAM readout boards. To achieve the maximal rejection power,

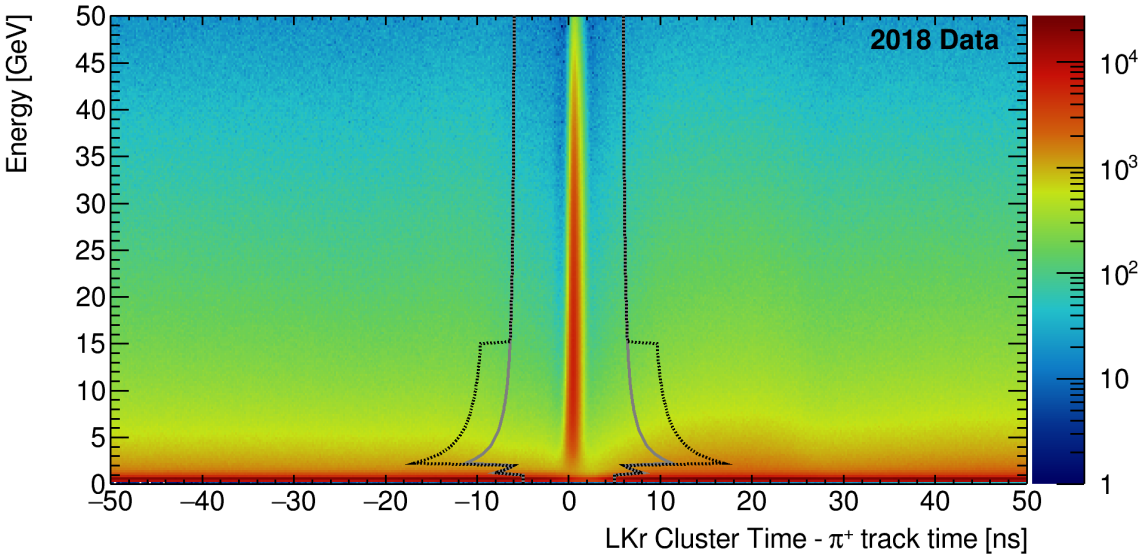

Figure 5.4: Energy of clusters found in the LKr not associated with the π^+ track as a function of their relative time difference measured using $K^+ \to \mu^+\nu_\mu$ on 2018 minimum bias data. In prior analyses, the cut at the highest energies was set to 70σ whilst this was reduced to 10σ after improvements to the reconstruction, see the black line. A further reduction for energies between 5 and 15 GeV was suggested by the author to improve the status of the random veto and consequently became the NA62 run-2 cut, see grey line.

veto criteria are optimised for both types of readout and used in conjunction with one another. Any signal read by the TEL62 boards within 7 ns of the trigger time will lead to the rejection of the candidate signal event. For the CREAM readout, this veto condition is relaxed to 5 ns and a minimum energy deposit of 1 GeV is additionally required.

5.2.2 Multiplicity vetoes

The second category of random activity impacting the $K^+ \to \pi^+\nu\bar{\nu}$ measurement is related to track multiplicity inside the event. This could either be due to photon conversion to charged particles or multi-track decays in which the tracks have only partially been reconstructed in the STRAW. For this category, the spatial association of in-time signals in the NA48-CHOD, CHOD and LKr not associated with the π^+ track are exploited. Additionally, looking for activity in the MUV0 and HASC

detectors also contribute to veto such undesired events. For multi-track final states with tracks partially reconstructed in the STRAW, an algorithm is used to combine hits inside each view into potential clusters before being associated between views into a segment. Segments can then be associated between stations when hits may be missing. If one of these partially reconstructed tracks is in-time and within 100 mm of the candidate signal track then the event is vetoed.

5.2.3 Status for the 2021 analysis

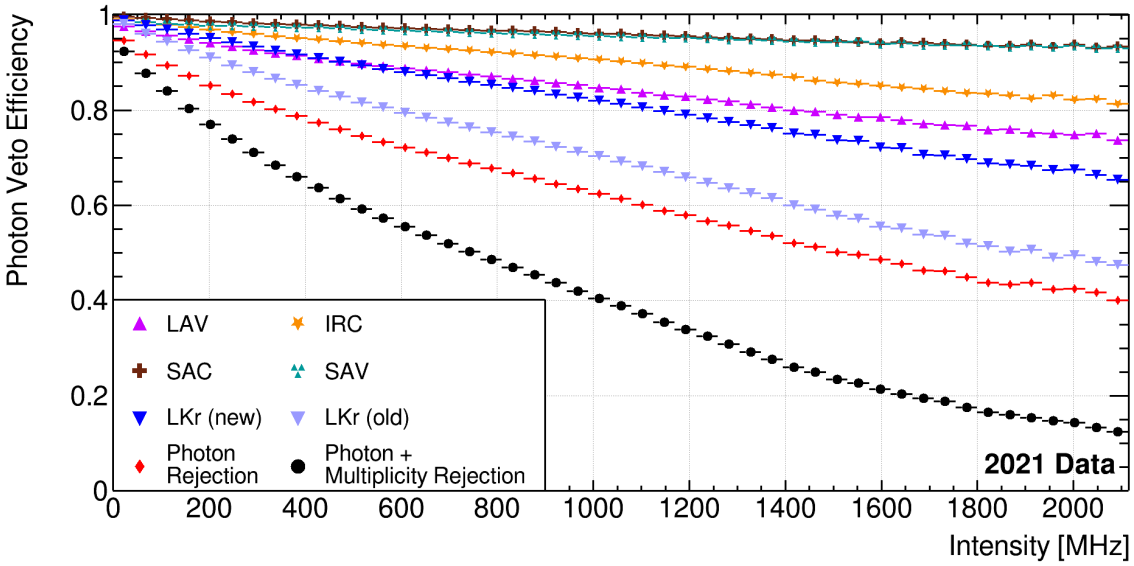

Figure 5.5: Efficiency of the random veto based on the criteria to reject photons as measured on 2021 minimum bias data.

Whilst the 2021 analysis has not yet been finalised, this section aims to describe the current improvements to the $K^+ \to \pi^+\nu\bar{\nu}$ analysis compared to the previous NA62 analysis with data collected between 2016-2018.

As mentioned in subsection 5.2.1, improvements to the LKr reconstruction have allowed for a significant reduction in the veto cut criteria for photons within the LKr. This is shown in Figure 5.4 where the energy of an LKr cluster is plotted against its time in reference to the trigger time. We see the physics peak centred at a time of 0 ns whilst the cut seems quite large in comparison. For the NA62 run-1 analysis,

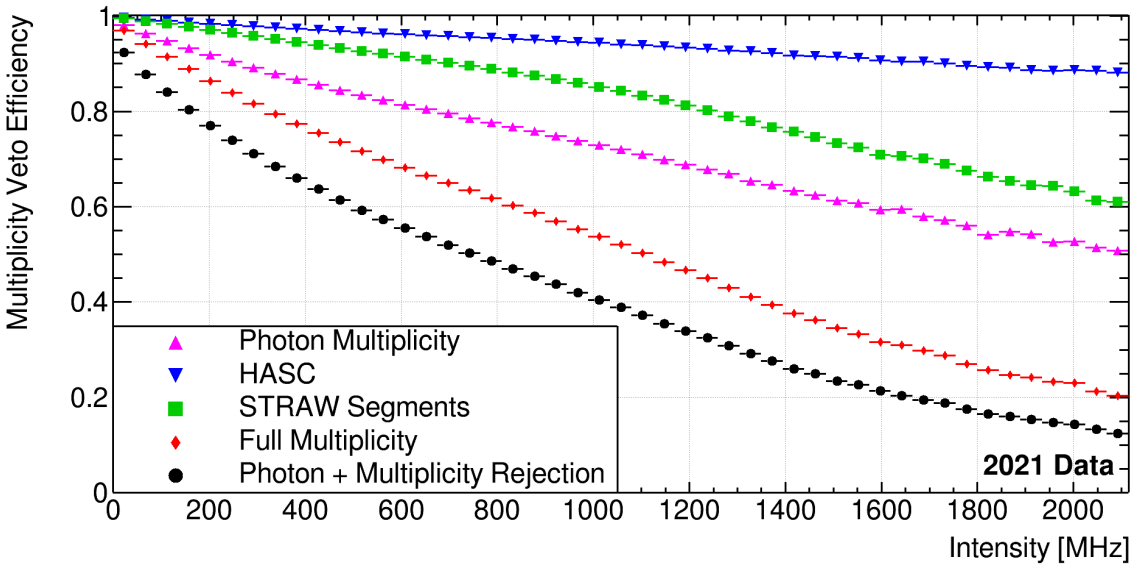

Figure 5.6: Efficiency of the random veto based on the criteria to reject additional tracks/events as measured on 2021 minimum bias data.

this cut was set to 70σ for the largest energies ($E > 15\,\text{GeV}$) but relaxed to 10σ after the improved reconstruction. By suggestion of the author of this thesis, the cut was reduced further for lower energy photons ($2\,\text{GeV} < E \leq 15\,\text{GeV}$), compare the black line to the grey line in Figure 5.4, whilst ensuring that the background contamination remains under control.

The random veto measured with 2021 data is shown in Figure 5.5 for the photon vetoes and Figure 5.6 for the multiplicity criteria. Here we see the improvements to the LKr veto by comparing the downward triangles in Figure 5.5 with the old (new) criteria in light (dark) blue. Additionally, we see in general that the photon vetoes outperform the multiplicity criteria and if we wish to decrease the impact of the random veto such that NA62 can operate at a higher nominal intensity, this is where our efforts should be focused. At the time of submission, work on implementing a BDT to replace the multiplicity criteria is showing promise in improving the status of the random veto.

As the nominal intensity has increased between the 2018 and 2021 data taking periods, one might predict that the overall random veto efficiency would decrease. As

reported in [12], the random veto efficiency for data taken in 2018 was $\epsilon_{RV} = 66 \pm 1\%$. Currently the 2021 random veto is measured with an efficiency of $\epsilon_{RV} = 63 \pm 1\%$ with further improvements planned such as the implementation of a BDT for the multiplicity criteria.

5.3 Trigger efficiency

An introduction into the trigger for NA62 has been provided in section 2.3. The conditions and performances relevant to the $K^+ \to \pi^+\nu\bar{\nu}$ measurement are discussed further in the following section.

Data used for the $K^+ \to \pi^+\nu\bar{\nu}$ analysis are collected with several triggers; the PNN trigger line is used to select signal events, the minimum bias (Non-μ) trigger line is used to collect the normalisation channel ($K^+ \to \pi^+\pi^0$) in NA62 run-1 (NA62 run-2), and a minimum bias trigger using the RICH and CHOD detectors is used to collect a control sample of $K^+ \to \mu^+\nu_\mu$ events for NA62 run-2. During the NA62 run-1 data collection, the minimum bias trigger was defined as a signal in the NA48-CHOD indicating the presence of a charged track. For NA62 run-2, the minimum bias trigger has been updated such that it is now formed of a signal in the CHOD and RICH detectors. The change in the minimum bias trigger allows for an unbiased subsample of the PNN triggered data to be collected with the added benefit of the improved time resolution from using the RICH primitive as a reference time. Both minimum bias triggers are downscaled by a factor of 400. The NA48-CHOD trigger still exists for the NA62 run-2 data collection period, albeit with greater downscaling, and is used in measuring the efficiency of the trigger.

The PNN trigger line at L0 is defined as follows: a signal in the RICH is used as the reference time and a time window of ± 6.25 ns is opened. Inside this time window

there must be at least one signal in the CHOD, although not in opposite quadrants to suppress multi-body decays such as $K^+ \to \pi^+\pi^-\pi^+$. No in-time signal must be found in the MUV3 to suppress $K^+ \to \mu^+\nu_\mu$ decays. In the LKr, no single cluster must exceed 30 GeV (NA62 run-1) or 40 GeV (NA62 run-2) or additionally the sum of multiple clusters, if present, must not exceed 5 GeV to suppress $K^+ \to \pi^+\pi^0$, $\pi^0 \to \gamma\gamma$ decays. At L1, a 5 sector coincidence in the KTAG is required with at least one positively charged STRAW track forming a vertex with the beam prior to the first STRAW station and with momenta less than 50 GeV/c. Additionally, there must not be more than two signals in the LAV stations excluding LAV1 and LAV12 within 6 ns of the trigger reference time.

As for the normalisation events, the minimum bias trigger for NA62 run-1 has already been discussed. The Non-μ trigger line used in NA62 run-2 requires a signal in the CHOD and RICH within a 6.25 ns time window and no signal inside any MUV3 tiles (excluding the eight closest to the beam). At L1, a positive identification of a kaon is required (signal in at least 5 sectors), along with a positively charged track originating inside the fiducial decay volume with momentum less than 65 GeV/c. A downscaling factor of 200 is applied to this trigger line. The trigger conditions shared with the PNN trigger line will cancel in the single event sensitivity calculation and thus reduces the uncertainty propagated to the final result.

The L0 conditions are studied individually using data collected with the NA48-CHOD minimum bias trigger. As for the L1 algorithms, these need to be evaluated in order of processing according to the specific trigger line. For each trigger line, a fraction (1%) of events (called *autopass*) satisfying the L0 trigger conditions is written to disk regardless of the L1 trigger algorithms outcome. *autopass* events are used to measure the L1 trigger efficiency. As the trigger conditions at L1 are independent from those applied at L0, the total trigger efficiency for a given trigger line is the product of the L0 and L1 efficiencies.

5.3.1 L0

The L0 trigger primitives are stored in data with a timing precision of 100 ps. Minimum bias events, requiring only a hit in the NA48-CHOD, are used as a control sample to measure the efficiency of L0 trigger primitives. Control samples of $K^+ \to \mu^+\nu_\mu$ and $K^+ \to \pi^+\pi^0$ are selected.

Figure 5.7 shows the efficiency of the L0 trigger conditions contributing to the PNN trigger line measured on NA48-CHOD triggered events from 2021 data compared to their emulated values on the same data set; the LKr condition shall be discussed separately. The emulated trigger efficiency is a software-based simulation of the hardware trigger and is crucial for calibrating the trigger system, understanding its performance, and correcting for any discrepancies between the hardware and software systems. All L0 trigger conditions are highly efficient with the largest contribution to the inefficiency arising from the $\overline{\text{QX}}$ condition, in which we require no signals in opposite quadrants of the CHOD detector. As the intensity is increased, additional events are more likely to be occurring in the same time window as a signal event, and thus the $\overline{\text{QX}}$ condition is less likely to be met. However, it is still highly efficient, $> 99\%$ at an intensity of 1 GHz. The emulated values on this same data set are shown to be highly accurate and within 0.5% across the entire intensity range.

The efficiency of the LKr L0 depends on the energy deposited in the LKr and hence is non-trivial to measure. A sample of $K^+ \to \pi^+\pi^0$ events are used with both photons from the $\pi^0 \to \gamma\gamma$ detected in the LAV. With this requirement, the sample contains events with more energetic π^+ than in the expected distribution from a sample of $K^+ \to \pi^+\nu\bar{\nu}$ events. Therefore, we require a conversion procedure to transform the LKr efficiency as a function of energy into an efficiency as a function of momentum. A sample of $K^+ \to \pi^+\pi^-\pi^+$ events are used to determine the relationship between the momentum of the π^+ and the energy it deposits in the

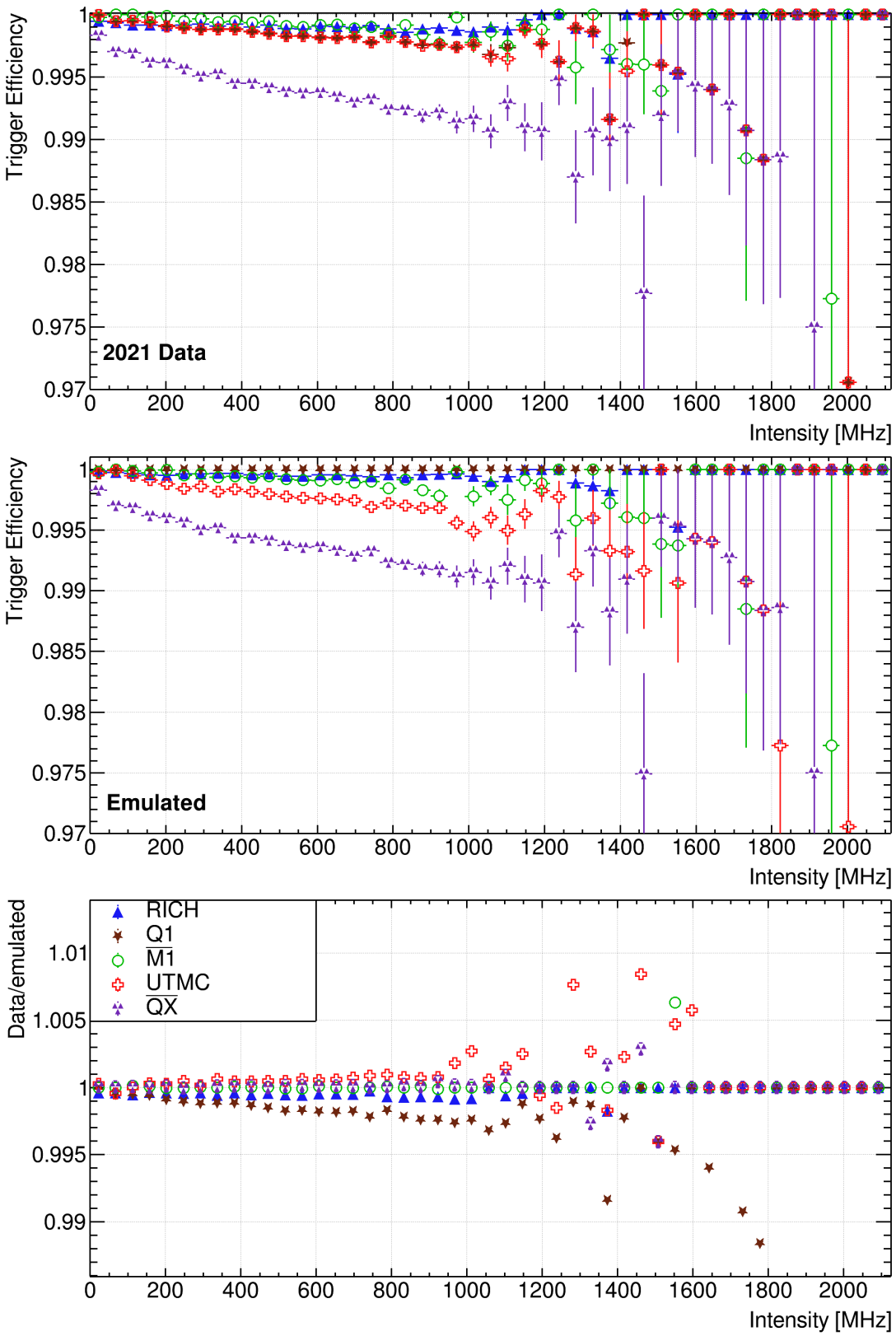

Figure 5.7: Efficiencies of the L0 trigger conditions as a function of intensity measured on samples of $K^+ \to \pi^+\pi^0$ and $K^+ \to \mu^+\nu_\mu$. **Top:** as measured on 2021 data, **Middle:** as emulated on 2021 data, **Bottom:** ratio of measured data/emulated data.

LKr. For NA62 run-1 the criteria for the LKr L0 in the PNN trigger line required that no more than two energy clusters exceed 5 GeV and additionally no single cluster exceeds 30 GeV; for NA62 run-2 this single energy requirement has been increased to 40 GeV after improvements to the reconstruction software.

Figure 5.8 shows the efficiency of the LKr L0 condition as a function of both energy and momentum for 2018 and 2021 data highlighting the difference between the NA62 run-1 and NA62 run-2 conditions. Considering Figure 5.8a we can see the increased efficiency at higher energies in 2021 by accepting pions up to an energy of 40 GeV. However, we see the efficiency at lower energies has been compromised. The origin of this reduced efficiency is unknown but is suspected to be related to changes in the logic surrounding energy clusters, and in particular the condition in which no more than two clusters must exceed 5 GeV of energy deposited. Consequently, whilst we might have expected an increase in efficiency as a function of momentum, we in fact see a decrease compared to NA62 run-1. Work is ongoing to confirm the cause of the reduced efficiency and to resolve the issue.

The overall L0 trigger efficiency for the $K^+ \to \pi^+\nu\bar{\nu}$ decay is the product of all the individual L0 components and is a function of both intensity and momentum, see Figure 5.9. The largest contribution to the inefficiency arises from the LKr trigger condition.

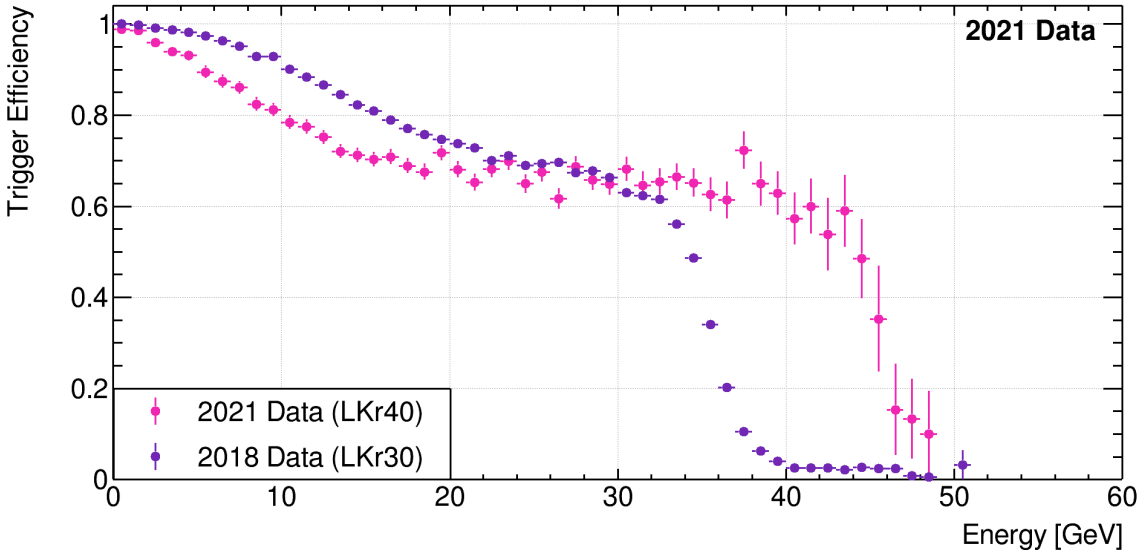

(a) Function of energy deposited in the LKr.

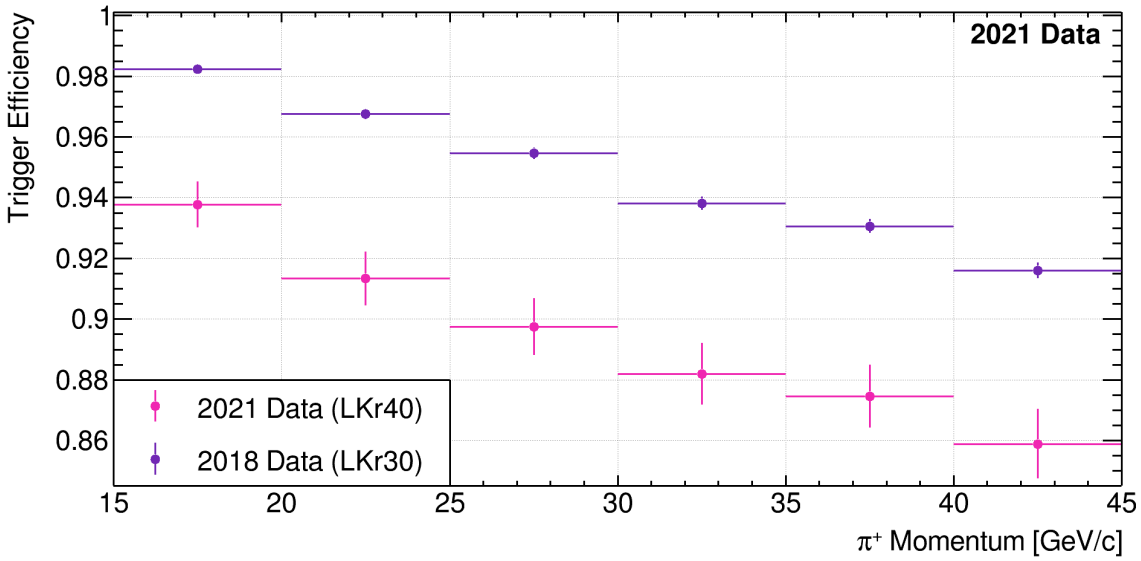

(b) Function of the outgoing π^+ momentum.

Figure 5.8: Trigger Efficiency of the LKr L0 condition for the $K^+ \to \pi^+\nu\bar{\nu}$ trigger line. For 2021 this condition was requiring that no more than 40 GeV is deposited as a single cluster, and no 2 clusters deposit more than 5 GeV combined.

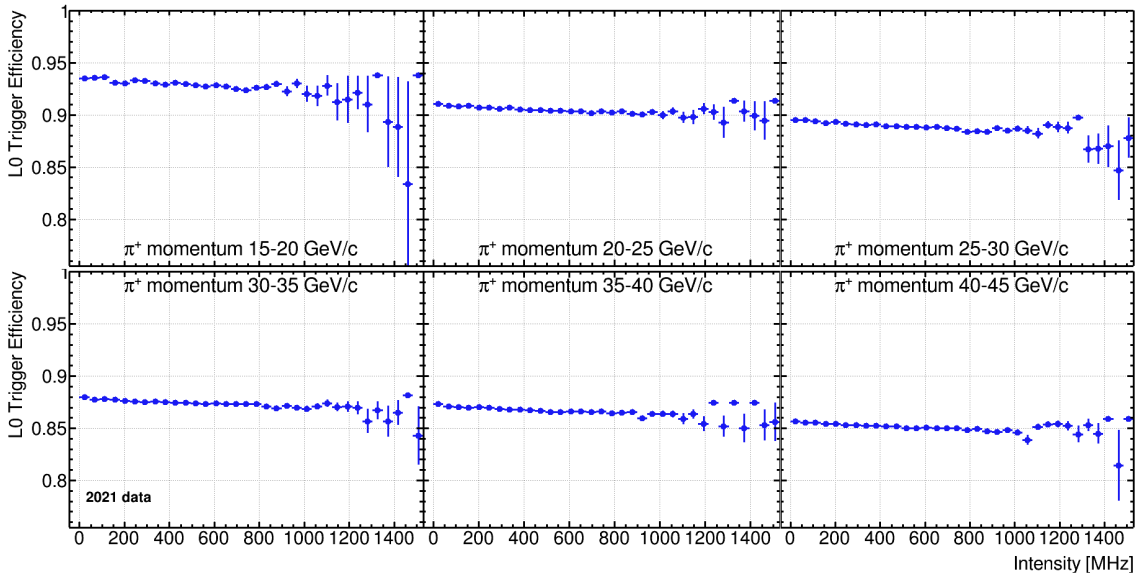

Figure 5.9: Trigger Efficiency of the $K^+ \to \pi^+\nu\bar{\nu}$ trigger conditions as a function of intensity in bins of the outgoing π^+ momentum.

5.3.2 L1

If an event provides a positive L0 trigger decision for a given trigger line, the high-level trigger (HLT) software collects data from all detectors, except for the GTK and calorimeters, and executes the L1 trigger algorithms. Algorithms are performed in a specified order according to the trigger line. If an event passes all L1 trigger algorithms for a given trigger line, data from the GTK and calorimeters is requested by the HLT and merged with the L1 event forming the complete event written to disk. To test the efficiency of each of the algorithms, *autopass* events can be used; however to increase statistics, a sample of $K^+ \to \mu^+\nu_\mu$ events selected with the minimum bias trigger are instead used. These L1 trigger efficiencies are validated with *autopass* events to ensure we remain unbiased.

Figure 5.10 shows the efficiency of the L1 algorithms for both the PNN and Non-μ trigger lines measured on 2021 data. Here the L1 KTAG algorithm is measured with an efficiency of 99.8% for both trigger lines. The L1 LAV algorithm varies as a function of intensity and ranges from 99.8% to ∼93%. An inefficiency arises here

due to random veto as the time window used by the L1 algorithm is larger than that used in the $K^+ \to \pi^+\nu\bar{\nu}$ selection.

The STRAW algorithms performed in each trigger line are subject to different criteria. The STRAW-1TRK algorithm in the Non-μ trigger line requires a track to have a momentum of less than 65 GeV/c and originate inside the fiducial volume. The efficiency of the STRAW-1TRK is measured as ranging from 99.8% down to 99.0%. The PNN trigger line uses a more restrictive version of the STRAW algorithm, optimised for the $K^+ \to \pi^+\nu\bar{\nu}$ decay, in which the track must have positive charge, momentum below 50 GeV/c, CDA to the nominal beam axis of less than 200 mm and originating upstream of the first STRAW chamber. In addition, multi-track events in which it is suspected that they originate from the same vertex are also rejected. Figure 5.11 shows the efficiency of the L1 STRAW algorithm used in the PNN trigger line as a function of momentum. Improvements in this algorithms efficiency, in particular in the final momentum bin, have been made since the publication of the NA62 run-1 trigger paper [75] by increasing the threshold used in the trigger algorithm.

The overall L1 trigger efficiency is the combination of all trigger algorithms performed on each trigger line and is found to be 99.3% for the Non-μ trigger line and 94.7% for the PNN trigger line.

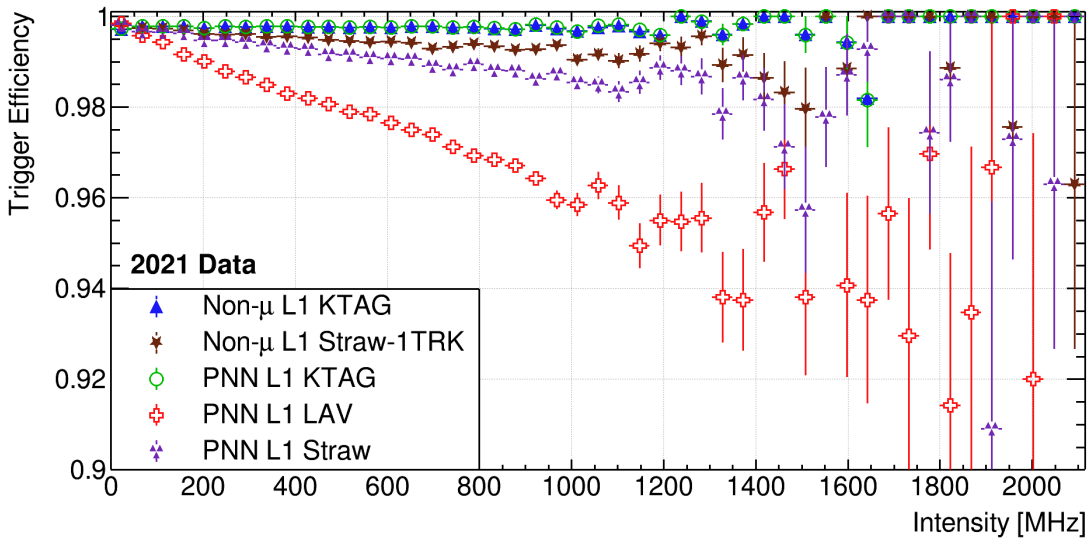

Figure 5.10: Efficiency of the L1 trigger algorithms as a function of intensity for the Non-μ and PNN trigger lines as measured on 2021 minimum bias data satisfying the corresponding L0 trigger conditions.

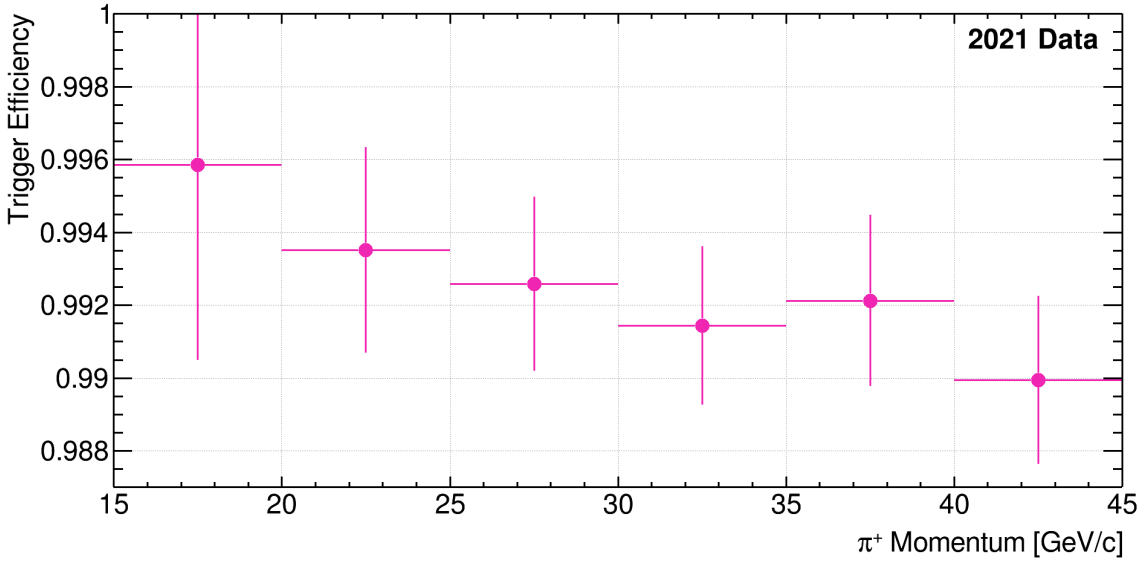

Figure 5.11: L1 STRAW efficiency as a function of momentum for the PNN trigger line measured on 2021 data.

5.3.3 Status for the 2021 analysis

The overall trigger efficiency is the product of the L0 and L1 efficiencies and varies as a function of intensity and momentum. For data collected in 2018 this was found to be $\epsilon^{\text{trig}}_{\pi\nu\nu} = (88.8 \pm 0.5)\%$ decreasing in 2021 to $\epsilon^{\text{trig}}_{\pi\nu\nu} = (83.8 \pm 1.6)\%$. The dominating contribution to this efficiency measurement lies in the LKr L0, and whilst there has been an attempt to increase the efficiency for the NA62 run-2 analysis by increasing the single energy cluster requirement to 40 GeV, the efficiency measurement at present is lower than that in 2018 data. Work is currently ongoing to investigate the source of the reduced efficiency.

Further changes occurring between the analysis in NA62 run-1 and NA62 run-2 lie in the L1 algorithms. Firstly, the z-position of the decay vertex has been incorporated into the L1 LAV algorithm such that only stations downstream of the decay are included in the veto time window. This reduces the number of events unnecessarily vetoed and has increased the efficiency of the algorithm. Moreover, in increasing the momentum threshold used in the L1 STRAW algorithm the efficiency, particularly in the final momentum bin, has improved.

5.4 Acceptance

The acceptance is defined as the number of simulated events passing some selection criteria normalised to the number of desired K^+ decays in the fiducial volume, in this case defined to be 105–170 m. As we are required to know exactly how many K^+ decays are into a given final state, this can only be measured on MC data. Whilst some effects might not be accurately simulated, as the single event sensitivity (see Equation 5.6) uses the ratio of $A_{\pi\pi}/A_{\pi\nu\bar{\nu}}$ these effects will cancel and are thus not an issue. Some examples of these effects are random veto due to additional activity

in the CHANTI, MUV3, and GTK detectors, or inefficiencies in the reconstruction of detectors such as the KTAG, STRAW, RICH and CHOD.

Whilst the acceptance can be measured as a function of intensity, such dependence contains information on the random veto which has already been accounted for separately. Thus the acceptance at zero intensity is used in the single event sensitivity calculation. Instead, the acceptance measurement is split into 5 GeV/c wide momentum bins, so that momentum dependent cuts can be optimised. Figure 5.12 shows the acceptance of the $K^+ \to \pi^+\nu\bar{\nu}$, $K^+ \to \pi^+\pi^0$ and $K^+ \to \mu^+\nu_\mu$ selections as a function of momentum. The total acceptance is calculated by integrating over the full momentum range and is shown in Table 5.2 for both 2018 and 2021 data-taking conditions.

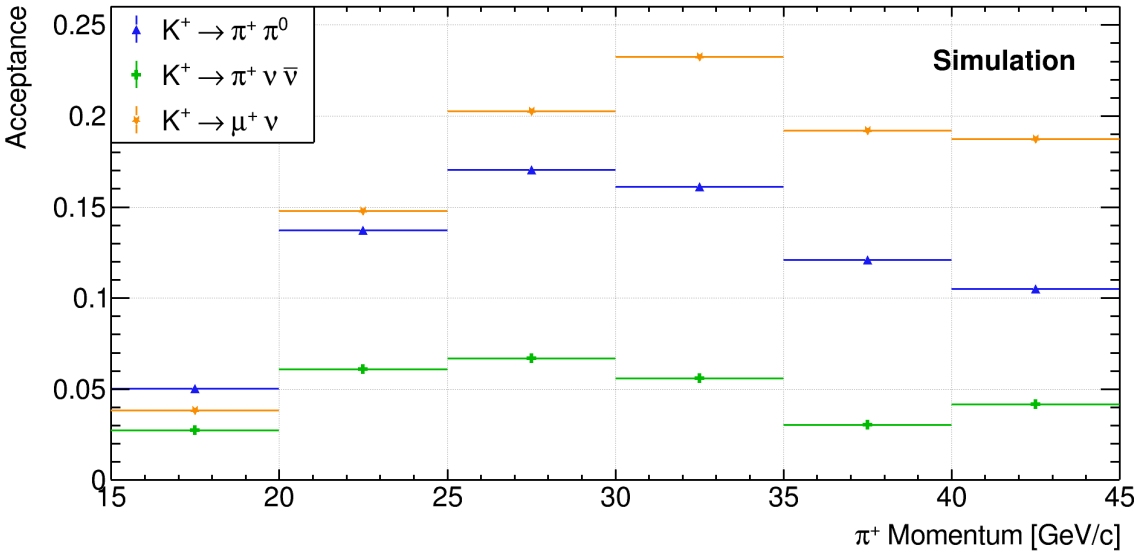

Figure 5.12: Acceptance as a function of momentum for each of the three decays used in this $K^+ \to \pi^+\nu\bar{\nu}$ study.

Table 5.2: Acceptances of the selections used in the $K^+ \to \pi^+\nu\bar{\nu}$ analysis.

Decay	Acceptance [(value ± 0.01)%] 2018	2021
$K^+ \to \pi^+\nu\bar{\nu}$	7.59	7.78
$K^+ \to \pi^+\pi^0$	12.76	13.08
$K^+ \to \mu^+\nu_\mu$	17.54	18.45

5.4.1 Status for the 2021 analysis

As a result of the increased intensity of the NA62 run-2 data set, the selection criteria needs to be reoptimised. Since the publication of the NA62 run-1 results [12], the changes to the selection criteria are:

- The new detectors added for NA62 run-2 have been incorporated into the analysis procedure improving the rejection power against backgrounds originating upstream of the fiducial decay volume.
- The improvements to the offline reconstruction algorithms used in clustering energy deposits in the LKr have allowed for the relaxation of the cuts described in subsection 5.2.3. Consequently this has improved the random veto efficiency, ϵ_{RV}.
- The selection criteria targeting the rejection of additional activity has been reoptimised for the increased intensity of NA62 run-2.
- The allowed region for a decay vertex to be reconstructed in has been reoptimised for the increased intensity. As a result the backgrounds have been reduced whilst increasing the signal acceptance.

These improvements have led to a marginal increase in the acceptances shown in Table 5.2, and consequently have increased the effective signal efficiency propagated into the single event sensitivity calculation.

5.5 Number of normalisation events

The final component entering the single event sensitivity calculation is the number of normalisation events, $N_{\pi\pi}$, collected in a given data-taking period. Whilst the

SES calculation uses the total number of counted normalisation events, it is also useful to investigate how $N_{\pi\pi}$ varies as a function of intensity. This does not come without some caveats. As the number of $K^+ \to \pi^+\pi^0$ events is a count, a time window in which we have counted is implied and thus the idea of measuring $N_{\pi\pi}$ as a function of the instantaneous intensity like was done for the random veto or trigger efficiencies is nonsensical. We instead arbitrarily consider the quantity $N_{\pi\pi}$ per burst as a function of intensity.

Figure 5.13 shows the number of normalisation events measured in a given burst as a function of the mean intensity of the burst. Immediately we run into issues, firstly we see the lack of statistics across the intensity range making any sort of conclusion about how this quantity varies as a function of intensity difficult to state with any meaningful certainty. Additionally, this results in a lack of understanding with whether we are running at the optimal intensity for collecting $K^+ \to \pi^+\pi^0$ events, or, after further manipulation, whether we are running at the optimal intensity for collecting $K^+ \to \pi^+\nu\bar{\nu}$ events. Secondly, we note the tail of the distribution where the number of $N_{\pi\pi}$ is lower than expected due to bad bursts. A burst could be labelled as bad for a number of reasons, this could be a detector not correctly recording the data or alternatively it could be related to the intensity distribution throughout the spill.

To improve the understanding of the optimal intensity at which to run the experiment at, alternative methods for estimating the number of $K^+ \to \pi^+\pi^0$ events are proposed and discussed in the following section.

5.5.1 New procedure

An alternative procedure is to count the number of $K^+ \to \pi^+\pi^0$ events per second. This provides a larger spread of intensity values due to inconsistencies in the spill

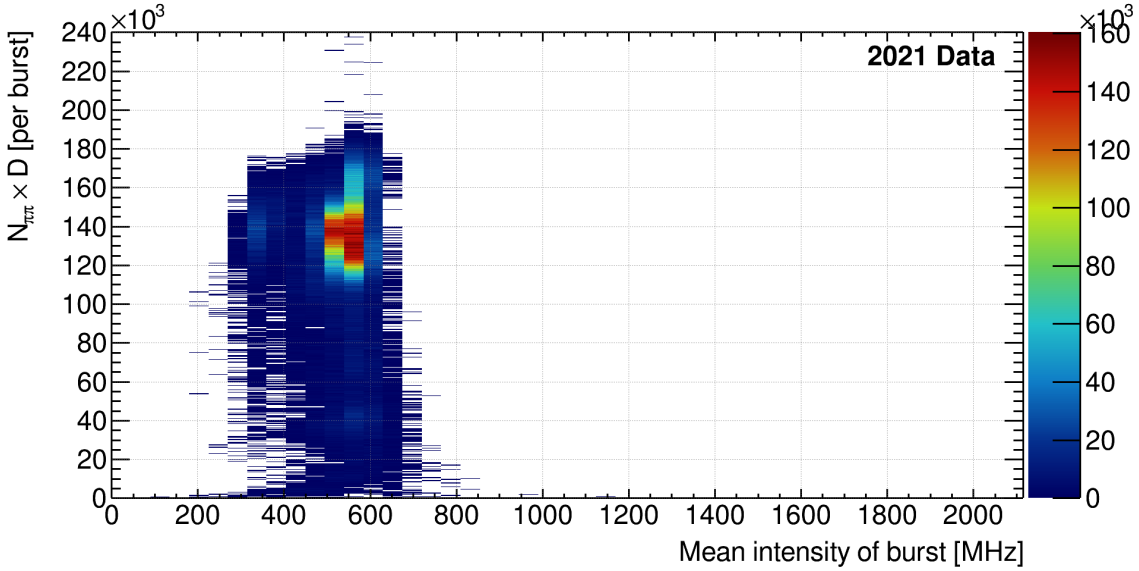

Figure 5.13: Number of $K^+ \to \pi^+\pi^0$ events collected per burst ($\sim 4.2\,\text{s}$) as a function of the mean intensity of the burst measured on 2021 data. The number of events has been multiplied by the downscaling factor to better reflect the total number of events.

structure. To allow for a direct comparison to the previous method, we extrapolate the number of $K^+ \to \pi^+\pi^0$ counted inside a 1 s time window to the average length of a burst, 4.2 s.

Another procedure and an analytical approach is adopted by rearranging Equation 5.3:

$$N_{\pi\pi} = \frac{\mathcal{B}_{\pi\pi} A_{\pi\pi} \epsilon_{\pi\pi}^{\text{trig}}}{D} N_k, \tag{5.8}$$

where the branching fraction ($\mathcal{B}_{\pi\pi}$) is precisely known, the acceptance ($A_{\pi\pi}$) has been discussed in section 5.4, and the trigger efficiency ($\epsilon_{\pi\pi}^{\text{trig}}$) with downscaling ($D$) has been discussed in section 5.3. The remaining factor is determined by estimating the number of effective kaons, N_k, at any given intensity.

We start by using the estimated beam intensity distribution in which we can sample an events intensity and convert this into a number of tracks passing through the GTK in the intensity estimators 45 ns time window, see Equation 4.2. Of these tracks, 6% are expected to be kaons due to the hadronic beam composition. As we

wish to convert this estimate into the number of effective kaons in a burst to match the previous method, we consider how many 45 ns time windows are in a burst of average length 4.2 s. Finally, we consider how many of these kaons detected in the GTK would decay inside the fiducial volume which, after studying MC, is calculated as 25%. Putting all of these components together, see Equation 5.9, and plotting the resulting distribution we find that we need an additional scale factor of 1/3 such that we have agreement with the original method.

time windows in a burst

Fraction decaying in FV

$$N_k = I \times 45\,\text{ns} \times 0.06 \times \frac{4.2\,\text{s}}{45\,\text{ns}} \times 0.25 \times \frac{1}{3}\,. \tag{5.9}$$

Number of tracks

6% kaons

Unknown effects

For this method to be viable, the unknown factor of 1/3 needs to be understood. Components that could contribute to this additional factor are things such as the dead time of the L0TP, detector CHOKEs, and a fraction of events that are corrupted/bad due to detector inefficiencies.

An alternate data driven approach was also suggested. For each burst we obtain the distribution of instantaneous intensity measured using minimum bias triggered data. To then understand the effective time where the beam was at a given intensity we can reweight this histogram such that instead of the number of events, N_{events}, its bin contents are the time, t, spent at any given intensity, I:

$$t = \frac{N_{\text{events}}}{I}. \tag{5.10}$$

If we also count the number of normalisation events at a given intensity for each burst we can convert this observed number of normalisation events, $N_{\pi\pi}^{\text{obs}}$, into the

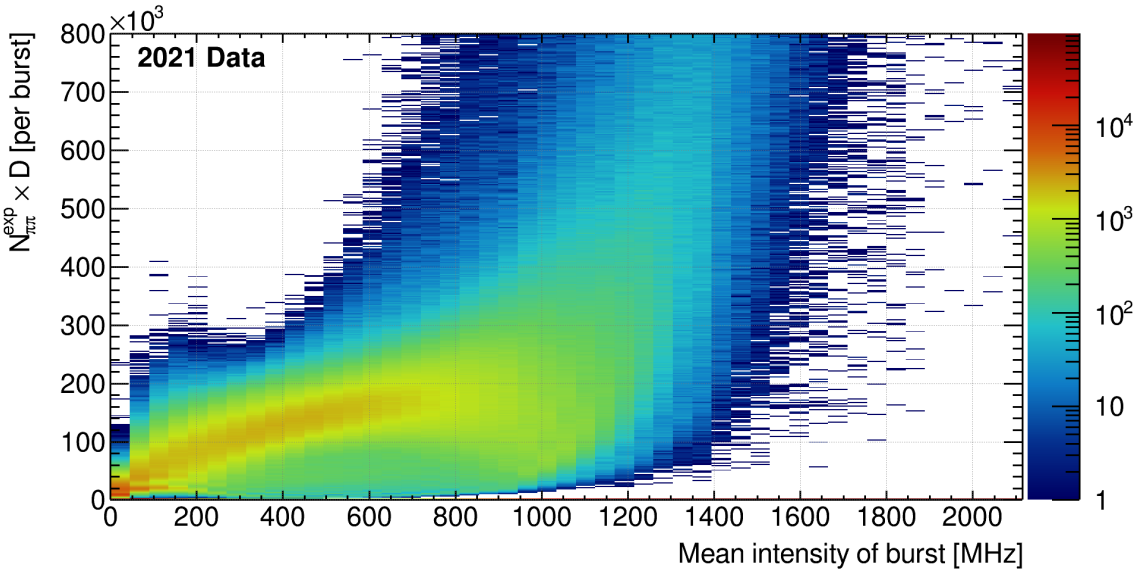

Figure 5.14: Expected number of $K^+ \to \pi^+\pi^0$ events per burst as a function of the mean intensity of the burst calculated using 2021 data.

expected number of normalisation events, $N^{\text{exp}}_{\pi\pi}$:

$$N^{\text{exp}}_{\pi\pi}(I) = \frac{N^{\text{obs}}_{\pi\pi}}{P(t|I)}, \tag{5.11}$$

where $P(t|I)$ is the fraction of time spent in the given burst at a certain intensity provided by the reweighted histogram described above. Figure 5.14 shows the resultant number of normalisation events, per burst, as a function of the mean intensity of a burst and we see a drastic improvement to the statistics across the intensity range, compare to Figure 5.13.

5.5.2 Status for the 2021 analysis

Figure 5.15 shows the distribution of the number of expected normalisation events per burst, multiplied by the downscaling factor, as a function of the mean intensity of a burst for 2021 data; each of the methods described above are shown. The original method of counting the number of normalisation events inside a burst provides the least wide range of intensity values, whilst we see a marginal increase by considering

the number of $N_{\pi\pi}$ events per second and scaling this to the average length of a burst. Additionally, as the spill structure of a burst does not provide a uniform intensity, see Figure 4.3, these results are typically lower than would be expected if we were to have a 'perfect' burst at a consistent intensity. The new analytical method shows a consistent distribution in-line with the expected result of some optimal peak before a decrease in the number of normalisation events collected due to random veto effects or trigger inefficiencies. We see the new data-driven approach also matches this analytical method with good accuracy up to $\sim 1100\,\text{MHz}$ in which there becomes a significant spread of $N_{\pi\pi}$ values resulting in large errors on the mean value. An improvement to the accuracy of this measurement can be made by averaging over a number of bursts and the values shown in Figure 5.15 have been calculated by averaging over 10 bursts. Further improvements can be made by directly improving the spill structure and it is expected that the errors in this distribution for data collected in 2022 shall be smaller for this reason.

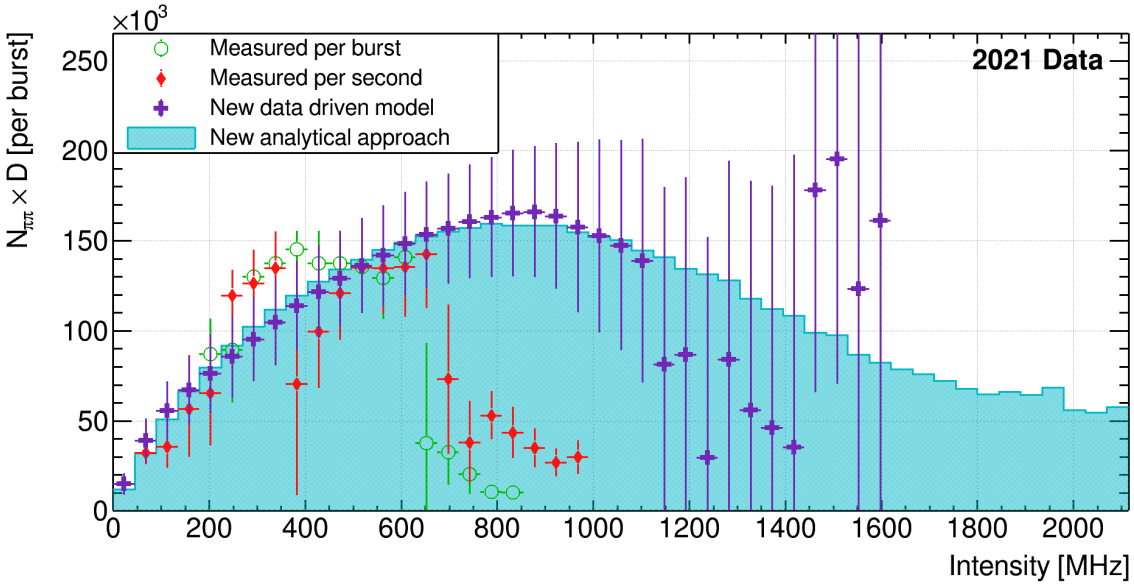

Figure 5.15: Number of normalisation events (per burst) as a function of intensity measured using 2021 data. All four methods discussed are shown.

Whilst the analytical method provides the expected behaviour of the number of normalisation events as a function of intensity well, the unknown factor of 1/3 would need to be understood. Therefore, the new data-driven method has been chosen for

this study due to the reduction in systematic errors propagated to the final single event sensitivity calculation and consequently the plot of expected $K^+ \to \pi^+\nu\bar{\nu}$ events per burst as a function of intensity.

Figure 5.16 shows the distribution of the number of expected normalisation events per burst for 2018 data. Again we see all the methods agree. We take note that the optimal intensity for 2018 is at $\sim 650\,\text{MHz}$ with $\sim 220,000$ $N_{\pi\pi}$ events per burst before we start to lose events due to inefficiencies in the analysis. This value has been increased to $\sim 800\,\text{MHz}$ for 2021 before the number of normalisation events plateaus at $\sim 170,000$ $N_{\pi\pi}$ events per burst highlighting the improved efficiency of the analysis at higher intensities for NA62 run-2. However, there was a reduction in the number of normalisation events collected per burst due to poor spill quality in 2021 with often significant spikes in intensity at the start of a burst out of the control of NA62, see Figure 4.3. This resulted in the remainder of the burst operating at a lower beam intensity than expected. We also note that this discussion is the optimal beam intensity for collecting $K^+ \to \pi^+\pi^0$ events and not necessarily the optimal intensity for collecting $K^+ \to \pi^+\nu\bar{\nu}$ events. Furthermore, the distribution shown is a direct status of the present analysis and the optimal intensity may be increased with changes to the selection after the data collection itself.

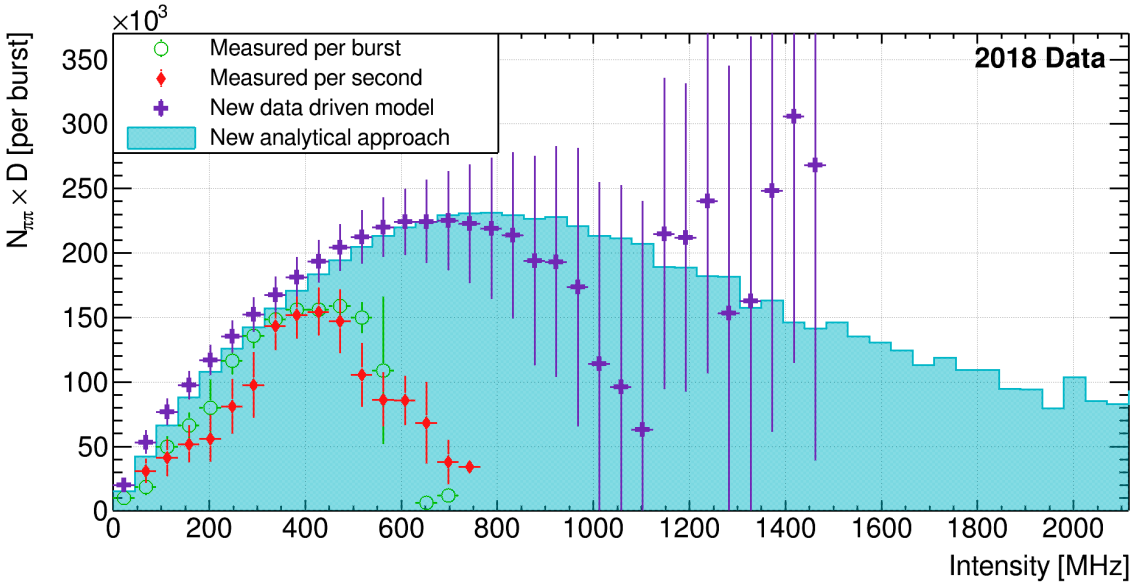

Figure 5.16: Number of normalisation events (per burst) as a function of intensity measured using 2018 data. All four methods discussed are shown.

5.6 Compiling results

In compiling all of the separate components discussed in this chapter, we find the single event sensitivity for data collected in 2021 is:

$$\mathcal{B}_{SES} = (5.00 \pm 0.13_{\text{stat}}) \times 10^{-11}. \tag{5.12}$$

By assuming a SM branching ratio of $\mathcal{B}(K^+ \to \pi^+\nu\bar{\nu}) = (8.60 \pm 0.42) \times 10^{-11}$ [12], we expect 1.72 $K^+ \to \pi^+\nu\bar{\nu}$ events. We note that this is approximately four times smaller than the value obtained in 2018, however the number of good bursts collected in 2021 was also approximately a quarter of that collected in 2018. By calculating the expected number of $K^+ \to \pi^+\nu\bar{\nu}$ events per burst we find:

$$\left(\frac{N^{\text{exp}}_{\pi\nu\nu}}{N_{\text{bursts}}}\right)_{2021} = 1.64 \times 10^{-5} \qquad \left(\frac{N^{\text{exp}}_{\pi\nu\nu}}{N_{\text{bursts}}}\right)_{2018} = 1.75 \times 10^{-5}. \tag{5.13}$$

We see that whilst improvements have been made to the $K^+ \to \pi^+\nu\bar{\nu}$ analysis we in fact see a similar number of signal events per burst to that collected in 2018.

Moreover, whilst this is the current status of the analysis at the time of submission, further improvements to the analysis are ongoing and the number of $K^+ \to \pi^+\nu\bar{\nu}$ events expected could increase by a small amount.

Additionally, if we leave the intensity dependence in the single event sensitivity and use the number of normalisation events per burst as a function of intensity, one can obtain the expected number of $K^+ \to \pi^+\nu\bar{\nu}$ events per burst as a function of intensity, see Figure 5.17. Again we note that the number of $K^+ \to \pi^+\nu\bar{\nu}$ events expected per burst is lower for 2021 than in 2018 albeit to a greater level than the values shown in Equation 5.13. This can be explained by the quality of the spill structure in the two data-taking periods and additionally in highlighting its limiting effect on the studies shown in this thesis. We do however see that the intensity at which we can collect these events is larger for 2021 than in 2018 reflecting the changes to the analysis accommodating the increased beam intensity. For 2018, it appears as though the optimal intensity to run NA62 at was between 400–500 MHz whilst for 2021 this is increased to 500–600 MHz. Consequently, in 2021 we were operating at a beam intensity that was beyond this peak and resulted in a loss of events collected. It is important to note that this is the optimal intensity for collecting $K^+ \to \pi^+\nu\bar{\nu}$ events with the current status of the analysis and improvements could be made that suggest a higher intensity is better. We also note that the optimal intensity for collecting $K^+ \to \pi^+\nu\bar{\nu}$ events is different to that for collecting the normalisation events described in subsection 5.5.2. In 2022, the spike in intensity at the start of the spill has been removed and a more uniform beam intensity is provided across the entire length of the burst. As a result of this analysis, the beam intensity requested by NA62 has been reduced for data collected in 2023 such that we more efficiently analyse the collected data.

Figure 5.18 shows how each of the SES components contribute to the distribution of expected $K^+ \to \pi^+\nu\bar{\nu}$ events per burst as a function of intensity; the acceptance

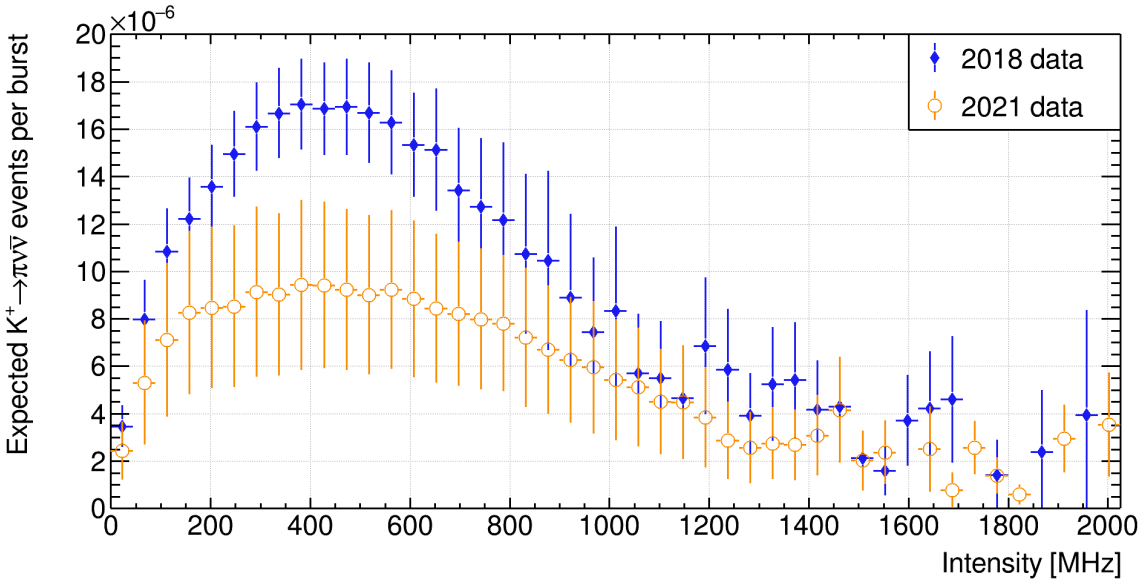

Figure 5.17: Expected number of $K^+ \to \pi^+\nu\bar{\nu}$ events per burst as a function of the mean intensity of the burst.

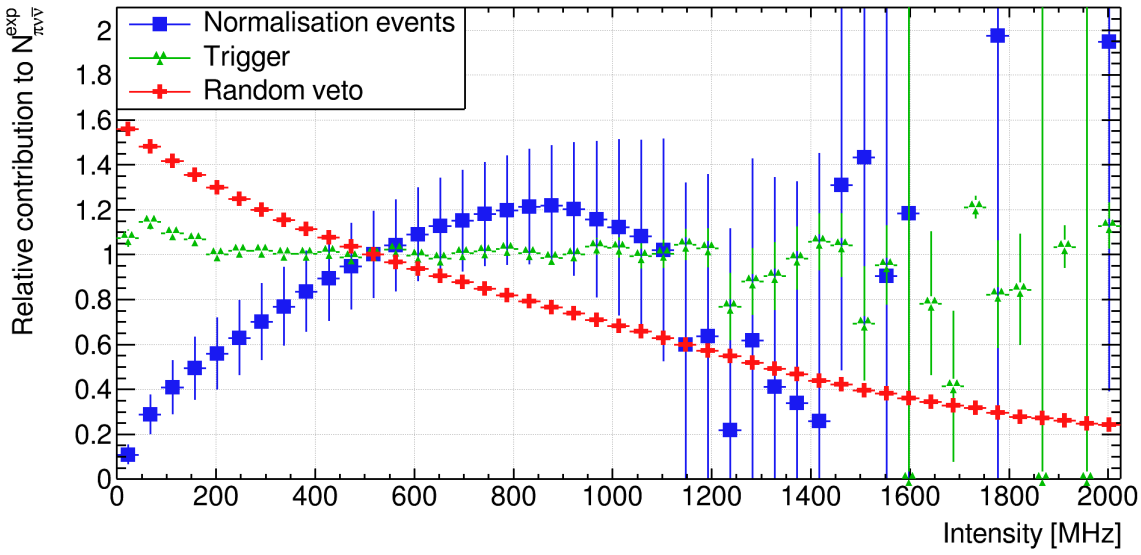

Figure 5.18: Components contributing to the distribution of $K^+ \to \pi^+\nu\bar{\nu}$ events per burst as a function of intensity. Each component has been normalised relative to its value at an intensity of 500 MHz.

has been left out of this plot as the intensity independent value is used. Here each component has been normalised to its value at an intensity of 500 MHz. The dominant component dictating the shape of this distribution is the random veto which also effects the number of $N_{\pi\pi}$ as a function of intensity. The ratio of the trigger efficiencies are almost independent with intensity. Therefore, to improve the expected number of $K^+ \to \pi^+\nu\bar{\nu}$ events it is recommended to focus on improvements to the random veto. Additionally, we take note that the optimisation of the single event sensitivity is a mandatory condition but not sufficient to achieve a precise measurement of the branching ratio of $K^+ \to \pi^+\nu\bar{\nu}$. Minimisation of the background contamination is also a factor to be considered.

5.7 Summary

In this chapter, the fundamentals of the $K^+ \to \pi^+\nu\bar{\nu}$ analysis have been discussed. Each component entering into the SES calculation have been explored as a function of intensity with the aim of finding the optimal beam intensity to collect $K^+ \to \pi^+\nu\bar{\nu}$ events at NA62. Changes to the analysis procedure between 2018 and 2021 have been highlighted.

The single event sensitivity for 2021 has been calculated to be:

$$\mathcal{B}_{SES} = (5.00 \pm 0.13_{\text{stat}}) \times 10^{-11}, \tag{5.14}$$

resulting in an expected 1.72 $K^+ \to \pi^+\nu\bar{\nu}$ events. Although this value is approximately four times smaller than that obtained in 2018, the number of bursts collected in 2021 is approximately a quarter of that collected in 2018. Whilst investigating how each of the components entering into the SES calculation vary as a function of intensity, we see we are dominated by the contribution of the random veto. The

optimal beam intensity for NA62 in collecting $K^+ \to \pi^+\nu\bar{\nu}$ events has been shown to be between 500–600 MHz and as a result of this analysis, the beam intensity of data collected in 2023 has been reduced to 500 MHz.

Chapter 6

Conclusions

A design for a new CEDAR detector to be used in the NA62 experiment with hydrogen as the radiator gas has been presented. The new detector design, called Cedar-H, and its expected performances with a working pressure of 3.80 bar pressure are presented. The Cedar-H designed by the author was built and tested at CERN in 2022, comissioned and used in NA62 data-taking in 2023. Furthermore, measured performances of the Cedar-H were found to be more than satisfactory with an increase in light yield of 20% compared to that of Cedar-W using nitrogen as radiator gas.

Significant improvements have been made to the simulation of pileup events in the NA62 detector. Software written by the author was implemented and certified to automate the procedure of generating beam intensity templates for each data-taking period.

An investigation into the optimal beam intensity for the NA62 $K^+ \to \pi^+ \nu\bar{\nu}$ analysis has been performed. An overview of the analysis procedure is discussed along with summarising the NA62 results achieved with data collected in 2016-2018. All components entering into the single event sensitivity are discussed individually along with their dependence on the beam intensity. A study of the 2021 dataset

is performed by the author and presented and the differences of the $K^+ \to \pi^+\nu\bar{\nu}$ analysis on 2021 data with respect to the previous analyses are highlighted. A single event sensitivity of:

$$\mathcal{B}_{SES} = (5.00 \pm 0.13_{\text{stat}}) \times 10^{-11}, \tag{6.1}$$

is achieved for the 2021 dataset resulting in an expected 1.72 $K^+ \to \pi^+\nu\bar{\nu}$ events. The optimal beam intensity for the present state of the analysis as obtained in the author's studies reported in this thesis is in the range 500–600 MHz. Consequently, the intensity of the beam at NA62 has been reduced to 500 MHz for data-taking in 2023 and will remain at this value for the next 2 years of planned data-taking.

References

[1] Jun Cao and Miao He. 'Neutrino Oscillation: Discovery and Perspectives'. In: *Science Bulletin* 61.1 (Jan. 2016), pp. 48–51. DOI: 10.1007/s11434-015-0969-7.

[2] A D Sakharov. 'Violation of CP in Variance, C, Asymmetry, and Baryon Asymmetry of the Universe'. In: *Sov. Phys. Usp.* 34.5 (1991). DOI: 10.1070/PU1991v034n05ABEH002497.

[3] M.S. Roberts and A.H. Rots. 'Comparison of Rotation Curves of Different Galaxy Types'. In: *Astronomy and Astrophysics* 26 (1973), pp. 483–485.

[4] Christian Gross et al. 'Dark Matter in the Standard Model?' In: *Phys. Rev. D* 98.6 (Sept. 2018), p. 063005. arXiv: 1803.10242 [astro-ph, physics:hep-ph].

[5] ATLAS Collaboration. 'Observation of a New Particle in the Search for the Standard Model Higgs Boson with the ATLAS Detector at the LHC'. In: *Physics Letters B* 716.1 (Sept. 2012), pp. 1–29. arXiv: 1207.7214 [hep-ex].

[6] CMS Collaboration. 'Observation of a New Boson at a Mass of 125 GeV with the CMS Experiment at the LHC'. In: *Physics Letters B* 716.1 (Sept. 2012), pp. 30–61. arXiv: 1207.7235 [hep-ex].

[7] M. K. Gaillard and Benjamin W. Lee. 'Rare Decay Modes of the K Mesons in Gauge Theories'. In: *Phys. Rev. D* 10.3 (Aug. 1974), pp. 897–916. DOI: 10.1103/PhysRevD.10.897.

[8] The NA62 collaboration. 'Precision Measurement of the Ratio of the Charged Kaon Leptonic Decay Rates'. In: (Jan. 2013). arXiv: 1212.4012.

[9] Giles David Barr et al. 'A New Measurement of Direct CP Violation in the Neutral Kaon System'. In: *Phys. Lett. B* 317 (1993), pp. 233–242. DOI: 10.1016/0370-2693(93)91599-I.

[10] V. Fanti et al. 'A New Measurement of Direct CP Violation in Two Pion Decays of the Neutral Kaon'. In: *Physics Letters B* 465.1 (Oct. 1999), pp. 335–348. DOI: 10.1016/S0370-2693(99)01030-8.

[11] KTeV Collaboration et al. 'Observation of Direct CP Violation in $K_{S,L} \to \pi\pi$ Decays'. In: *Phys. Rev. Lett.* 83.1 (July 1999), pp. 22–27. DOI: 10.1103/PhysRevLett.83.22.

[12] NA62 Collaboration. 'Measurement of the Very Rare $K^+ \to \pi^+\nu\bar{\nu}$ Decay'. In: *J. High Energ. Phys.* 2021.6 (June 2021), p. 93. arXiv: 2103.15389.

[13] University of Zurich. *Standard Model*. URL: http://www.physik.uzh.ch/en/researcharea/lhcb/outreach/StandardModel.html (visited on 27/06/2023).

[14] Nicola Cabibbo. 'Unitary Symmetry and Leptonic Decays'. In: *Phys. Rev. Lett.* 10.12 (June 1963), pp. 531–533. DOI: 10.1103/PhysRevLett.10.531.

[15] Makoto Kobayashi and Toshihide Maskawa. 'CP-Violation in the Renormalizable Theory of Weak Interaction'. In: *Progress of Theoretical Physics* 49.2 (Feb. 1973), pp. 652–657. DOI: 10.1143/PTP.49.652.

[16] R. P. Feynman and M. Gell-Mann. 'Theory of the Fermi Interaction'. In: *Phys. Rev.* 109.1 (1958), pp. 193–198. DOI: 10.1103/PhysRev.109.193.

[17] Ling-Lie Chau and Wai-Yee Keung. 'Comments on the Parametrization of the Kobayashi-Maskawa Matrix'. In: *Phys. Rev. Lett.* 53.19 (Nov. 1984), pp. 1802–1805. DOI: 10.1103/PhysRevLett.53.1802.

[18] Particle Data Group et al. 'Review of Particle Physics'. In: *Progress of Theoretical and Experimental Physics* 2022.8 (Aug. 2022). DOI: 10.1093/ptep/ptac097.

[19] Lincoln Wolfenstein. 'Parametrization of the Kobayashi-Maskawa Matrix'. In: *Phys. Rev. Lett.* 51.21 (Nov. 1983), pp. 1945–1947. DOI: 10.1103/PhysRevLett.51.1945.

[20] A. J. Buras, M. E. Lautenbacher and G. Ostermaier. 'Waiting for the Top Quark Mass, $K^+ \to \pi^+ \nu\bar{\nu}$, $B_s^0 - \bar{B}_s^0$ Mixing and CP Asymmetries in B-Decays'. In: *Phys. Rev. D* 50.5 (Sept. 1994), pp. 3433–3446. DOI: 10.1103/PhysRevD.50.3433. arXiv: hep-ph/9403384.

[21] J. Charles et al. 'CP Violation and the CKM Matrix: Assessing the Impact of the Asymmetric B Factories'. In: *Eur. Phys. J. C* 41.1 (May 2005). updated results and plots available at: http://ckmfitter.in2p3.fr. DOI: 10.1140/epjc/s2005-02169-1.

[22] G.D. Rochester and C.C. Butler. 'Evidence for the Existence of New Unstable Elementary Particles'. In: *Nature* 160 (1947), pp. 855–857. DOI: 10.1038/160855a0.

[23] R. Brown et al. 'Observations with Electron-Sensitive Plates Exposed to Cosmic Radiation*'. In: *Nature* 163.4133 (Jan. 1949), pp. 82–87. DOI: 10.1038/163082a0.

[24] T. D. Lee and C. N. Yang. 'Question of Parity Conservation in Weak Interactions'. In: *Phys. Rev.* 104.1 (Oct. 1956), pp. 254–258. DOI: 10.1103/PhysRev.104.254.

[25] J. H. Christenson et al. 'Evidence for the 2π Decay of the K_2^0 Meson'. In: *Phys. Rev. Lett.* 13.4 (July 1964), pp. 138–140. DOI: 10.1103/PhysRevLett.13.138.

[26] C. Lazzeroni et al. 'Precision Measurement of the Ratio of the Charged Kaon Leptonic Decay Rates'. In: *Physics Letters B* 719.4-5 (Feb. 2013), pp. 326–336. DOI: 10.1016/j.physletb.2013.01.037.

[27] KLOE Collaboration. 'Precise measurement of $\Gamma(K \to e\nu(\gamma))/(K \to \mu\nu(\gamma))$ and study of $K \to e\nu\gamma$'. In: European Physical Journal C.64 (2009), pp. 627–636. DOI: 0.1140/epjc/s10052-009-1177-x.

[28] S. L. Glashow, J. Iliopoulos and L. Maiani. 'Weak Interactions with Lepton-Hadron Symmetry'. In: *Phys. Rev. D* 2.7 (Oct. 1970), pp. 1285–1292. DOI: 10.1103/PhysRevD.2.1285.

[29] Andrzej J. Buras and Elena Venturini. 'Searching for New Physics in Rare K and B Decays without $|V_{cb}|$ and $|V_{ub}|$ Uncertainties'. In: *Acta Physica Polonica B* (June 2022). DOI: 10.5506/aphyspolb.53.6-a1. arXiv: 2109.11032.

[30] Giancarlo D'Ambrosio and Gino Isidori. '$K^+ \to \pi^+\nu\bar{\nu}$: a rising star on the stage of flavour physics'. In: *Physics Letters B* 530.1-4 (Mar. 2002), pp. 108–116. DOI: 10.1016/S0370-2693(02)01328-X. arXiv: hep-ph/0112135.

[31] Joachim Brod and Martin Gorbahn. 'Electroweak Corrections to the Charm Quark Contribution to $K^+ \to \pi^+\nu\bar{\nu}$'. In: *Phys. Rev. D* 78.3 (Aug. 2008), p. 034006. DOI: 10.1103/PhysRevD.78.034006. arXiv: 0805.4119 [hep-ph].

[32] Federico Mescia and Christopher Smith. 'Improved Estimates of Rare K Decay Matrix-Elements from Kl3 Decays'. In: *Phys. Rev. D* 76.3 (Aug. 2007), p. 034017. DOI: 10.1103/PhysRevD.76.034017. arXiv: 0705.2025 [hep-ph].

[33] Mikolaj Misiak and Joerg Urban. 'QCD Corrections to FCNC Decays Mediated by Z-penguins and W-boxes'. In: *Physics Letters B* 451.1-2 (Apr. 1999), pp. 161–169. DOI: 10.1016/S0370-2693(99)00150-1. arXiv: hep-ph/9901278.

[34] Gerhard Buchalla and Andrzej J. Buras. 'The Rare Decays $K \to \pi\nu\bar{\nu}$, $B \to X\nu\bar{\nu}$ and $B \to l^+l^-$ – An Update'. In: *Nuclear Physics B* 548.1-3 (May 1999), pp. 309–327. DOI: 10.1016/S0550-3213(99)00149-2. arXiv: hep-ph/9901288.

[35] Joachim Brod, Martin Gorbahn and Emmanuel Stamou. 'Two-Loop Electroweak Corrections for the $K \to \pi\nu\bar{\nu}$ Decays'. In: *Phys. Rev. D* 83.3 (Feb. 2011), p. 034030. DOI: 10.1103/PhysRevD.83.034030. arXiv: 1009.0947.

[36] Gino Isidori, Christopher Smith and Federico Mescia. 'Light-Quark Loops in $K \to \pi\nu\bar{\nu}$'. In: *Nuclear Physics B* 718.1-2 (July 2005), pp. 319–338. DOI: 10.1016/j.nuclphysb.2005.04.008. arXiv: hep-ph/0503107.

[37] Andrzej J. Buras et al. '$K^+ \to \pi^+\nu\bar{\nu}$ and $K_L \to \pi^0\nu\bar{\nu}$ in the Standard Model: Status and Perspectives'. In: *J. High Energ. Phys.* 2015.11 (Nov. 2015), p. 33. DOI: 10.1007/JHEP11(2015)033. arXiv: 1503.02693.

[38] J. K. Ahn et al. 'Search for $K_L \to \pi^0\nu\bar{\nu}$ and $K_L \to \pi^0 X^0$ Decays at the J-PARC KOTO Experiment'. In: *Phys. Rev. Lett.* 122.2 (Jan. 2019), p. 021802. DOI: 10.1103/PhysRevLett.122.021802.

[39] NA62 Collaboration. *A Study of the $K^+ \to \pi^0 e^+\nu\gamma$ Decay*. Apr. 2023. arXiv: 2304.12271.

[40] NA62 Collaboration. *Search for Dark Photon Decays to $\mu^+\mu^-$ at NA62*. Mar. 2023. arXiv: 2303.08666.

[41] NA62 Collaboration. 'A Search for the $K^+ \to \mu^- \nu e^+ e^+$ Decay'. In: *Physics Letters B* 838 (Mar. 2023), p. 137679. DOI: 10.1016/j.physletb.2023.137679.

[42] NA62 Collaboration. 'A Measurement of the $K^+ \to \pi^+ \mu^+ \mu^-$ Decay'. In: *J. High Energ. Phys.* 2022.11 (Nov. 2022), p. 11. arXiv: 2209.05076.

[43] NA62 Collaboration. 'Searches for Lepton Number Violating K^+ Decays'. In: *Physics Letters B* 797 (Oct. 2019), p. 134794. DOI: 10.1016/j.physletb.2019.07.041.

[44] NA62 Collaboration. 'Search for Lepton Number and Flavor Violation in K^+ and π^0 Decays'. In: *Phys. Rev. Lett.* 127.13 (Sept. 2021), p. 131802. DOI: 10.1103/PhysRevLett.127.131802.

[45] NA62 Collaboration. 'Searches for Lepton Number Violating $K^+ \to \pi^-(\pi^0)e^+e^-$ Decays'. In: *Physics Letters B* 830 (July 2022), p. 137172. DOI: 10.1016/j.physletb.2022.137172.

[46] NA62 collaboration. 'Search for Production of an Invisible Dark Photon in π^0 Decays'. In: *J. High Energ. Phys.* 2019.5 (May 2019), p. 182. DOI: 10.1007/JHEP05(2019)182.

[47] NA62 Collaboration. 'Search for Heavy Neutral Lepton Production in K^+ Decays to Positrons'. In: *Physics Letters B* 807 (Aug. 2020), p. 135599. DOI: 10.1016/j.physletb.2020.135599.

[48] NA62 collaboration. 'Search for K^+ Decays to a Muon and Invisible Particles'. In: *Physics Letters B* 816 (May 2021), p. 136259. DOI: 10.1016/j.physletb.2021.136259. arXiv: 2101.12304.

[49] NA62 Collaboration. 'Search for π^0 Decays to Invisible Particles'. In: *J. High Energ. Phys.* 2021.2 (Feb. 2021), p. 201. DOI: 10.1007/JHEP02(2021)201. arXiv: 2010.07644.

[50] NA62 Collaboration. *Search for a Feebly Interacting Particle X in the Decay* $K^+ \to \pi^+ X$. Jan. 2021. arXiv: 2011.11329.

[51] E. Cortina Gil et al. 'The Beam and Detector of the NA62 Experiment at CERN'. In: *J. Inst.* 12.05 (May 2017), P05025. DOI: 10.1088/1748-0221/12/05/P05025.

[52] NA62 Collaboration. *2019 NA62 Status Report to the CERN SPSC*. Tech. rep. CERN-SPSC-2019-012, SPSC-SR-249. CERN, 2019.

[53] NA62 Collaboration. *ADDENDUM I TO P326 Continuation of the Physics Programme of the NA62 Experiment*. Tech. rep. CERN-SPSC-2019-039, SPSC-P-326-ADD-1. 2019.

[54] NA62 Collaboration. *2020 NA62 Status Report to the CERN SPSC*. Tech. rep. CERN-SPSC-2020-007, SPSC-SR-266. Geneva: CERN, 2020.

[55] NA62 Collaboration. *2021 NA62 Status Report to the CERN SPSC*. Tech. rep. CERN-SPSC-2021-009, SPSC-SR-286. Geneva: CERN, 2021.

[56] NA62 Collaboration. *2022 NA62 Status Report to the CERN SPSC*. Tech. rep. CERN-SPSC-2022-012, SPSC-SR-306. Geneva: CERN, 2022.

[57] NA62 Collaboration. *2023 NA62 Status Report to the CERN SPSC*. Tech. rep. CERN-SPSC-2023-013, SPSC-SR-326. Geneva: CERN, 2023.

[58] NA62 Collaboration. 'NA62: Technical Design Document'. In: *CERN Document Server* (Dec. 2010). NA62-10-07.

[59] Claude Bovet et al. 'The CEDAR Counters for Particle Identification in the SPS Secondary Beams : A Description and an Operation Manual'. In: *CERN Document Server* CERN-82-13 (1982). Number: CERN-82-13 Publisher: CERN. DOI: 10.5170/CERN-1982-013.

[60] E. Goudzovski et al. 'Development of the Kaon Tagging System for the NA62 Experiment at CERN'. In: *Nucl. Instrum. Methods A* 801 (Nov. 2015), pp. 86–94. arXiv: 1509.03773.

[61] G. Aglieri Rinella et al. 'The NA62 GigaTracKer: A Low Mass High Intensity Beam 4D Tracker with 65 Ps Time Resolution on Tracks'. In: *J. Inst.* 14.07 (July 2019). arXiv: 1904.12837.

[62] H. Danielsson et al. 'New Veto Hodoscope ANTI-0 for the NA62 Experiment at CERN'. In: *JINST* 15.07 (2020).

[63] Marco Ceoletta. 'Upgrade of the DAQ System in the Veto Counter at NA62 and Performance Evaluation'. MA thesis. University of Padua, 2023. URL: https://thesis.unipd.it/handle/20.500.12608/45502?mode=simple (visited on 23/06/2023).

[64] F. Ambrosino et al. 'The CHarged ANTIcounter for the NA62 Experiment at CERN'. In: *Physics Procedia* 37 (2012), pp. 675–682. DOI: 10.1016/j.phpro.2012.04.095.

[65] F. Ambrosino et al. 'CHANTI: A Fast and Efficient Charged Particle Veto Detector for the NA62 Experiment at CERN'. In: *J. Inst.* 11.03 (Mar. 2016), P03029–P03029. arXiv: 1512.00244.

[66] A. Sergi. 'NA62 Spectrometer: A Low Mass Straw Tracker'. In: *Physics Procedia* 37 (2012), pp. 530–534. DOI: 10.1016/j.phpro.2012.03.713.

[67] B. Angelucci et al. 'Pion–Muon Separation with a RICH Prototype for the NA62 Experiment'. In: *Nucl. Instrum. Meth. A* 621.1-3 (Sept. 2010), pp. 205–211. DOI: 10.1016/j.nima.2010.05.062.

[68] F. Ambrosino et al. 'The Large-Angle Photon Veto System for the NA62 Experiment at CERN'. In: *2011 IEEE Nuclear Science Symposium Conference Record*. Oct. 2011, pp. 1159–1166. DOI: 10.1109/NSSMIC.2011.6154594.

[69] OPAL Collaboration. 'The OPAL Detector at LEP'. In: *Nucl. Instrum. Meth. A* 305.2 (July 1991), pp. 275–319. DOI: 10.1016/0168-9002(91)90547-4.

[70] J. Badier et al. *Shashlik Calorimetry*. Tech. rep. CERN-DRDC-93-28, DRDC-P-50. CERN, Aug. 1993.

[71] V. Fanti et al. 'The Beam and Detector for the NA48 Neutral Kaon CP Violation Experiment at CERN'. In: *Nucl. Instrum. Meth. A* 574.3 (May 2007), pp. 433–471. DOI: 10.1016/j.nima.2007.01.178.

[72] A Ceccucci et al. 'The NA62 Liquid Krypton Calorimeter's New Readout System'. In: *J. Inst.* 9.01 (Jan. 2014), pp. C01047–C01047. DOI: 10.1088/1748-0221/9/01/C01047.

[73] S. Kholodenko. 'NA62 Charged Particle Hodoscope. Design and Performance in 2016 Run'. In: *J. Inst.* 12.06 (June 2017). arXiv: 1705.05093.

[74] R. Ammendola et al. 'The Integrated Low-Level Trigger and Readout System of the CERN NA62 Experiment'. In: *Nucl. Instrum. Meth. A* 929 (June 2019), pp. 1–22. arXiv: 1903.10200.

[75] NA62 Collaboration. *Performance of the NA62 Trigger System*. Mar. 2023. arXiv: 2208.00897.

[76] S. Agostinelli et al. 'Geant4—a Simulation Toolkit'. In: *Nucl. Instrum. Meth. A* 506.3 (July 2003), pp. 250–303. DOI: 10.1016/S0168-9002(03)01368-8.

[77] Karl L Brown and F Christoph Iselin. *DECAY TURTLE (Trace Unlimted Rays Through Lumped Elements): A Computer Program for Simulating Charged-Particle Beam Transport Systems, Including Decay Calculations*. Tech. rep. Geneva: CERN, 1974. DOI: 10.5170/CERN-1974-002.

[78] ROOT team. *ROOT: Analysing Petabytes of Data, Scientifically*. URL: https://root.cern/ (visited on 17/05/2024).

[79] B M Bolotovskii. 'Vavilov–Cherenkov Radiation: Its Discovery and Application'. In: *Physics-Uspekhi* 52.11 (Nov. 2009). DOI: 10.3367/UFNe.0179.200911c.1161.

[80] H. Young and R. Freedman. *University Physics with Modern Physics*. 13th ed. Addison-Wesley, 2012.

[81] M. J. Riedl. 'The Mangin Mirror and Its Primary Aberrations'. In: *Appl Opt* 13.7 (July 1974), pp. 1690–1694. DOI: 10.1364/AO.13.001690.

[82] Angela Romano. 'Leptonic Decays and Kaon Identification at the NA62 Experiment at CERN'. PhD thesis. University of Birmingham, 2013.

[83] Karim Massri. 'Kaon Identification and Search for Lepton Number Violation in $K^{\pm}$ Decay-in-Flight Experiments at CERN'. PhD thesis. University of Birmingham, 2015.

[84] Francis Newson. 'Kaon Identification and the Search for Heavy Neutrinos at NA62'. PhD thesis. University of Birmingham, 2016.

[85] *R7400U-03 Datasheet*. URL: https://www.datasheetcatalog.com/datasheets_pdf/R/7/4/0/R7400U-03.shtml (visited on 30/04/2024).

[86] *R9880U_TPMH1321E*. URL: https://www.hamamatsu.com/content/dam/hamamatsu-photonics/sites/documents/99_SALES_LIBRARY/etd/R9880U_TPMH1321E.pdf (visited on 30/04/2024).

[87] Thomas Bache. 'Branching Ratio Measurement of the π^0 Dalitz Decay at NA62'. PhD thesis. University of Birmingham, 2022.

[88] J. Henshaw and J. Fry. *Design of a Hydrogen Filled Cedar*. Tech. rep. NA62-2021-03 [NA62 Internal Note]. Jan. 2021.

[89] A Lafuente et al. *Production of a New CEDAR-H Detector and Required Infrastructure for NA62*. Tech. rep. https://edms.cern.ch/document/2621859/0.2. URL: https://edms.cern.ch/document/2621859/0.2.

[90] C. Parkinson et al. *A New CEDAR for the NA62 Experiment*. URL: https://ep-news.web.cern.ch/content/new-cedar-na62-experiment (visited on 23/05/2023).

[91] NA62 Collaboration. *NA62 Framework*. URL: https://na62-sw.web.cern.ch/ (visited on 18/08/2023).

[92] Lydia Brenner et al. 'Comparison of Unfolding Methods Using RooFitUnfold'. In: *Int. J. Mod. Phys. A* 35.24 (May 2020). arXiv: 1910.14654.

[93] Tim Adye. 'Unfolding Algorithms and Tests Using RooUnfold'. In: *Proceedings of the PHYSTAT 2011 Workshop*. May 2011. arXiv: 1105.1160.

[94] Glen Cowan. *Statistical Data Analysis*. Oxford University Press, 1998.

[95] G. D'Agostini. 'A Multidimensional Unfolding Method Based on Bayes' Theorem'. In: *Nucl.Instrum.Meth.A* 362 (1995), pp. 487–498. DOI: 10.1016/0168-9002(95)00274-X.

[96] Bogdan Malaescu. *An Iterative, Dynamically Stabilized Method of Data Unfolding*. July 2009. arXiv: 0907.3791.

[97] E. Cortina Gil et al. 'First Search for $K^+ \to \pi^+\nu\bar{\nu}$ Using the Decay-in-Flight Technique'. In: *Physics Letters B* 791 (Apr. 2019), pp. 156–166. DOI: 10.1016/j.physletb.2019.01.067.

[98] NA62 Collaboration. 'An Investigation of the Very Rare $K^+ \to \pi^+\nu\bar{\nu}$ Decay'. In: *J. High Energ. Phys.* 2020.11 (Nov. 2020), p. 42. DOI: 10.1007/JHEP11(2020)042. arXiv: 2007.08218.

Appendix A

Cedar-H simulation parameters and tolerance plots

A.1 Cedar parameter values

Table A.1 shows the values of all parameters used in the Cedar-H simulations (NA62MC) highlighting the difference between Cedar-W and Cedar-H. The origin of the coordinate system is the start of the old Cedar nose (z=69.278 m) and unless otherwise stated all values quoted are in mm.

Table A.1: Simulation parameters for each Cedar design.

	Cedar Type	Cedar-W	Cedar-H
	Gas	N_2	H_2
	Pressure [bar]	1.71	3.80
Cedar			
Front Vessel	Length	339.0	280.0
	Inner Radius	139.0	139.0
	Outer Radius	150.0	150.0
Main Vessel	Length	4500.0	4500.0
	Inner Radius	267.0	267.0
	Outer Radius	279.0	279.0
Chromatic Corrector	Z (upstream surface)	2234.0	2281.0
	Radius Of Curvature	1385.0	1307.0
	Central Thickness	20.0	20.0
	Inner Radius	75.0	75.0
	Outer Radius	160.0	160.0
Mangin Mirror	Z (upstream surface)	5732.0	5741.0
	Radius Of Curvature (refracting)	6615.0	8994.0
	Radius Of Curvature (reflecting)	8610.0	9770.0
	Central Thickness	40.0	40.0
	Inner Radius	50.0	40.0
	Outer Radius	150.0	150.0
Diaphragm	Z (centre)	1251.0	1290.0
	Radial Position Of Aperture	100.0	100.0
	Aperture Diameter	2.0	2.0
Condensers	Z (upstream surface)	1211.0	1250.0
	Maximum Thickness	10.0	10.0
	Radius Of Curvature	300.0	300.0
Quartz Windows	Z (upstream surface)	851.0	910.0
	Thickness	10.0	10.0
	Radius	22.5	22.5
	Radial Offset (of centre)	103.0	103.0
KTAG			
Spherical Mirrors	Z (of cap centre)	701.0	701.0
	Radius Of Curvature	51.68	77.52
	Diameter	50.0	50.0
	Central Angle (deg)	45.0	45.0
	Radial Offset (of cap centre)	106.0	106.0

A.2 Tolerance plots

This section presents the plots that were generated during the calculation of optical and mechanical tolerances based on the number of detected photons. Each plot highlights the nominal value of a parameter, which is indicated by a red mark on the x-axis. For parameters dependent on both an x and y coordinate, such as the lens positions, only the radial distance is considered due to the cylindrical symmetry of the Cedar. The tolerance for the refractive index follows a different method, which is outlined in section A.2.

Mangin Mirror:

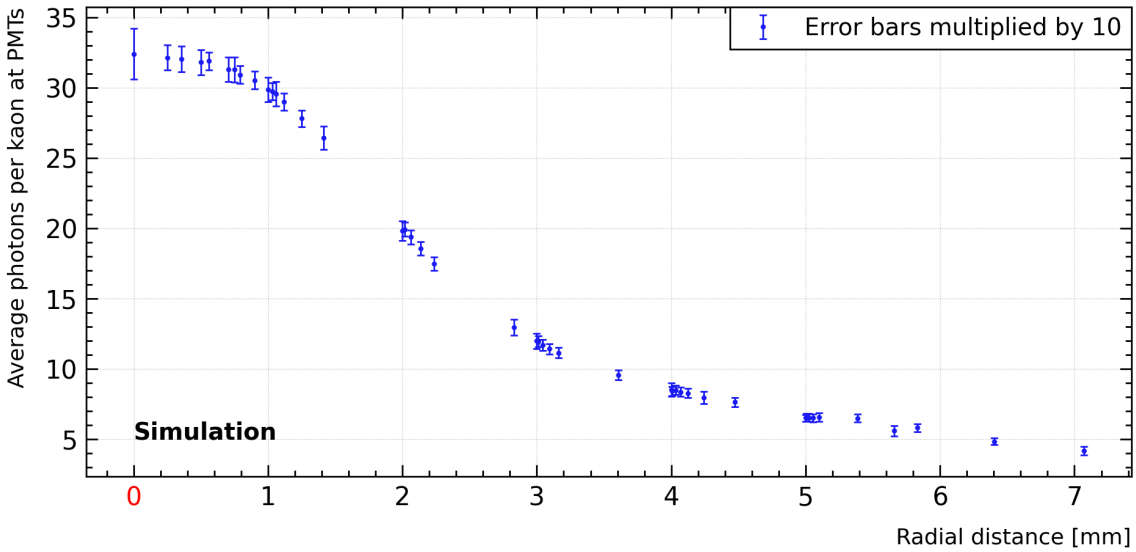

Figure A.1: Number of photons per kaon as the Mangin Mirror is moved in the x-y plane.

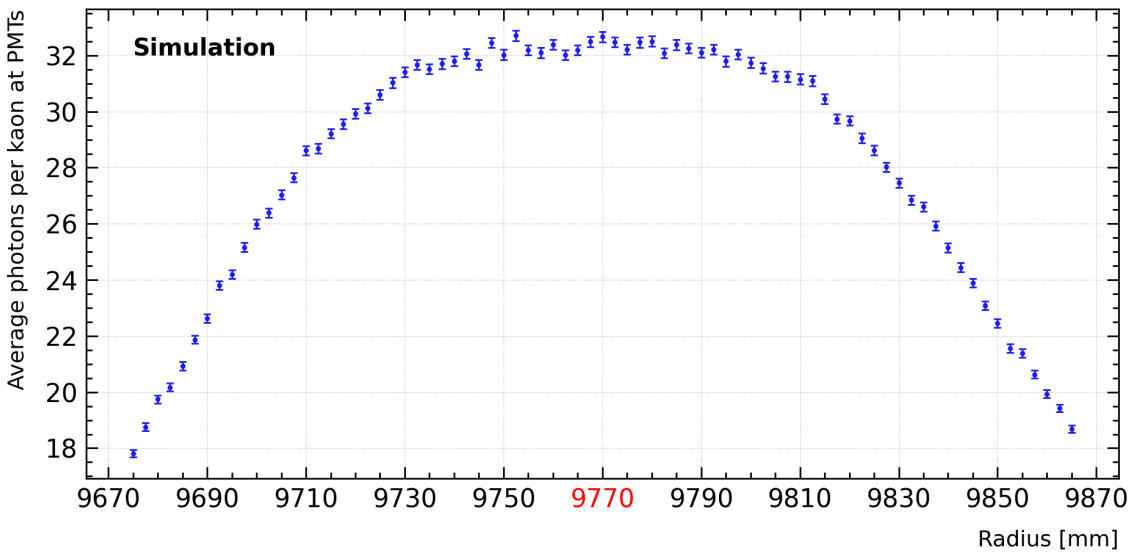

Figure A.2: Number of photons per kaon as the Mangin Mirror reflective surface radius of curvature is altered.

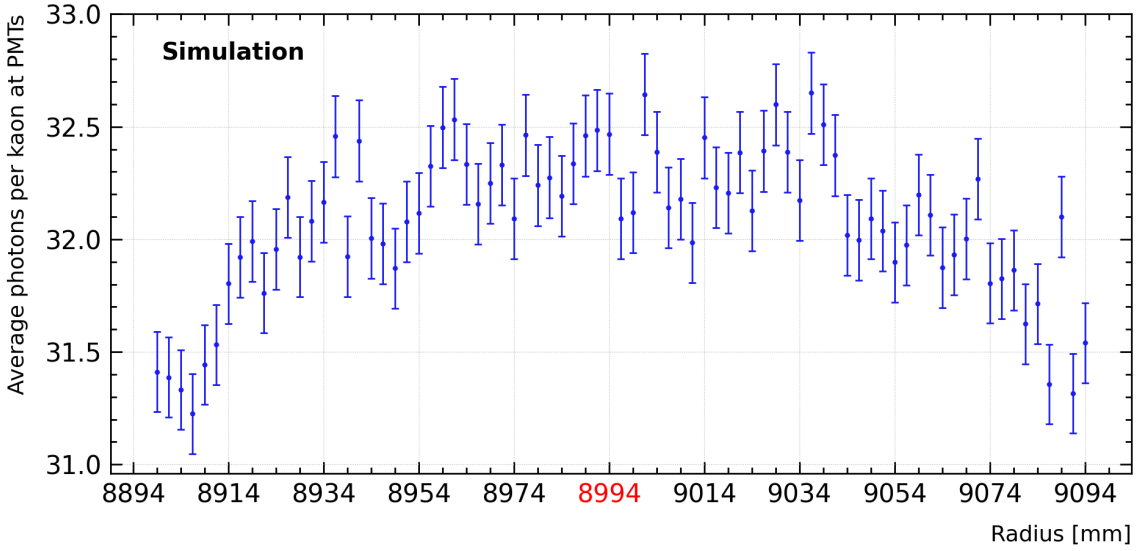

Figure A.3: Number of photons per kaon as the Mangin Mirror refractive surface radius of curvature is altered.

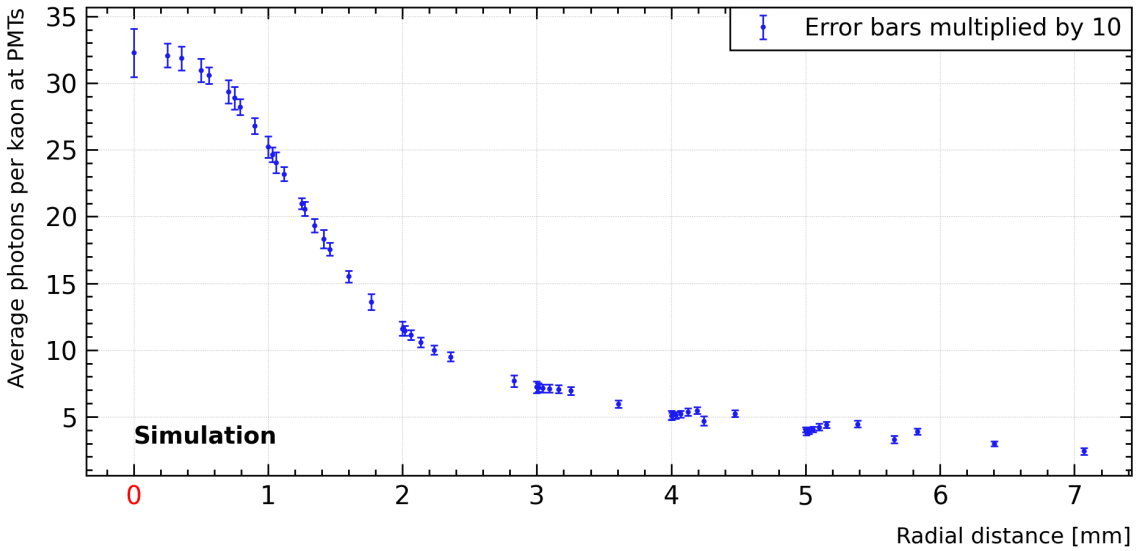

Figure A.4: Number of photons per kaon as the Mangin Mirror reflective surface centre of curvature is altered.

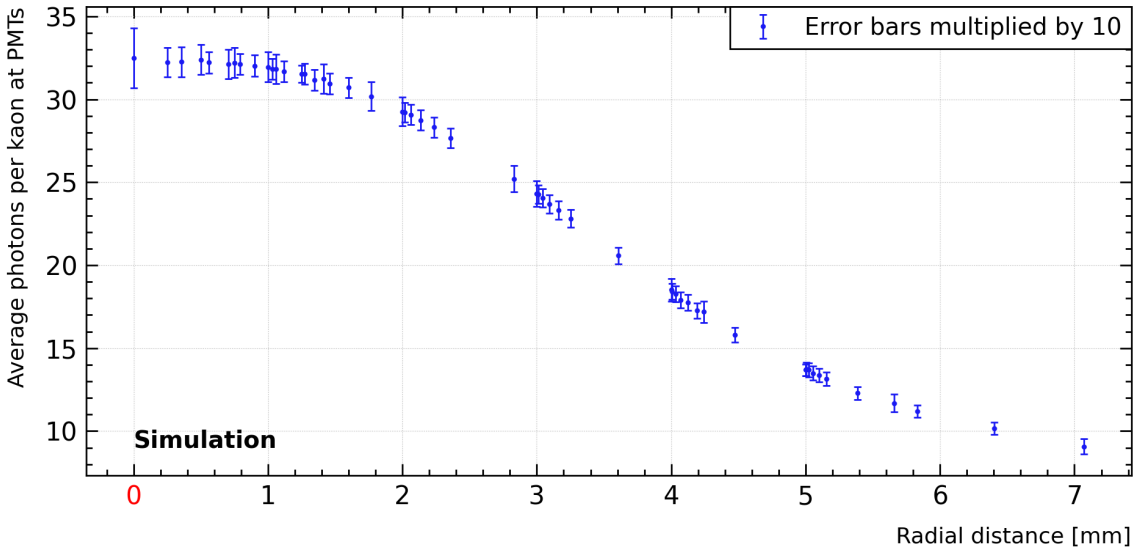

Figure A.5: Number of photons per kaon as the Mangin Mirror refractive surface centre of curvature is altered.

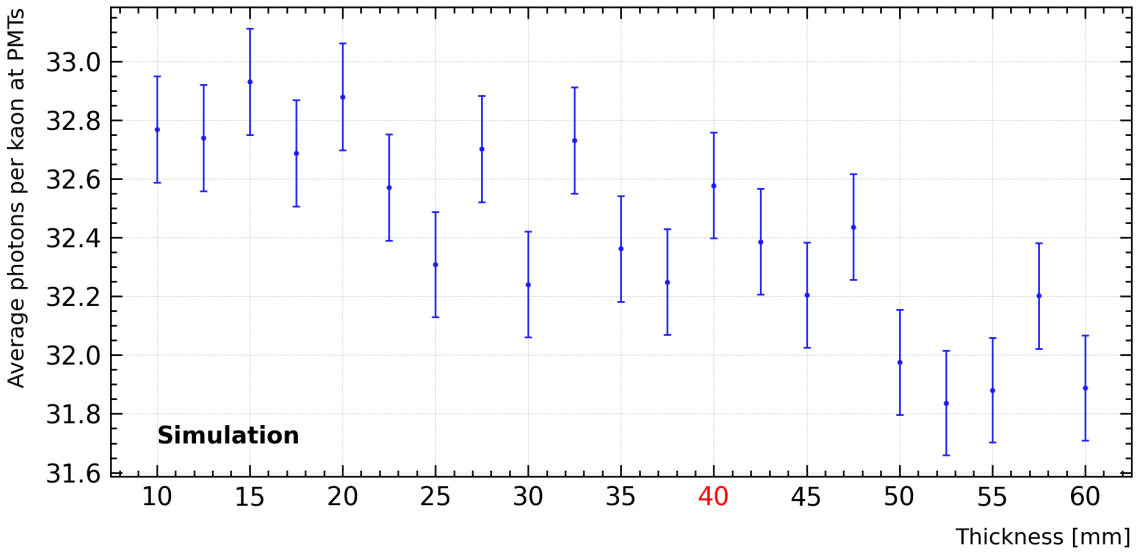

Figure A.6: Number of photons per kaon as the Mangin Mirror thickness is altered.

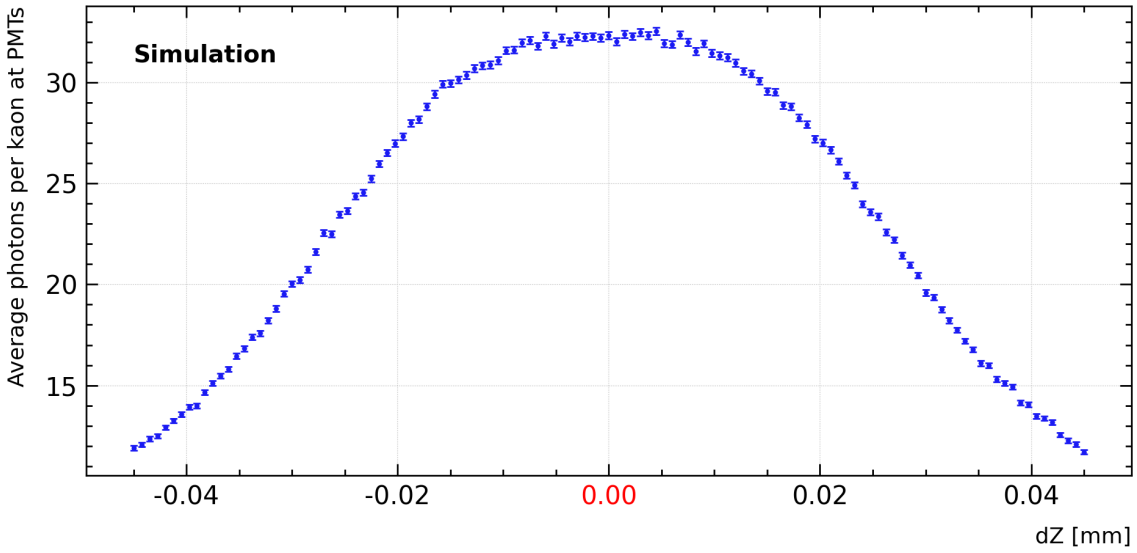

Figure A.7: Number of photons per kaon as the Mangin Mirror is tilted.

Chromatic Corrector:

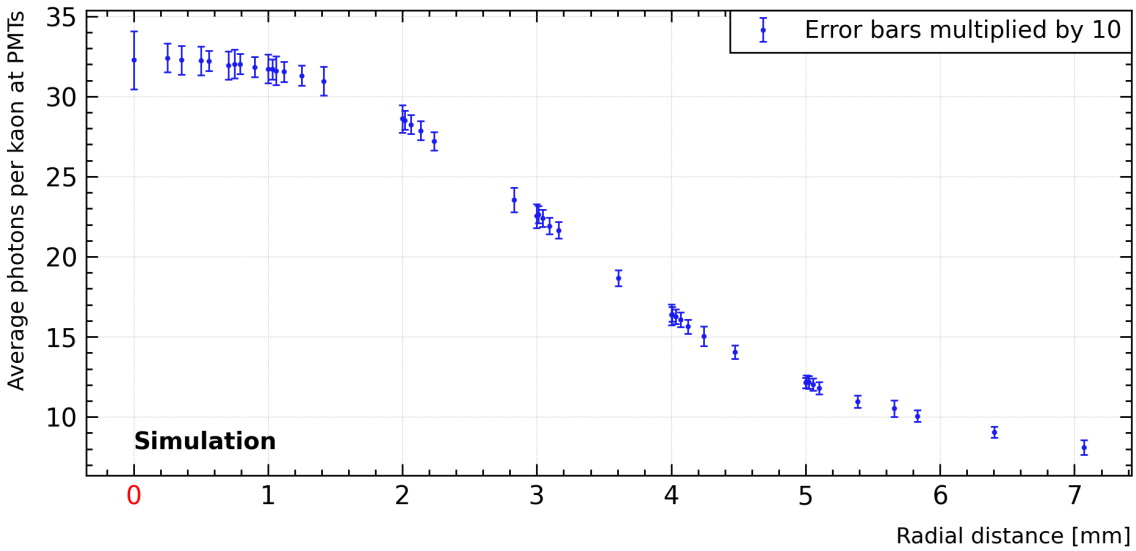

Figure A.8: Number of photons per kaon as the Chromatic Corrector is moved in the x-y plane.

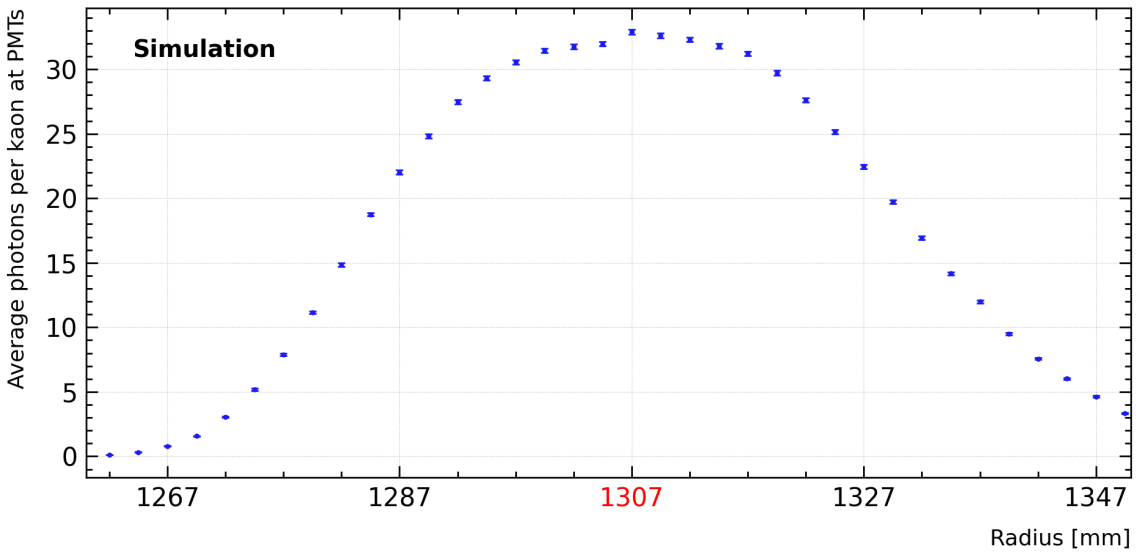

Figure A.9: Number of photons per kaon as the Chromatic Corrector radius of curvature is altered.

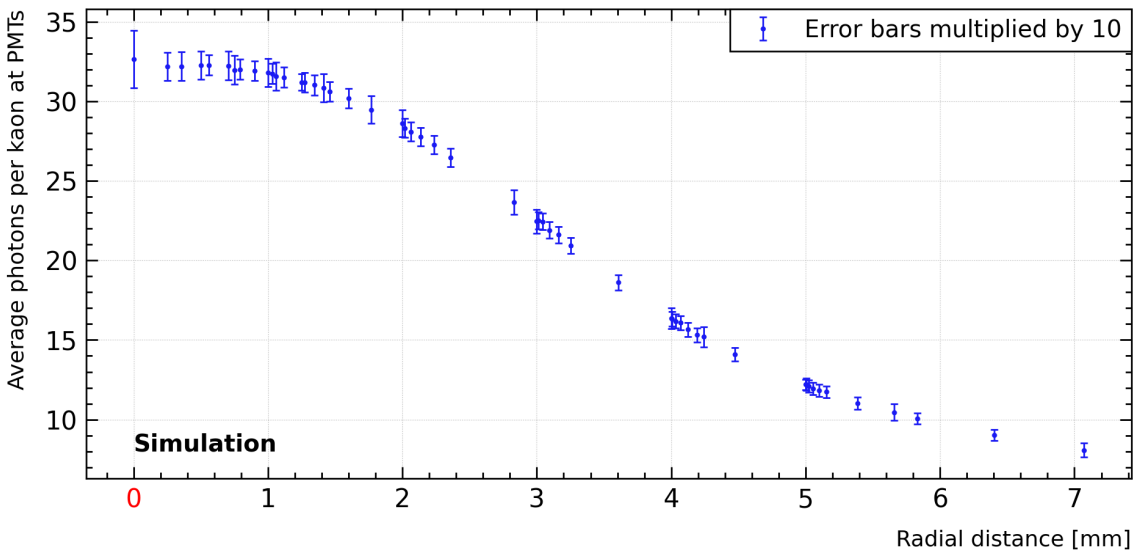

Figure A.10: Number of photons per kaon as the Chromatic Corrector centre of curvature is altered.

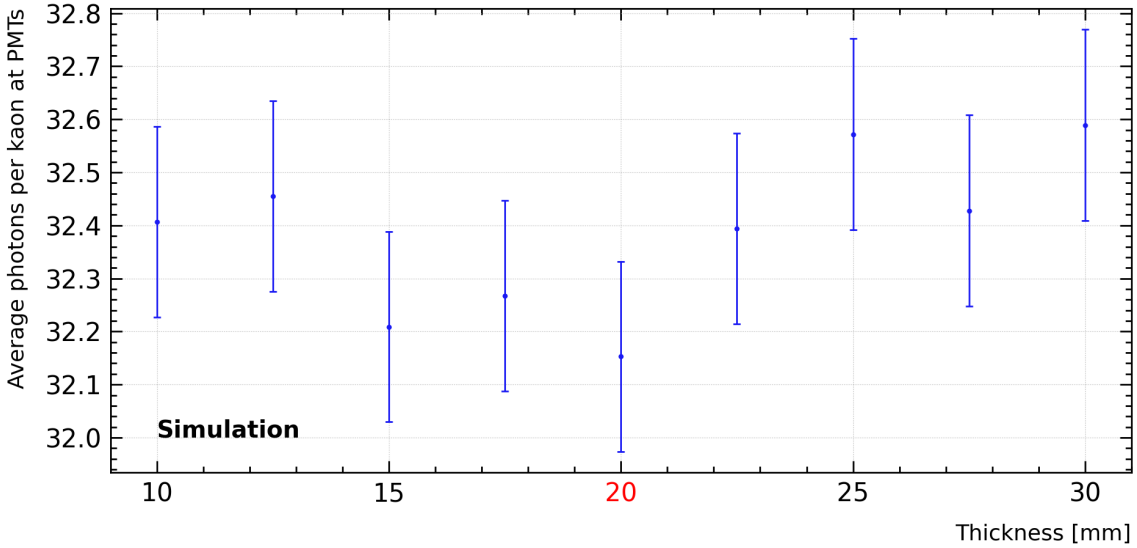

Figure A.11: Number of photons per kaon as the Chromatic Corrector thickness is altered.

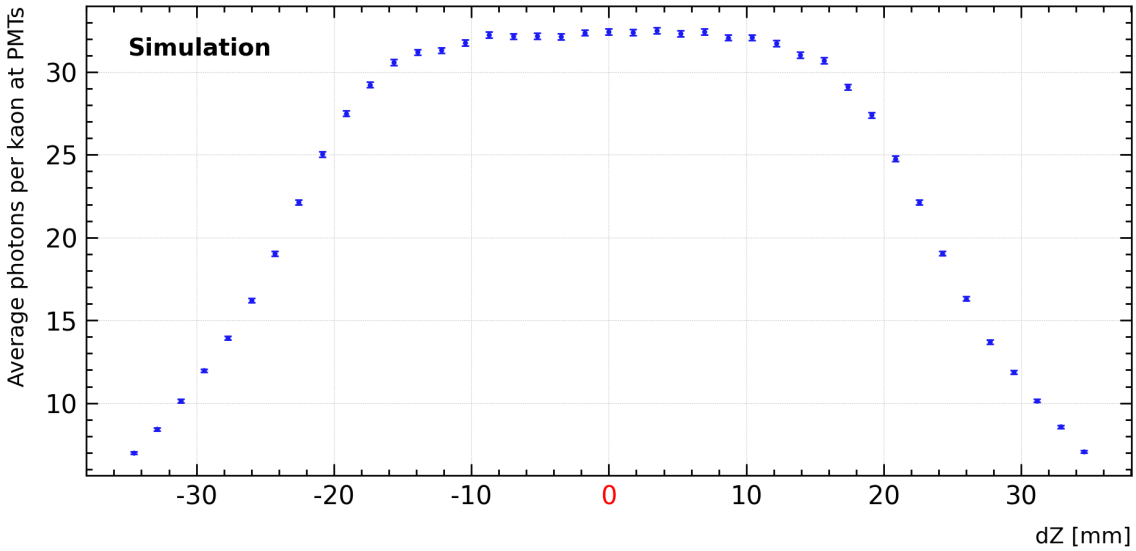

Figure A.12: Number of photons per kaon as the Chromatic Corrector is tilted.

KTAG:

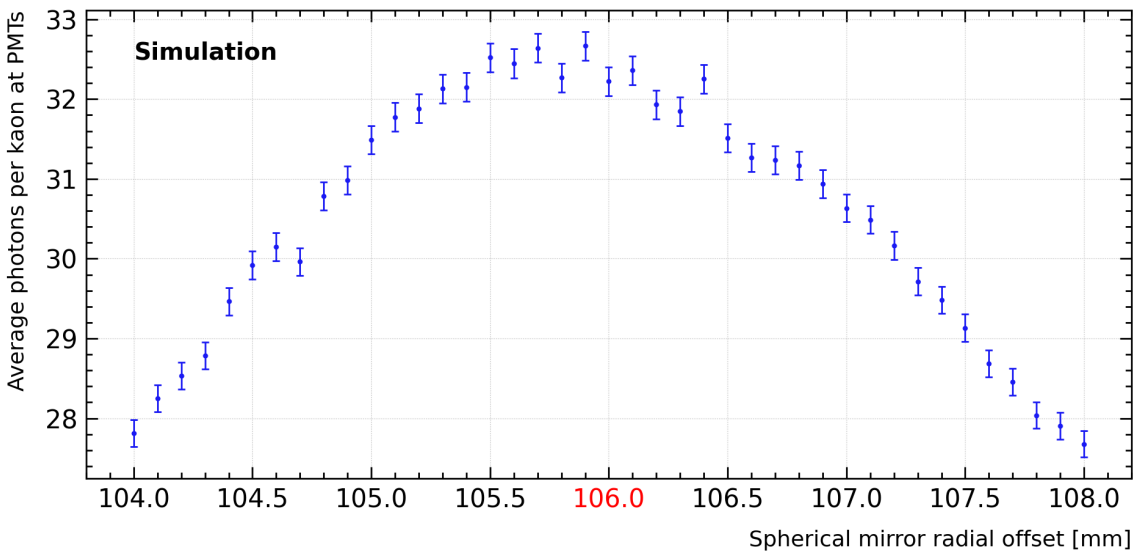

Figure A.13: Number of photons per kaon as the Spherical Mirror is moved away from the beamline.

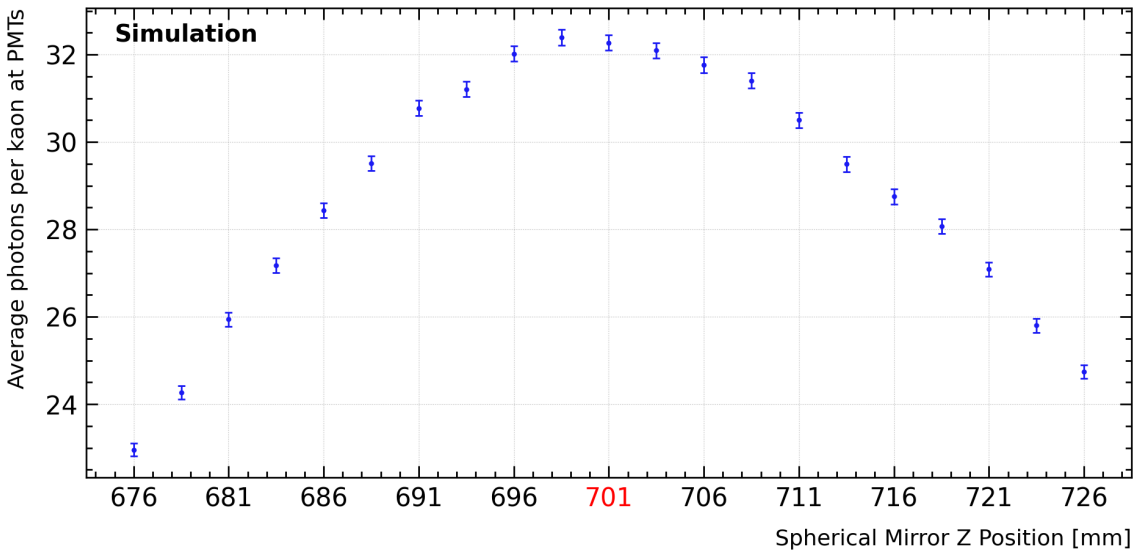

Figure A.14: Number of photons per kaon as the Spherical Mirror is moved in the z direction.

A.3 Tolerance of refractive index

To calculate the tolerance on the refractive index, we analyze each lens separately as their relative position to the diaphragm plane impacts the result. We begin by examining how the mean and width of the light rings are affected by a constant multiplicative factor applied to the refractive index. A multiplicative factor was chosen since the refractive index relies on the wavelength of photons, and fixing it for all wavelengths would result in a broad ring at the diaphragm. Figures A.15 and A.16 illustrate how the mean and width of the kaon and pion rings change as a function of this multiplicative factor. The mean exhibits a linear trend, while the width increases quadratically.

A toy MC simulation was devised to assess the tolerance on the non-uniformity. To replicate the non-uniformity of each lens, we allow each photon to perceive a different refractive index based on a Gaussian distribution centered on the nominal refractive index but with varying width. Again, we adopt a multiplicative factor to simplify the problem (refer to Figure A.17a). We sample this Gaussian multiplicative factor, which becomes the refractive index perceived by a given photon. Subsequently, we utilize the information from the uniform scans to determine the expected mean and width of a light ring for that particular wavelength. We can then sample a Gaussian distribution with the anticipated mean and width, representing where the photon will strike the diaphragm plane (see Figure A.17b). After simulating all the photons, the final light distribution can be fitted with a Gaussian distribution. The width of the light ring is plotted as a function of the multiplicative factor width in Figure A.18. Considering a 10% increase in the width of the light ring, a tolerance of 0.5% for the Mangin Mirror and 0.1% for the Chromatic Corrector was calculated.

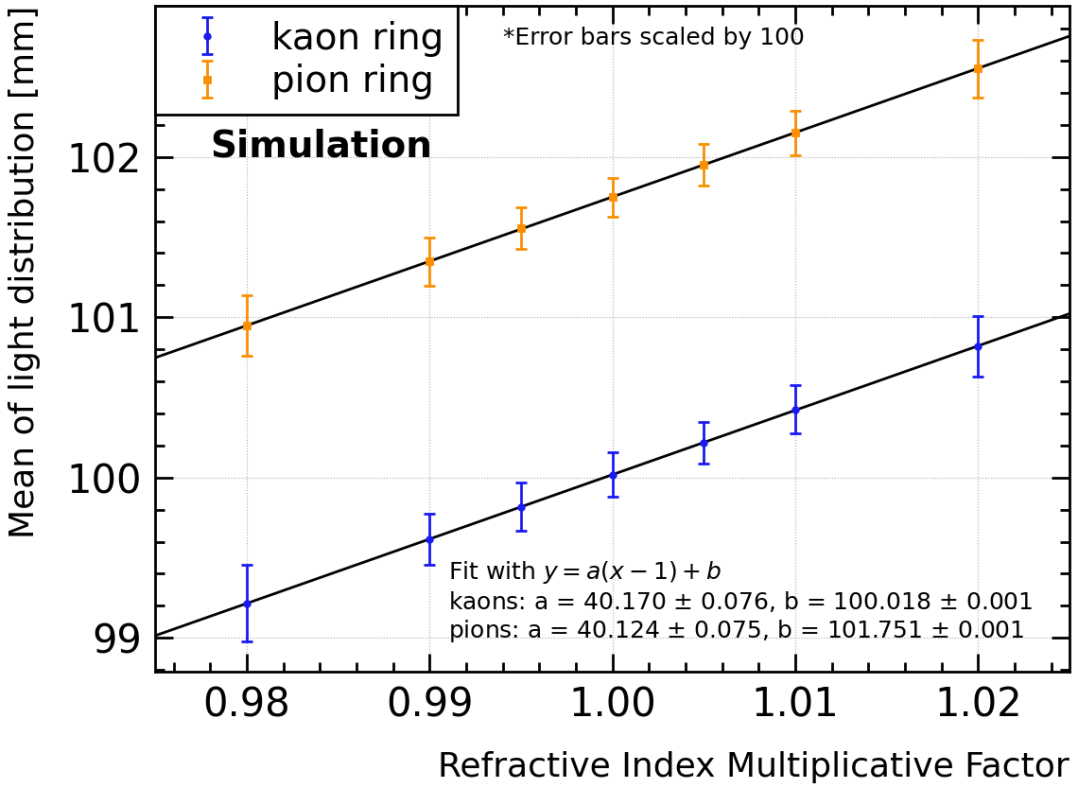

(a) Mangin Mirror

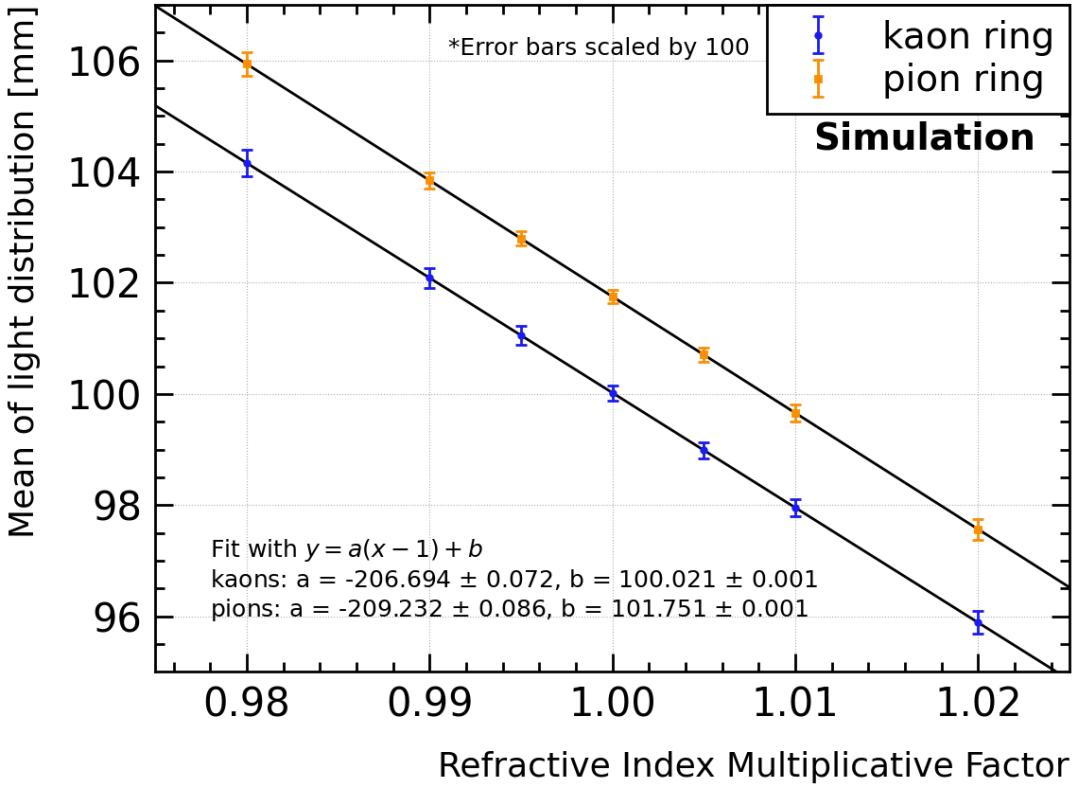

(b) Chromatic Corrector

Figure A.15: Mean position of the kaon and pion light rings as the refractive index of the Mangin Mirror and Chromatic Corrector is changed uniformly.

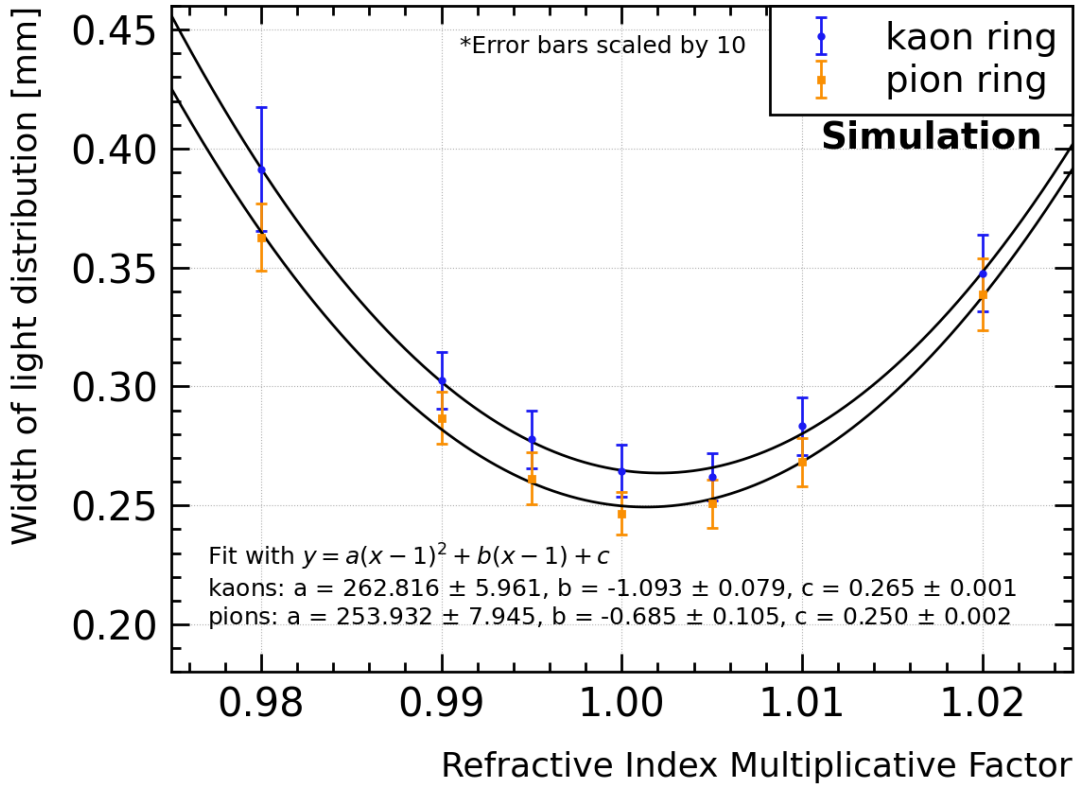

(a) Mangin Mirror

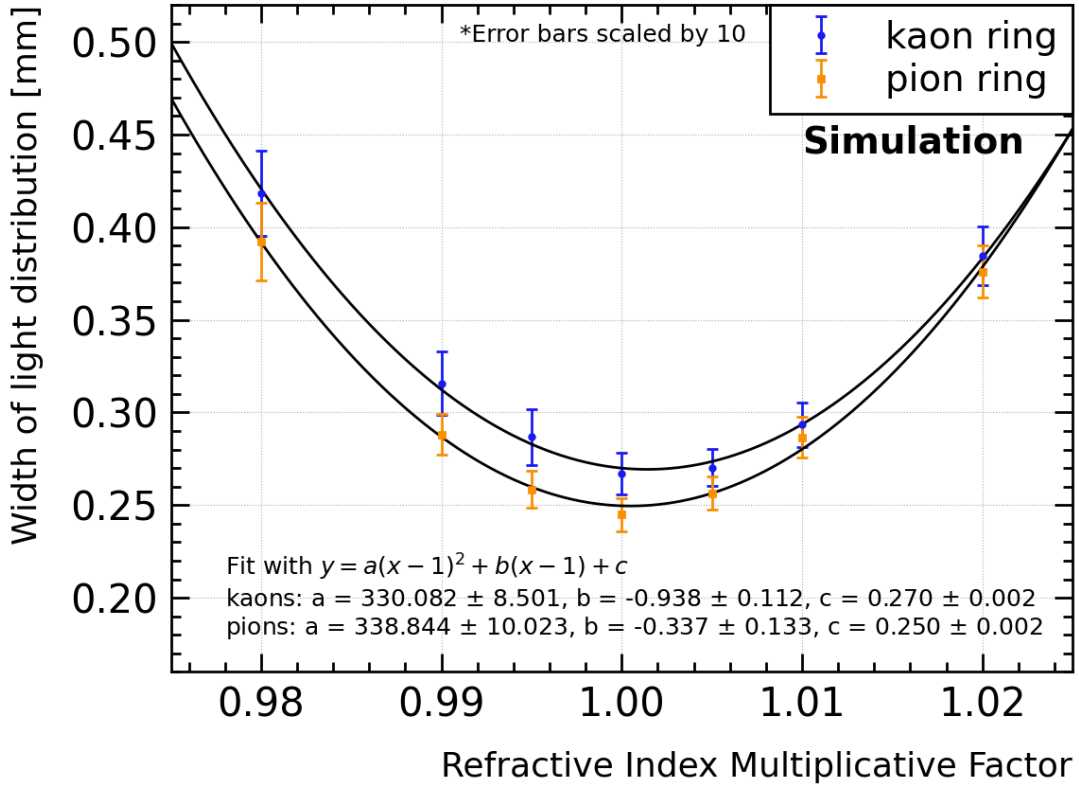

(b) Chromatic Corrector

Figure A.16: Gaussian width of the kaon and pion rings as the refractive index of the Mangin Mirror and Chromatic Corrector is changed uniformly.

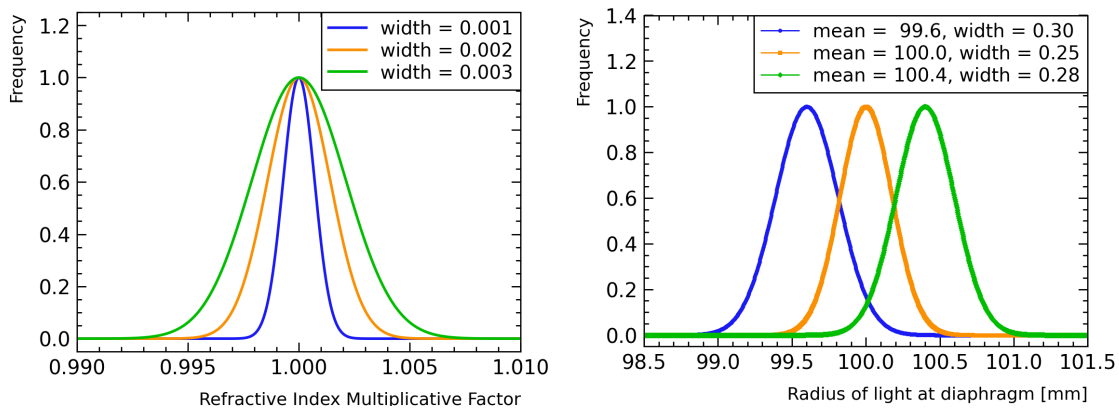

(a) Refractive index multiplicative factor.

(b) Mean and width of light ring.

Figure A.17: Example Gaussian Distributions for calculating refractive index tolerance.

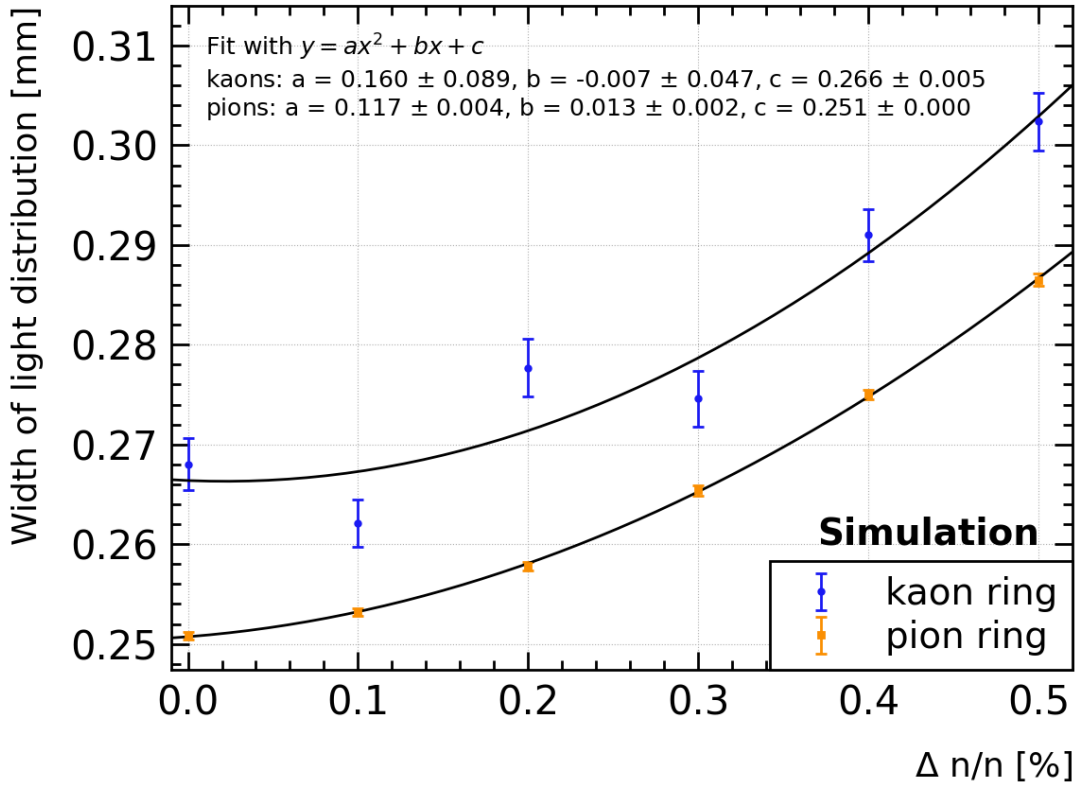

(a) Mangin Mirror

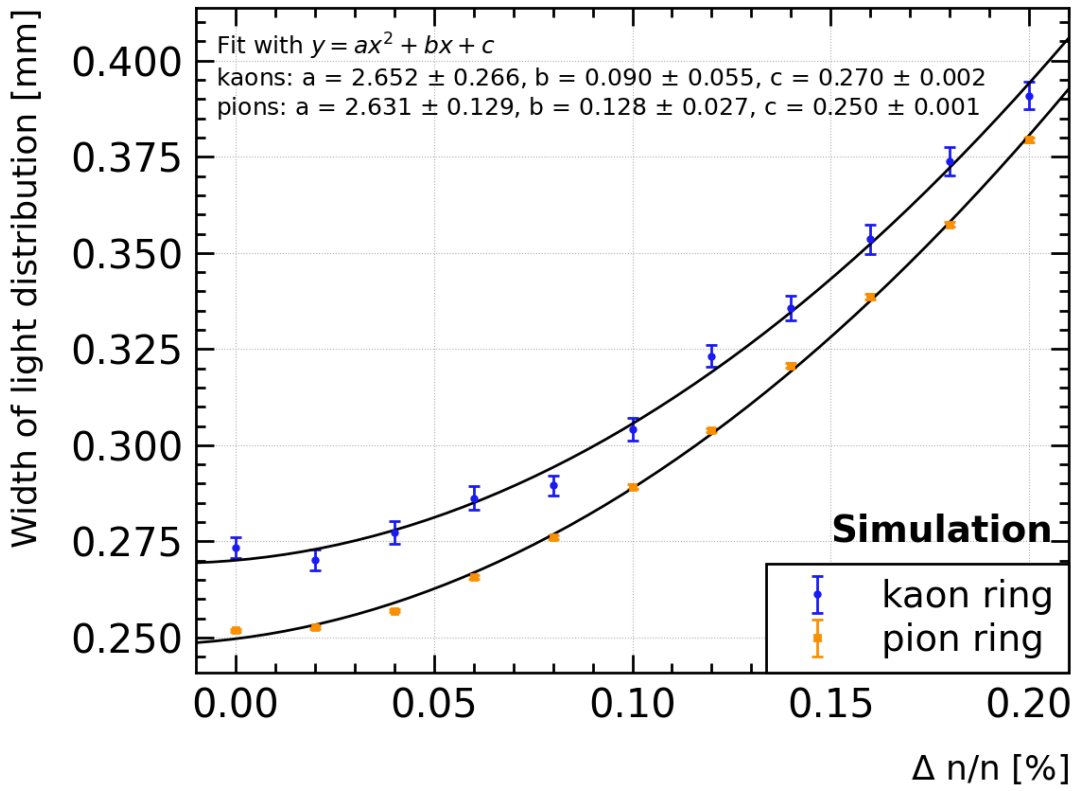

(b) Chromatic Corrector

Figure A.18: Gaussian width of the kaon and pion rings allowing for each photon to 'see' a different refractive index following a Gaussian distribution with width Δn/n.